A Thesis Submitted for the Degree of PhD at the University of Warwick

Collective Instability and Physics of the Anomalous Doppler Resonance in Fusion Plasmas

by

Samuel William Alan Irvine

Thesis

Submitted to the University of Warwick

for the degree of

Doctor of Philosophy

Department of Physics

September 2018

THE UNIVERSITY OF
WARWICK

Contents

List of Figures

Declarations

The work presented in this thesis is that of the author, except where stated otherwise, and was carried out at the university of Warwick under the supervision of Profs. S. C. Chapman and R. O. Dendy. The work has not been submitted for any other degree.

Some part of the work presented herein have been published in Refs[1].

Abstract

The anomalous Doppler instability (ADI) is a key relaxation mechanism for suprathermal electrons in magnetic confinement fusion (MCF) plasmas. The ADI involves a shift from parallel to perpendicular electron motion, accompanied by the excitation of waves at frequency and wavenumber satisfying the anomalous Doppler resonance condition. In this thesis we split effort between studying the physics of the anomalous Doppler resonance and developing a new code to address linear calculations in magnetized plasmas characterized by arbitrary gyrotropic velocity distribution functions. This fully relativistic code is more general than the analytical linear theory which has been performed previously. This code is benchmarked against many problems in plasma physics.

We perform 2D3V particle-in-cell (PIC) simulations of the ADI for an energetic electron tail oriented in the magnetic field direction. For the first time we verify, via fully kinetic simulation, that the long standing conjecture, that it is possible for the ADI to self consistently drive a positive slope in the parallel electron velocity distribution, is correct. We show that the presence of this positive slope excites waves in a separate region of frequency and wavevector space to the ADI. We show that the simulated linear and quasilinear stages of instability demonstrate strong agreement with the linear solver which we have constructed. We also show that the addition of a second simulated spatial dimension is necessary to capture nonlinear three-wave coupling which can be driven by the ADI. The location of this three-wave triad, which has not previously been explored, is consistent with what would be predicted by the wave matching condition and a cold plasma model.

Chapter 1

Introduction

1.1 Nuclear Fusion

Nuclear fusion is the process of combining atomic nuclei. A fusion event which produces nuclei with atomic number below Z = 26 will generally yield net energy gain. The fusion cross section σ_f is a measure of the probability that two nuclei will fuse as function of velocity. For fusion to occur the atomic nuclei must overcome the coulomb potential between positively charged ions. Due to the strength of the coulomb potential very high temperatures are required. Understanding fusion relevant conditions therefore necessitates the study of plasmas. The four fusion reactions with favourable characteristics for energy production are:

$$\begin{aligned}
{}^{2}_{1}\mathrm{D} + {}^{3}_{1}\mathrm{T} &\rightarrow {}^{4}_{2}\mathrm{He} + \mathrm{n}^{0}, \\
{}^{2}_{1}\mathrm{D} + {}^{2}_{1}\mathrm{D} &\rightarrow {}^{3}_{1}\mathrm{T} + \mathrm{p}^{+} \quad 50\% \\
& {}^{3}_{2}\mathrm{He} + \mathrm{n}^{0} \quad 50\%, \\
{}^{3}_{2}\mathrm{He} + {}^{2}_{1}\mathrm{D} &\rightarrow {}^{4}_{2}\mathrm{He} + \mathrm{p}^{+}, \\
\mathrm{p}^{+} + {}^{11}_{5}\mathrm{B} &\rightarrow 3{}^{4}_{2}\mathrm{He}.
\end{aligned}$$

Of these four reactions, the most energetic and easily achievable is deuterium-tritium. This nuclear reaction has the disadvantages of producing energetic 14.1MeV neutrons which are hard to shield against, and requires that tritium be generated via splitting ${}^{7}_{3}\mathrm{Li}$ and ${}^{6}_{3}\mathrm{Li}$ using these neutrons. The last two reactions listed here are “aneutronic” in the sense that the majority of the energy produced is deposited to fusion born ions and not neutrons. Mainstream fusion research currently focuses on D-T fusion due to it having the lowest requirements for reaction. The simplicity of nuclear fusion reactions means that they do not produce long lived radioactive bi-products. There is therefore no risk of meltdown in the event of power outage or catastrophic disruption. With the exception of ${}^{3}_{2}\mathrm{He}$, the fuels are either plentifully available or self generated. This means that nuclear fusion is highly desirable in the long term as a future technology for energy generation.

1.1.1 Confinement

The main difficulty in achieving energy net gain from nuclear fusion arises due to the problem of plasma confinement. Heat escapes from the plasma more quickly than energy can be produced by fusion events. This problem is a “grand challenge” in modern physics and therefore deserves study regardless of its immediate economic application. Fusion energy gain cannot be achieved in particle colliders because the cumulative collisional cross section for scattering by 90^o greatly exceeds the fusion cross section. This means that the ion velocity distribution will rapidly thermalise before a significant enough number of fusion events can occur. It is also for this reason that early electrostatic approaches to plasma confinement such as the Farnsworth fusor, which accelerates ions using an electrode and relies on non-thermal ion velocity distributions, are not thought to be viable for net energy generation[2].

Provided that the fuel ions have a velocity distribution which is close to a Maxwellian, fusion for net energy gain remains possible. In this case, the fuel nuclei must be brought into close proximity at high enough temperatures for long enough that a significant number of fusion events can occur before the confined heat is lost from the plasma. This requirement is best known as the Lawson criterion. The Lawson criterion states that for net energy gain from D-T fusion the product of electron number density and energy confinement time, $n_e\tau_E$, must exceed $1.5 \times 10^{20}\mathrm{sm}^{-3}$[3]. This number is minimised for an ion temperature of $T_i = 25\mathrm{keV}$. This condition may be satisfied in one of two regimes. Inertial confinement fusion is possible when densities are very high but confinement times are low. Magnetic confinement fusion is only possible at near vacuum densities but has a much longer energy confinement time.

To date, the only approach to fusion which has yielded net energy gain is inertial confinement fusion. Unfortunately this success has only ever been reproduced at the scale of thermonuclear weapons. In order to be useful as a power source the energies involved must be reduced to manageable levels. In inertial confinement fusion, a great intensity of energy must be delivered to the outer edges of a fuel pellet. Most current inertial confinement fusion research considers lasers as the primary driver of choice for depositing this energy due to the very high intensities which are possible[4]. Delivery of significant energy to the fuel pellet causes a shockwave to travel through the pellet, focusing energy at the core. If this shockwave can be smooth and intense enough, the densities and temperatures at the pellets core may reach levels sufficient for fusion. If enough fusion events can occur, a chain reaction known as "ignition" may take place. Ignition means that the increase in temperature caused by the initial fusion events causes the rate of fusion of the remaining fuel to greatly increase, initiating a self sustaining cycle. In inertial confinement fusion, the inertia of the fuel must contain the elevated temperature and density long enough for a significant portion of the initial fuel to burn. In magnetic confinement fusion the fuel must be contained in a steady state by strong magnetic fields. Ignition is one of the primary goals for both inertial and magnetic confinement fusion research.

1.2 Magnetic Confinement

Magnetic confinement fusion (MCF) is the confinement of fusion plasmas using a magnetic field. When a plasma is influenced by a strong magnetic field, particle motion is altered in a fundamental way. Electrons and ions follow helical trajectories tracing the magnetic field lines. This means that the plasma is not free to move across the field lines. If the plasma is stable, heat loss across the field lines may only be due to radiation and diffusion. Due to the individual particle dynamics, heat diffusion in directions which are perpendicular to the magnetic field is much slower than diffusion in directions which are parallel to the magnetic field. The maximum pressure which may be supported by a magnetic field is $P = B^2/2\mu_0$, where μ_0 is the permeability of free space. The electron pressure of a plasma is $P_e = n_e k_b T_e$. The plasma beta of a device, which is a measure of its efficiency, is the ratio of these quantities,

$$\beta = \frac{n_e k_B T_e}{B^2/2\mu_0}. \tag{1.1}$$

A device with ideal magnetic confinement would have a plasma beta of $\beta = 1$.

The first attempts at magnetic confinement used devices which had open field lines[6]. A gas-dynamic trap is a type of device with open field lines. This class of device consists of a central cylindrical bottle region capped with two magnetic mirrors at either end. The bottle region of the trap is simply an evacuated solenoid with internal magnetic field lines which are parallel to the solenoid. This region can be extended to an arbitrary length, where particles will follow helical trajectories along its length. Within the bottle region of the trap, confinement is very efficient. The gas-dynamic trap at Novosibirsk has a perpendicular plasma beta of 0.6[7].

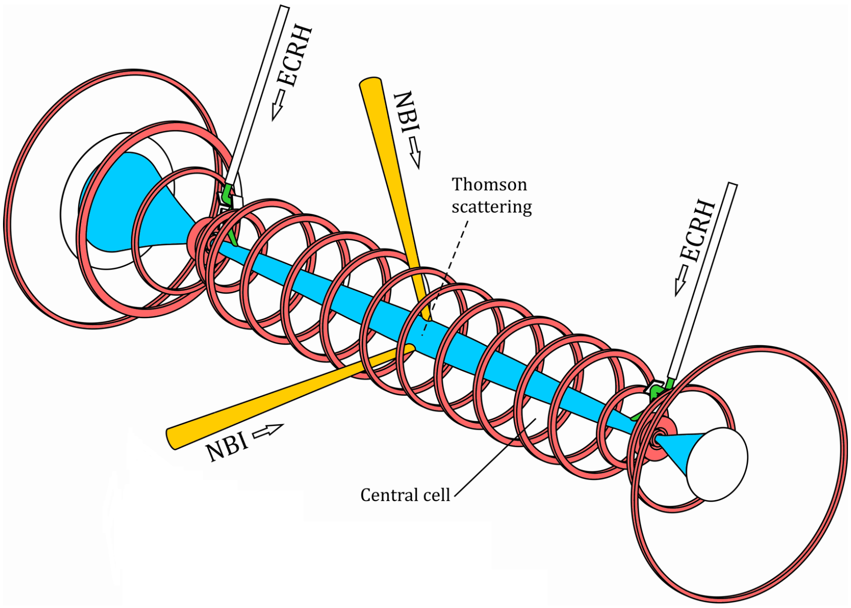

Figure 1.1: A gas-dynamic trap is an example of open magnetic confinement. Magnetic mirrors exist at either end of the trap[5].

This very attractive perpendicular performance is unfortunately negated due to the presence of open field lines at the ends of the device. In an open field configuration plasma is always free to escape along the field lines. In a gas-dynamic trap magnetic mirrors are installed to greatly reduce the rate of plasma outflow along the open field lines. The mirror principle works by increasing the magnetic field strength towards either end of the device. The magnetic moment of a charged particle in a magnetic field is an adiabatic invariant defined by $\mu = m_s v_\perp^2/2B$, where m_s is the particle species mass and $v_\perp$ is the particles velocity perpendicular to the field lines. As kinetic energy is also conserved, particles with pitch angle $\alpha = \tan^{-1}(v_\perp/v_\parallel)$ which satisfy $v_\perp^2/v_\parallel^2 > B(\mathbf{r})/B_{\max}$ follow trajectories which are reflected, where $B(\mathbf{r})$ is the magnetic field at the particles position and $B_{\max}$ is the maximum magnetic field strength of the mirror. The remaining particles are free to escape the trap, leaving behind a loss cone in velocity space. Unfortunately kinetic instability and collisionally driven diffusion means that the loss cone in velocity space tends to be rapidly repopulated. This means that particles will continually stream from either end of the device. As plasma is only lost at the ends of the device, it is possible to improve confinement by increasing the device length. For net power gain in this configuration it has been calculated that a device would need to be around 1km long[8].

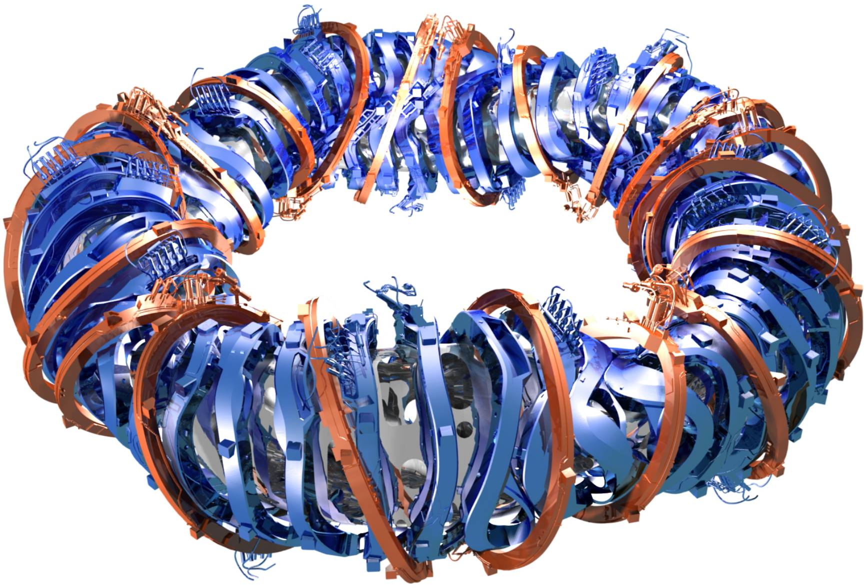

Figure 1.2: Schematic view of the superconducting magnet system of the stellarator Wendelstein 7-X[9].

1.2.1 Toroidal Confinement

The most highly developed MCF devices use confinement geometries which are toroidal. The toroidal magnets of a solenoid may be wrapped around to form a closed torus. In this configuration open field lines are not present. Unfortunately there are several physical issues with this arrangement. Any force acting on a charged particle gyrating in a magnetic field impacts a velocity drift in the direction perpendicular to both the force and the field lines. This means that particles drift across the field lines. Field line curvature and changes in the magnetic field strength both impact forces on charged particles, hence a device which is simply a torus will not confine plasma effectively. The two primary designs which address this problem are stellarators and tokamaks. If the torus is morphed into a figure of eight the majority of drifts cancel. An advanced implementation of this concept is known as a stellarator. Currently the worlds largest stellarator is Wendelstein-7X. The design of the magnet system for this device has been highly optimised by numerical simulations[10]. It is clear from schematic 1.2 that significant complexity exists with the stellarator design. The complex shape of the toroidal magnets puts them under significant mechanical stress which reduces the designs already low engineering tolerances. Large stellarators therefore remain several generations behind large tokamaks which are simpler to engineer.

1.2.2 Tokamaks

Tokamaks are designed so that a central solenoid inductively drives a current in the plasma which flows parallel to the toroidal field direction. This current induces a secondary poloidal magnetic field. The poloidal field causes additional velocity drifts which mean that charged particles rotate around the tokamak. This means that the curvature and grad-B drifts tend to be averaged out over time. It also means that unless a bootstrap current emerges, or that additional current drive is applied, then tokamaks cannot operate in steady state.

Most conventional modern tokamaks have a cross section which is D-shaped. This design was widely employed in the 1980s and introduces additional shaping coils to the configuration[11]. A magnetic island or X-point exists within the cross section of the device. This X-point means that the plasma is separated into a core and an unconfined outer scrape-off layer by a last closed flux surface(LCFS) or separatrix. Plasma in the scrape-off layer is diverted to a region of the first wall near the X-point. This region of the first wall is known as the divertor and must be designed to withstand extremely high heat fluxes. This configuration is also effective at limiting high atomic number plasma impurities and allows for technologies such as liquid lithium limiters[12]. Current examples of large D-shaped tokamaks include JET, ASDEX-upgrade, DIII-D, JT60-U and KSTAR. The international thermonuclear experimental reactor (ITER) is the cumulation of this design approach and is currently projected to achieve first plasma by 2025. ITER is expected to improve energy confinement time by enlarging the plasma volume and is the flagship project for international nuclear fusion. ITER has a design goal of $Q \geq 10$[13], where Q is the ratio of output energy to input energy. There are also hopes that ITER may be able to achieve $Q = \infty$(ignition)[14].

A second approach to tokamak design is spherical tokamaks. Spherical tokamaks have a much lower aspect ratio than conventional tokamaks. The aspect ratio of a tokamak is defined as the ratio between the minor and major radii of the torus. In addition to the compact geometry afforded by their design, spherical tokamaks have the advantage of relatively high plasma β[15]. It has been suggested that by using smaller spherical tokamaks, with higher plasma β and stronger magnetic fields, that it may be possible to achieve similar performance to large devices such as ITER at lower cost[16]. Spherical tokamaks remain a possible candidate for a next generation component test facility[17].

Spherical and conventional tokamaks share a large collection of common traits, so that knowledge is often transferable between the two. The discovery of high performance mode (H-mode) at ASDEX in 1982 is an example of this[18].

H-mode is a regime of tokamak operation where confinement time is dramatically improved. It was found at ASDEX that when sufficient neutral beam power was injected, a temperature pedestal would form at the plasma edge, and turbulence would be suppressed[19]. This allowed for tokamaks to support higher temperature gradients and therefore operate at a much higher plasma β. Since its initial discovery, H-mode has been successfully employed in almost every modern tokamak[20].

1.2.3 Edge Localised Modes

Edge localised modes (ELMs) are disruptive magnetohydrodynamical (MHD) events which occur at the edge of tokamaks operating in H-mode[21]. ELMs occur when the edge pressure gradient exceeds a critical gradient. This gradient may be calculated by considering MHD stability. The onset of an ELM results in a temporary reduction in the edge pressure gradient. The pressure gradient then gradually increases, leading to conditions where ELMs can once again occur. ELMs may broadly be classified into three categories. Type I ELMs are the largest edge localised modes. In these events a large heat load may be deposited on the divertor. Type II ELMS are an intermediate category with magnitudes between type I and type II. Type III Elms are continuous and are associated with a significant deterioration of confinement. ELMs may unload significant thermal loads on the first wall and divertor[22]. ELMs have also been associated with millisecond bursts of microwave emission in MAST[23]. These microwave bursts occur on timescales too short to be accounted for by thermal emission. It is thought that this emission may be linked to collective instability and non-thermal electron populations[24]. The suppression and prediction of ELMs remains an active area of tokamak research[25]. ELMs may be considered a form of minor disruption which does not lead to total loss of plasma confinement.

1.2.4 Disruption

Disruptions are events which cause a significant loss of plasma confinement. When confinement is lost the plasma temperature rapidly drops. This “thermal quenching” causes the plasma resistivity to rapidly increase. This is followed by a rapid decrease in plasma current and the formation of a strong parallel electric field. Disruptions are a problem which occurs in both conventional tokamaks and spherical tokamaks[26]. When a disruption event occurs the first wall may experience very large thermal and mechanical loads. It has been suggested that this may significantly reduce the lifetime of plasma facing components in ITER[27, 28]. There are two main classes of instability which lead to disruption. Vertical displacement events are MHD instabilities which can occur when vertically elongated plasmas become unstable to bulk vertical motion[29, 30]. This instability involves the whole plasma and can lead to thermal quench if the plasma is displaced sufficiently to come into contact with the first wall. Major disruptions occur when the tokamak magnetic configuration becomes unstable to helical perturbations[31]. The exact cause of major disruptions varies from device to device. In most cases it is thought to be related to loss of magnetic shear and "bubble capture"[32]. The mitigation of disruptions is currently a very active area of research[33]. It is important to understand both the physics leading to disruptions, and the results of disruptions. The presence of a large parallel electric field means that vertical displacement events and major disruptions can both lead to conditions which allow the formation of energetic runaway electron populations[34].

1.2.5 Runaway Electrons

Runaway electrons (RE) is the term used to denote electrons which are free to accelerate to very high energies. Under normal conditions, electrons which are accelerated to higher velocities will rapidly thermalise due to collisions. Dreicer showed that by solving the collisional Boltzmann equation:

$$\frac{\partial f}{\partial t} + \frac{eE_{\|}}{m_e}\frac{\partial f}{\partial v_{\|}} = \frac{\partial f}{\partial t_{\mathrm{coll}}}, \tag{1.2}$$

for a plasma comprised of thermal electrons and thermal ions in static electric field, that a runaway electron tail could be produced[35, 36]. For electrons with parallel velocity $v_{\|} > v_c$ there exists some critical value of the electric field E_c for which runaway will occur. This effect arises because the collisional friction force experienced by electrons scales as $v_{\|}^{-2}$. This means that for electrons going faster than the critical velocity v_c, the collisional drag force is less than the force applied by the electric field. These accelerated particles continue to be preferentially accelerated and form an energetic tail that is distinct from the bulk of the distribution. Once a small population of runaway electrons exists it has been suggested that an avalanche mechanism may drag further electrons out into the tail[37]. Small angle collisions between high energy electrons in the tail and electrons in the bulk may allow for electrons in the bulk to exceed the Dreicer velocity.

When present, runaway electrons may exasperate the already hostile conditions of disruption. Significant quantities of energy may be deposited on very localised regions of the first wall. Concern exists that this problem may be more severe in ITER[38]. The mitigation of this damage remains an active area of research, where interest has been placed in strategies such as argon puffing[39], or using thin layers of tungsten as shielding[40]. Understanding the physics of runaway electrons requires detailed calculations spanning a multitude of time-scales.

1.3 Models for magnetized Plasma

Plasma physics is a discipline which describes physical phenomena which occur across a wide range of spatial and temporal scales. Multiple approaches are therefore required to describe physics in different regimes. Fluid models describe plasmas in terms of smoothed quantities such as bulk velocity and density. Magnetohydrodynamics (MHD) is a theory which describes the magnetic properties of conducting fluids. MHD solves the continuity equation, fluid equation of motion and the energy equation of state. This theory is useful for describing macroscopic physics which occurs on length and time-scales much longer than the ion gyro-radius and gyroperiod. It is also a good predictor for plasma stability in tokamaks. Ideal (zero resistivity), resistive and Hall MHD are frequently applied to calculate tokamak stability[41]. It is possible to model dynamic processes such as merging compression in spherical tokamaks using MHD[42]. Publicly available MHD solvers relevant to the study of plasma in tokamaks include Nimrod[43], HiFi[44], Elite[45] and many more.

Because fluid models only track the moments of particle distributions, they can never capture structures in velocity space and therefore have limited applicability for calculating dynamical properties which depend on velocity anisotropy. Codes can be constructed which trace the orbit trajectories of charged particles in arbitrary evolving magnetic and electric fields. These Orbit tracing codes can be coupled with the output of MHD simulations, an approach which has been to used to understand fast particle behaviour during sawtooth crashes[46] and merging compression[1].

Orbit tracing codes are not fully self-consistent. This means that the currents produced by particle populations do not feed back to the fields dictating their trajectories. For this reason, it is not possible to model physics involving resonant wave-particle interactions using orbit tracing codes. To understand wave-particle resonance and fast physics at small scales, it is necessary to study kinetic theory.

1.3.1 Kinetic Theory

Kinetic theory describes gases or plasmas by a continuous particle distribution function. Equal emphasis is placed on the spatial and velocity dependence of this distribution function. Kinetic theory is applicable when a large enough number of particles exist for the approximation of a continuous distribution to be statistically valid. The most fundamental equation in kinetic theory is the Boltzmann equation:

$$\frac{\partial f_s}{\partial t} + \frac{d\mathbf{r}}{dt} \cdot \frac{\partial f_s}{\partial \mathbf{r}} + \frac{d\mathbf{p}}{dt} \cdot \frac{\partial f_s}{\partial \mathbf{p}} = \left(\frac{\partial f_s}{\partial t}\right)_{\text{coll}}. \tag{1.3}$$

The species distribution function $f_s(\mathbf{r}, \mathbf{p}, t)$ describes the number density of a particle species as a function of position, momentum and time. The most complex part of this equation is the collisional term. In gas only binary collisions need to be considered. Collisions involving lager numbers of particles occur so infrequently that they can be neglected. The Boltzmann collision operator defines the rate of collision between distribution functions $f_1(\mathbf{r}, \mathbf{p}, t)$ and $f_2(\mathbf{r}, \mathbf{p}, t)$ for collision cross section $\sigma(\mathbf{p}_1, \mathbf{p}_2)$:

$$\begin{aligned}\left(\frac{\partial f_2}{\partial t}\right)_1 = \int\int\int & \boldsymbol{\sigma}(\mathbf{p}_1, \mathbf{p}_2; \mathbf{p}_1', \mathbf{p}_2')|\mathbf{p}_1 - \mathbf{p}_2| \\ & \times \left(f_1(\mathbf{p}_1')f_2(\mathbf{p}_2') - f_1(\mathbf{p}_1)f_2(\mathbf{p}_2)\right) d^3\mathbf{p}_2 d^3\mathbf{p}_1' d^3\mathbf{p}_2'. \end{aligned} \tag{1.4}$$

Here $\mathbf{p}'$ denotes original momentum and $\mathbf{p}$ denotes momentum after collision. Due to the challenges involved with efficiently calculating the Boltzmann collision operator, this topic is still an area of active computational research[47]. Several simpler collision operators exist. For example the BGK[48] approximation assumes that collisions will always force a non-Maxwellian distribution to return to a Maxwellian distribution at a rate proportional to the collision frequency.

Coloumb interactions are long range and therefore cannot be modelled efficiently by using a binary collision operator. Low density plasmas such as those found in tokamaks are dominated by long range collisions. It is possible to ignore short range collisions and instead model long range interactions by tracking electric and magnetic fields and applying the Lorentz force law. This gives the Vlasov equation:

$$\frac{\partial f}{\partial t} + \frac{d\mathbf{r}}{dt} \cdot \frac{\partial f}{\partial \mathbf{r}} + q_s\left(\mathbf{E} + \mathbf{v_s} \times \mathbf{B}\right) \cdot \frac{\partial f}{\partial \mathbf{p}} = 0 \tag{1.5}$$

To solve the Vlasov equation it is necessary to describe the feedback of moving charge back into Maxwell's equations. This gives the Maxwell-Vlasov system of equations. When described classically a point charge produces an electric field which is unbounded at short range. In plasma physics this problem is avoided by consideration of the Debye sphere. The short range interaction between charged particles is greatly reduced because of electric field “screening” due to local cloud of mobile electrons. In practise Vlasov models often neglect short range collisions entirely. Effects occurring on longer time-scales may be described by the Landau (Fokker-Planck) collision operator, which approximates the effect of many small angle collisions[49].

In general it is very computationally expensive to directly solve the Vlasov equation. Several simplifications may be applied to the full treatment of kinetic theory. Drift-kinetics and gyrokinetics reduce computational requirements by gyro-averaging the distribution function[50, 51]. These theories are useful for describing physics on intermediate time-scales between a fully kinetic treatment and a MHD treatment. Neither drift-kinetics or gyrokinetics may fully capture the physics of gyrating particles interacting with the electric and magnetic fields. Several categories of hybrid codes also exist, which treat electrons and ions differently. As we wish to investigate the physics of electrons, it is necessary to maintain a good understanding of full kinetic theory.

Because kinetic theory does not describe individual particles, it is unable to address certain physical processes. The Klimnitovich equation describes every particle in a plasma individually[52]. This allows for physical phenomena which depend on the statistical properties of the phase space distribution function to also be resolved. In practise this approach is limited to modelling a very small number of physical particles. We can capture many of these effects by using particle-in-cell codes, which instead model spatially smoothed elements in phase space. We address particle-in-cell codes in Section 2.1.

1.3.2 Velocity-Space Instability

The Maxwell-Vlasov system of equations describes electromagnetic fields and their interactions with the underlying particle distribution functions. For plasma there are many oscillating solutions which depend on the initial conditions. These solutions form a spectrum of travelling waves. This spectrum makes up the plasma dispersion relation. These solutions can be stationary, damped, or growing in time. It is often the case that the behaviour of these waves is significantly modified by the particular form of the velocity distribution. “Velocity-space instability” occurs when the velocity distribution causes waves to grow in time.

Velocity space instabilities can cause “collective emission”. Collective emission is distinct from thermal emission in that collective emission involves the whole plasma, while thermal emission only involves single particles. Observations of collective emission tend to rapidly grow in time, and may have luminosities which greatly exceeds what is possible from thermal emission alone. Collective emission may grow very rapidly in time until some saturation point is reached, when the rate of energy transfer from the particle distribution to electric or electromagnetic waves becomes limited. This means that it is possible to observe short bursts of microwave emission which may be attributed to velocity space instability.

A great number of velocity-space instabilities are known. These are distinct from MHD instabilities which only depend on the bulk properties of the plasma. A key theme in the study of velocity space instability is wave-particle resonance. Wave-particle resonance occurs when individual particles are resonant with waves with phase velocity equal to the particles velocity. The addition of a strong magnetic field allows for additional harmonic wave-particle resonances to occur, at increments of the particles cyclotron frequency. This results in a wider array of instabilities being possible when plasma is magnetized. The anomalous Doppler instability is an example of velocity space instability which may occur in runaway electrons in magnetized plasma. We introduce the properties of this instability in more detail within Chapter 4.

1.4 Thesis Outline

The research presented in this thesis is motivated primarily to advance the knowledge of kinetic theory relevant to runaway electrons in tokamak plasmas. We place an emphasis on studying velocity space instabilities which occur on short time-scales, rather than studying collisional physics which requires much longer time-scales to resolve. The two primary research chapters of this thesis govern the construction of a fully gyrotropic relativistic kinetic dispersion solver and fully kinetic two spatial three velocity (2D3V) self-consistent particle-in-cell simulations of the anomalous Doppler instability.

We begin this thesis by first discussing the methods which we use to perform simulations and by outlining some of the methods used to analyse data from particle-in-cell codes. We benchmark the calculation of linear growth rates using a simple 1D simulation of an electron two-stream instability. In this section we also show how spatiotemporal Fourier transforms can be computed and compare against the dispersion relation of a cold plasma model. As a demonstration of our methodology, polarization which is calculated from theory is compared to polarization computed by simulation.

In the first research chapter of this thesis, we construct a code to solve linear physics in magnetized plasmas characterized by arbitrary gyrotropic velocity distributions. This code is able to accurately predict the frequency, growth and damping rates for plasma waves. Additionally, quantities such as polarization may be computed for these solutions. Fully relativistic and non-relativistic variants of this code are constructed. Following a review of some of the analytical approaches to calculating the linear theory of waves in plasmas, we benchmark the non-relativistic variant of this code against a number of problems. We show that it is able to reproduce a wide range of physical effects including beam instabilities and Landau damping. The code accurately reproduces simple hydrodynamic instabilities such as streaming instabilities and more complex kinetic instabilities such as the oblique kinetic electron firehose instability. We also demonstrate that this code is capable of computing growth rates for ion cyclotron emission driven by a ring beam distribution. The relativistic variant of this code is shown to predict instability at the electron cyclotron maser resonance, where the non-relativistic variant (as expected) does not.

In the final research chapter, we perform 2D3V particle-in-cell simulations which are initially composed of a superthermal electron tail and background ion population in a guiding magnetic field. Strong agreement is found to exist between the linear growth rates that have been computed using the dispersion solver which we have developed, and the growth rates measured during the linear phase of particle-in-cell simulation. We investigate the quasilinear evolution of the electron velocity distribution in response to electrostatic waves excited by the anomalous Doppler instability. We verify by using fully kinetic simulation, for the first time, that it is possible for a positive slope to evolve self consistently in the parallel component of the velocity distribution. This positive slope triggers instability in a separate region of frequency and wavevector space to the location which is excited by the anomalous Doppler resonance. We additionally investigate the possibility for secondary non-linear wave-wave interactions. Using bispectral analysis we demonstrate that many phase locked three-wave triads exist where the beat wave is unsupported by the dispersion relation. These three-wave triads have inherently limited energy transfer. We also show that under certain circumstances, it is possible for waves at the anomalous Doppler resonance to support beat waves which are supported by the dispersion relation. We demonstrate that the region of frequency and wavevector space where we observe this effect in simulation can be well predicted by considering the frequency and wavevector matching conditions of a cold plasma dispersion model.

Chapter 2

Simulation Methods

2.1 particle-in-cell Codes

From first principles particle-in-cell (PIC) codes are the most robust method to study the kinetic theory of plasmas. In PIC codes fluid macro-particle elements which represent a large number of physical particles are tracked in continuous phase space. Certain moments of the macro-particle distribution are additionally tracked on a fixed mesh. The particles and moments are then updated iteratively. This means that the tracked quantities can evolve self consistently in time. Provided that a sufficiently large number of macro-particles are simulated, statistically significant output will be produced.

In this thesis we make significant use of the fully relativistic electromagnetic PIC code *EPOCH*[53]. This relativistic electromagnetic PIC code uses weighted macro-particles which are attributed with position and momentum. Each macro-particle represents many physical particles of a single species with a fixed charge and rest mass. In each time-step of the simulation the macro-particles momentum is updated using the Lorentz force law driven by electric and magnetic fields which are defined on a Cartesian grid. The first moment of particle velocity is then accumulated on the grid, and used to calculate current density. The current density is then used to update the electric and magnetic fields using Maxwell's equations. This iterative scheme can accurately reproduce a full range of classical micro-scale behaviour for collections of charged particles.

2.1.1 Updating Fields

Fields in *EPOCH* are evaluated on a staggered Yee-Grid[54]. The magnetic field density is evaluated on the edges of a unit cube while the electric field density is evaluated on face norms. The first two of the equations which outline the second order finite-difference time-domain (FDTD) scheme for the electric and magnetic fields at step $n+1$ are:

$$\mathbf{E}^{n+\frac{1}{2}} = \mathbf{E}^{n} + \frac{\Delta t}{2}\left(c^2\nabla \times \mathbf{B}^{n} - \mathbf{j}^{n}\right), \tag{2.1}$$

$$\mathbf{B}^{n+\frac{1}{2}} = \mathbf{B}^{n} - \frac{\Delta t}{2}\left(\nabla \times \mathbf{E}^{n+\frac{1}{2}}\right). \tag{2.2}$$

After $\mathbf{E}^{n+\frac{1}{2}}$ and $\mathbf{B}^{n+\frac{1}{2}}$ are computed, $\mathbf{j}^{n+1}$ is computed using the current density which was accumulated during the particle push. The fields are then evolved fully:

$$\mathbf{B}^{n+1} = \mathbf{B}^{n+\frac{1}{2}} - \frac{\Delta t}{2}\left(\nabla \times \mathbf{E}^{n+\frac{1}{2}}\right), \tag{2.3}$$

$$\mathbf{E}^{n+1} = \mathbf{E}^{n+\frac{1}{2}} + \frac{\Delta t}{2}\left(c^2\nabla \times \mathbf{B}^{n+1} - \mathbf{j}^{n+1}\right). \tag{2.4}$$

This explicit leapfrog scheme uses half time-steps and is preferable to implicit schemes as implicit schemes must solve for both the current and future state and are thus less computationally efficient. The time-step size Δt is chosen at the simulation onset to ensure that the Courant Friedrichs Lewy(CFL) condition is satisfied for the speed of light[55]. The 1D CFL condition for light states that $\Delta t < \Delta x/c$, where Δx is the grid spacing. In addition to satisfying the CFL condition, the numerical scheme used in *EPOCH* requires that the condition $\Delta t < \pi/\omega_{ps}$ is satisfied for stability, where $\omega_{ps} = n_s e^2/m_s\epsilon_0$ is the species specific plasma frequency.

2.1.2 Particle Pusher

The particle pusher is the most computationally demanding component for most PIC codes. In *EPOCH* macro-particle momentum is updated using a Boris scheme[56]. The Boris scheme separates the particle push into a rotation around the magnetic field and two half integrations of the electric force. As the Boris method rotates velocities around the magnetic field, energy is conserved and the radius of gyro-orbits remains constant for constant magnetic fields. This quality is essential for modelling magnetized plasmas. To reduce noise the electric and magnetic fields are interpolated from the grid using shape functions evaluated at each macro-particles position. All PIC simulations reported here make use of shape functions which are composed of four quadratic splines. Following the momentum update, the particle position is then updated. Finally, the current is updated using a Esirkepov scheme[57].

2.1.3 Numerical Tuning

The CFL condition means that simulations with larger cell sizes can run in less time-steps than simulations with smaller cell sizes providing that plasma oscillations are well resolved. It is necessary to spatially resolve the physics which is being investigated. This means that if possible, it is desirable to use cell sizes which are comparable to the length scales of the physics of interest. Unfortunately, increasing cell sizes excessively has the unwanted effect of enhancing self-heating. In addition to this, properties of the simulated dispersion curve may be modified when cell sizes are sufficiently large. A trade-off therefore exists which must be hand tuned for the individual simulation which is being considered.

When running PIC codes it is also important to represent the momentum distribution with a sufficiently large number of particles per cell. Each macro-particle in the code drives a current fluctuation. This fluctuation drives fluctuations in the electric and magnetic fields. These fluctuations are often referred to as “noise”, although they arise in a fully self-consistent manner and therefore closely resemble the properties of physical plasmas. Signal to noise ratio typically scales as $1/\sqrt{N}$ where N is the number of events measured. This scaling is also true for PIC simulations, where the noise in the field energy (a squared quantity) scales as $1/N$, where N is the number of particles per cell. When sampling from distributions which are not comprised of particles with a single fixed value of energy, it is possible to adjust individual particle weights to reduce the noise in the initial configuration. In the ideal case, the quantity $\sum_i w_i p_i^2$ should be minimised, where w_i is the macro-particle weight and p_i is the macro-particle momentum. This minimizes the energy associated with particle current fluctuations at initialisation. In practise it is often more effective to simply to increase the number of particles per cell until numerical convergence is attained.

2.2 Analysing Simulation Output

Quantities stored on the simulation grid can be written to disk at user defined time intervals. This section addresses some of the methods which we have used to analyse simulation output. In Figure 2.1 we show the electrostatic field in both physical and wavenumber space for a simulated two-stream instability. The electrostatic field energy is the component of electric field energy aligned with the direction of wave propagation. In a 1D simulation, waves are only free to travel in the direction of the simulation domain, so that the electrostatic field is just E_x. The two-stream instability occurs for a simple linearly unstable system composed of two counter-

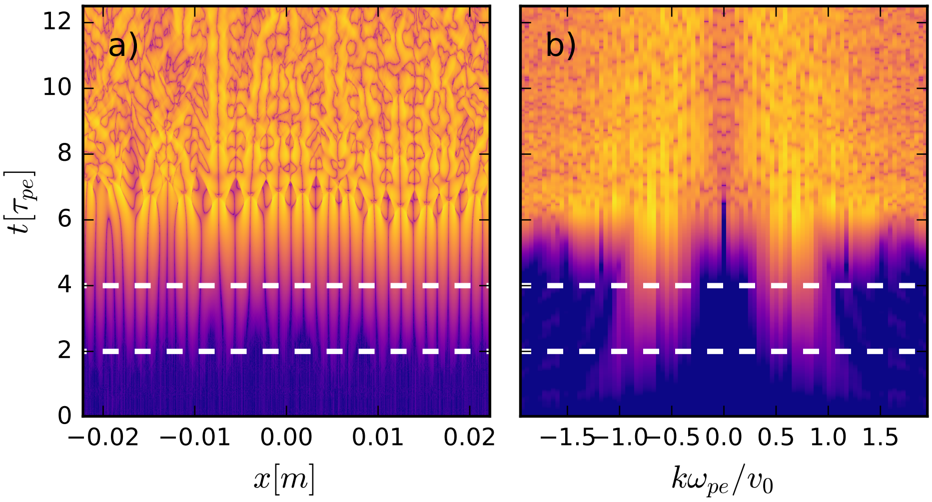

Figure 2.1: Panel a): Spatial electrostatic field energy density evolves in time. Panel b): Spatial Fourier transforms of the electrostatic field evolve in time. The white dashed lines show the upper and lower bounds of the time period which we measure growth rates for.

streaming charged particle beams. We can simulate this using PIC codes. In Section 3.1.1 we derive the linear growth rates for this instability as an introductory problem to calculating growth rates for kinetic instabilities in magnetized gyrotropic plasmas. The result of this derivation is:

$$1 - \frac{\omega_{pe}^2}{2}\left[\frac{1}{(\omega - \mathbf{k}\cdot\mathbf{v}_0)^2} + \frac{1}{(\omega + \mathbf{k}\cdot\mathbf{v}_0)^2}\right] = 0, \tag{2.5}$$

where $\mathbf{k}$ is the wavevector. Here we aim to reproduce this result by performing self consistent PIC simulations. We represent the counter-streaming electron beams using two drifting Maxwellians which have very low thermal temperatures. Here we choose a thermal temperature of $T_e = 0.01\text{eV}$. The electron thermal velocity is defined as $v_{th} = \sqrt{k_B T_e/m_e}$ where k_B is the Boltzmann constant and m_e is the electron mass. A beam velocity of $v_0 = 2000 v_{th}$ is chosen, where each beam contains half of the total electron number density. The total electron number density $n_e = 2.5\times 10^{19} m^{-3}$ defines the electron plasma frequency $\omega_{pe} = \sqrt{e^2 n_e/m_e\epsilon_0}$, where ϵ_0 is the permittivity of free space and e is the elementary charge. This instability evolves rapidly in time. For this reason we output data every $\Delta t = \tau_{pe}/40$, where the plasma oscillation period is $\tau_{pe} = 2\pi/\omega_{pe}$. The simulation was terminated after $20\tau_{pe}$. We perform this 1D simulation in a spatially homogeneous periodic box

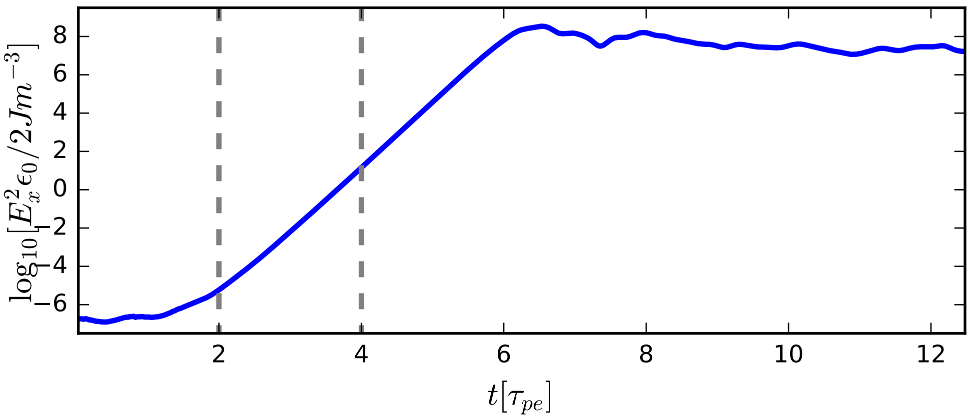

Figure 2.2: Logarithm of spatially integrated electrostatic field power is plotted against time. Linear growth is measured between the two dashed grey lines at times $t_1 = 2\tau_{pe}$ and $t_2 = 4\tau_{pe}$ and is shown in Figure 2.3.

containing 10000 cells of length $\Delta x = 30\lambda_D$, where $\lambda_D = \sqrt{\epsilon_0 k_B T_e/e^2 n_e}$ is the Debye length for the cold electron beams. Although greatly exceeding the Debye length, this cell size is still relatively small for simulations of this type. We highlight that it is not always important to resolve the Debye length in PIC simulations. We used 2000 particles per cell to ensure that the instability was well resolved. This resolution is likely more than is necessary, but is an acceptable use of resources given that the simulation still runs in under one hour on 64 processes.

2.2.1 Measuring Growth Rates

Using the time-series of spatial electrostatic field density which is produced by *EPOCH*, we can measure growth rates from simulation. In Figure 2.2 we show a time-series of the total electrostatic field energy density. In this figure a period of linear growth occurs roughly between times $t_1 = 2\tau_{pe}$ and $t_2 = 6\tau_{pe}$. For times earlier than this, the simulation is dominated by other physics such as spontaneous emission. At time $t \approx 6\tau_{pe}$ wave energy saturation occurs. For times later than this the simulation enters into its non-linear phase of evolution. In this phase it is difficult to predict what may occur from simple linear analysis. We choose to measure growth rates during the first half of the linear phase of evolution between times $2 - 4\tau_{pe}$. This choice is made because the underlying velocity distribution function does not evolve much beyond its initial configuration for these early times. The maximum growth rate in the simulation can be calculated by simply measuring the slope of the blue line which depicts the logarithm of electrostatic power in Figure

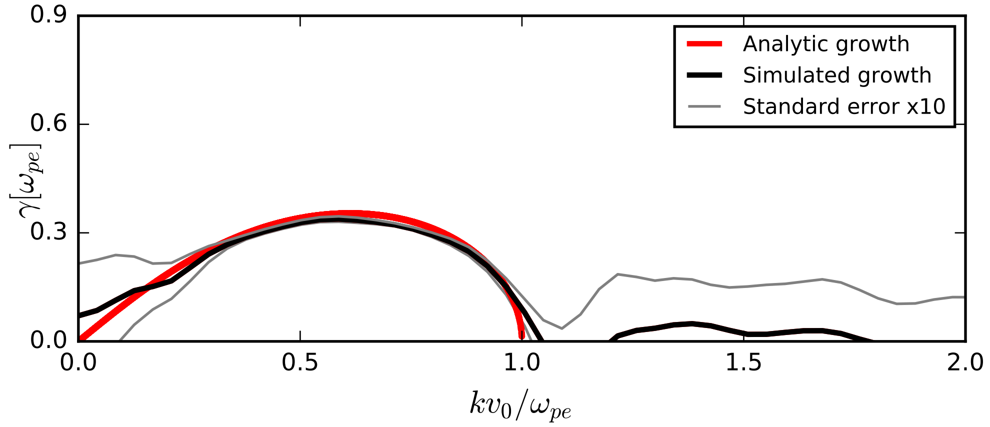

Figure 2.3: Growth rates are plotted as a function of k. Analytic solutions of Equation 2.5 are shown in red. Growth measured from simulation is shown in black. Errors computed from a least square fit are shaded in grey.

2.2. The electric field amplitude grows as $E(t) \propto e^{\gamma t}$ so that the slope of this line will be equal to 2γ, where γ is the growth rate of the instability.

In panel a) of Figure 2.1 it is evident that a spectrum of spatial waves exists. If we first spatially Fourier transform the fields, we can then examine the growth of waves with different wavenumbers separately. The time evolution of the spatial Fourier transform of the electrostatic field is shown in panel b) of Figure 2.1. The frequencies of a discrete Fourier transform are determined by the sampling rate and the number of samples. For a box of length L with grid spacing Δx, the wavenumbers which can be resolved are $k_n = n\pi/L$, where $L = N\Delta x$ and n ranges from $-N/2$ to $N/2$. The maximum wavenumber is equal to $\pi/2\Delta x$. The lowest wavenumber is the fundamental wavenumber and is determined by π/L. In this simulation we have been careful to use a box which is large enough to resolve many low wavenumbers.

Later in this thesis we perform simulations which have 2 spatial dimensions. Spatial Fourier transforms in 2D are simple to perform. Fourier transforms are a linearly independent operation, so that a 1D Fouier transform can be performed in the x direction, followed by a second 1D Fourier transform in the y direction. This gives the wavevector as a grid in k_x and k_y. As the wavevector is a vector quantity, measuring waves propagating at some angle θ from the x direction of a 2D simulation is simply a matter of interpolating quantities along the line $\mathbf{k} = k(\cos\theta, \sin\theta)$ in wavevector space.

Growth can be computed from this time series of spatial Fourier transforms. We construct a time series for the natural logarithm of the absolute value of each Fourier component. A simple least squares fit is then performed on this data. We

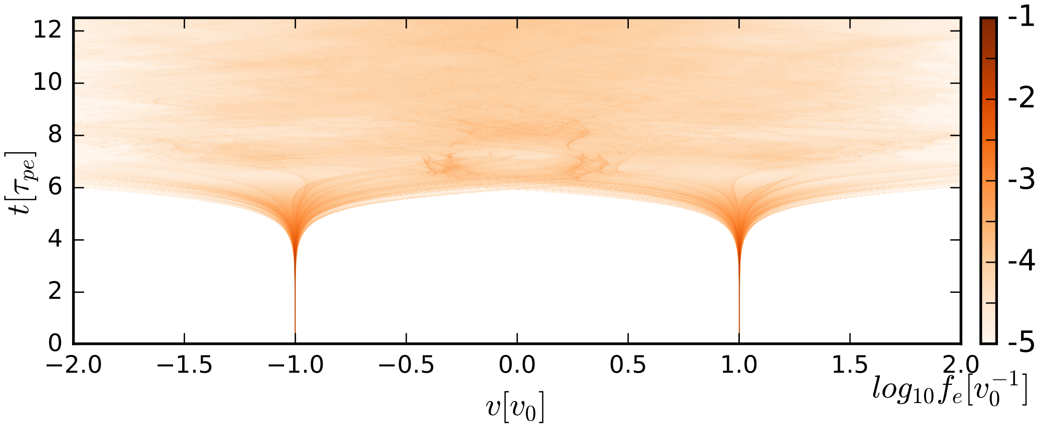

Figure 2.4: Time evolution of the electron velocity distribution as a function of velocity in the direction of the simulation domain.

can compute the variance of the gradient of this fit from the covariance matrix. In Figure 2.3 we show growth rates which have been measured using this technique for the simulation of the two-stream instability. It is evident that very good agreement exists between simulation and the analytical growth rates presented here. The errors computed from the fit are small. Here they have been exaggerated for the purposes of visualization. It is important to note that these are only the standard errors in the fitted gradient and ignore the possible influence of systematic effects.

2.2.2 Particle Distributions

In addition to measuring quantities which are stored on the grid, we can also measure quantities of the particles themselves. In PIC simulations it is typical to work with numbers of macro-particles which would be difficult to store in memory or on disk. It is more appropriate to compute histograms of the particle distribution during the simulation. For this reason it is necessary to choose the properties of the distribution which will be recorded prior to the simulation initialisation. In Figure 2.4 we show the evolution of the particle distribution function in time as a function of velocity in the x direction. During the linear growth phase of the simulation little visible change occurs in the velocity distribution. It is evident that the saturation mechanism for the two-stream instability is that the velocity distribution flattens out. This is followed by a turbulent mixing of phase space and the broadband excitation of many eigenmodes.

2.2.3 Cold Plasma

The theme of magnetized plasmas is important in this thesis. As an introduction to performing simulations describing magnetized plasmas, and to highlight some of the electrodynamics necessary to compute growth rates, we will explore the dispersion relation for a cold magnetized plasma. This very simple description can be surprisingly informative. We begin with the basic equations needed to describe waves in a magnetized plasma. Maxwell's equations state that:

$$\nabla \times \mathbf{E} = -\frac{\partial \mathbf{B}}{\partial t}, \qquad \nabla \times \mathbf{B} = \mu_0 \mathbf{j} + \frac{1}{c^2}\frac{\partial \mathbf{E}}{\partial t}, \tag{2.6}$$

If the electric field is represented as a Fourier series, with components of the form $\mathbf{E}_{\omega,\mathbf{k}} \exp i(\mathbf{k}\cdot\mathbf{r} - \omega t)$, then 2.6 can be combined to give the wave equation:

$$\mathbf{k} \times (\mathbf{k} \times \mathbf{E}) + \frac{\omega^2}{c^2}\mathbf{E} + i\omega\mu_0 \mathbf{j} = \boldsymbol{\phi}, \tag{2.7}$$

where $\boldsymbol{\phi}$ is some vector potential which describes inhomogeneity. Defining the wave normal $\mathbf{n} = \mathbf{k}c/\omega$ and applying Ohm's law $\mathbf{j} = \boldsymbol{\sigma}\cdot\mathbf{E}$ to the homogeneous wave equation, where $\boldsymbol{\sigma}$ describes the conductivity tensor, we arrive at:

$$\mathbf{n} \times (\mathbf{n} \times \mathbf{E}) + \boldsymbol{\epsilon}\cdot\mathbf{E} = \mathbf{0}, \tag{2.8}$$

where the dielectric tensor is defined by $\boldsymbol{\epsilon} = \mathbf{1} + \frac{i\mu_0 c^2}{\omega}\boldsymbol{\sigma}$ and $\mathbf{1}$ is the unit diadic. The equation of motion for a non-relativistic species in a cold magnetized plasma is:

$$m_s \frac{d\mathbf{v}_s}{dt} = q_s(\mathbf{E} + \mathbf{v}_s \times \mathbf{B}), \tag{2.9}$$

where m_s is the species mass and q_s is the species charge. Given that the current density is just $\mathbf{j} = \sum_s q_s n_s \mathbf{v}_s$, it is then possible to solve for the individual elements of the conductivity tensor $\boldsymbol{\sigma}$. The magnetic field can be oriented such that $\mathbf{B}_0 = (0, 0, B_z)$ without loss of generality. The component $\sigma_{z,z}$ is then simple to solve as its solution is independent of the magnetic field. The non-zero conductivity elements $\sigma_{x,x}$, $\sigma_{x,y}$, $\sigma_{y,x}$ and $\sigma_{y,y}$ can be solved as a linear system, giving the multi species cold plasma conductivity tensor:

$$\boldsymbol{\sigma} = \sum_s \begin{bmatrix} i\frac{\omega n_s q_s^2}{m_s(\omega^2-\Omega_{cs}^2)} & -\frac{\Omega_{cs} n_s q_s^2}{m_s(\omega^2-\Omega_{cs}^2)} & 0 \\ \frac{\Omega_{cs} n_s q_s^2}{m_s(\omega^2-\Omega_{cs}^2)} & i\frac{\omega n_s q_s^2}{m_s(\omega^2-\Omega_{cs}^2)} & 0 \\ 0 & 0 & i\frac{n_s q_s^2}{m_s\omega} \end{bmatrix}. \tag{2.10}$$

where the species specific cyclotron frequency is defined as $\Omega_{cs} = q_s B_0/m_s$. In

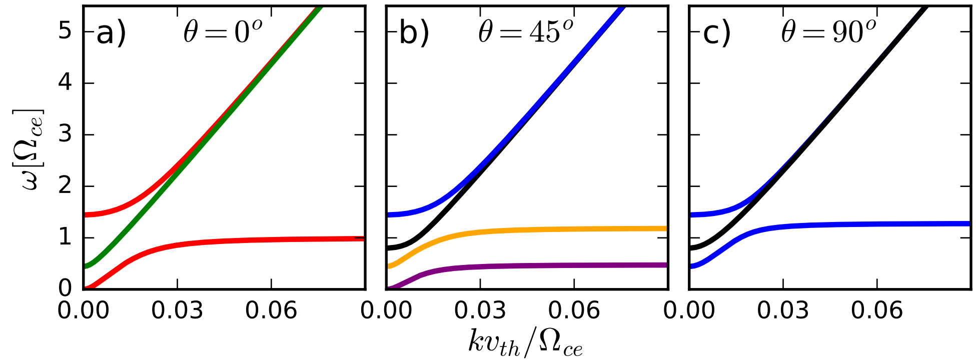

Figure 2.5: Cold plasma dispersion relations are shown for angles $\theta = 0^o$, $\theta = 45^o$ and $\theta = 90^o$ in panels a), b) and c) respectively. All panels are computed for the ratio of $\omega_{pe}/\Omega_{ce} = 0.8$. The right and left whistlers propagating at $\theta = 0^o$ are plotted in red and green. The ordinary mode is plotted in black and the extraordinary mode in blue. The W and Z (upper and lower bulk modes) are shown in orange and purple.

practise the dielectric tensor is more useful than the plasma conductivity tensor. The cold plasma dielectric tensor is:

$$\boldsymbol{\epsilon} = \begin{bmatrix} 1 - \sum_s \frac{\omega_{ps}^2}{\omega^2 - \Omega_{cs}^2} & -i\left(\sum_s \frac{\Omega_{cs}\omega_{ps}^2}{\omega(\omega^2-\Omega_{cs}^2)}\right) & 0 \\ i\left(\sum_s \frac{\Omega_{cs}\omega_{ps}^2}{\omega(\omega^2-\Omega_{cs}^2)}\right) & 1 - \sum_s \frac{\omega_{ps}^2}{(\omega^2-\Omega_{cs}^2)} & 0 \\ 0 & 0 & 1 - \sum_s \frac{\omega_{ps}^2}{\omega^2} \end{bmatrix}. \tag{2.11}$$

where $\omega_{ps} = \sqrt{n_s q_s^2/\epsilon_0 m_s}$ is the species specific plasma frequency. Expressing the wave Equation 2.8 in matrix form and substituting the cold plasma dielectric response tensor 2.11 gives a system of equations which may be solved. Taking the determinant of this system gives a sixth order polynomial for which roots may be found in a purely symbolic manner. Solving these roots gives the well known cold plasma dispersion relation for an arbitrary angle θ, species charges, densities and a background magnetic field.

In Figure 2.5 we plot solutions to Equation 2.8 for angles $\theta = 0^o$, $\theta = 45^o$ and $\theta = 90^o$ from the magnetic field direction. These solutions are computed for a ratio of plasma frequency to electron cyclotron frequency of $\omega_{pe}/\Omega_{ce} = 0.8$. The ordinary "O" wave is plotted in black. The dispersion relation for this mode, $\omega^2 = \omega_{pe}^2 + k^2c^2$, is unaffected by the presence of a magnetic field and is characterized by a frequency cut-off at $\omega = \omega_{pe}$ when $k = 0$. Right and left polarized whistler waves are shown in red and green respectively. The dispersion relations for these modes may be described by $k^2c^2 = \omega^2 - \frac{\omega_{pe}^2}{1-\Omega_{ce}/\omega_{pe}}$ and $k^2c^2 = \omega^2 - \frac{\omega_{pe}^2}{1+\Omega_{ce}/\omega_{pe}}$. The right whistler frequency cutoffs occur at $\omega_R = \frac{1}{2}\left(\sqrt{\Omega_{ce}^2 + 4\omega_{pe}^2} + \Omega_{ce}\right)$ and $\omega = 0$ while the left whistler frequency cutoff occurs at $\omega_L = \frac{1}{2}\left(\sqrt{\Omega_{ce}^2 + 4\omega_{pe}^2} - \Omega_{ce}\right)$. The lower right polarized whistler branch has a resonance at the electron cyclotron frequency. The extraordinary or "X" mode is plotted in blue and is described by the dispersion relation $k^2c^2 = \omega^2 - \omega_{pe}^2 \frac{\omega^2 - \omega_{pe}^2}{\omega^2 - \omega_h^2}$, where $\omega_h^2 = \omega_{pe}^2 + \Omega_{ce}^2$ is the upper hybrid frequency. Frequency cutoffs for the upper and lower extraordinary modes occur at ω_R and ω_L, the same as those for the right and left polarized whistlers. The extraordinary mode has a resonance at the upper hybrid frequency. Modes propagating at angles between 0^o and 90^o are sometimes denoted by the letters "W" and "Z", but we prefer the nomenclature upper bulk mode and lower bulk mode. The resonance for these modes occurs at:

$$\omega_{U,L}^2 = \frac{1}{2}\omega_h^2 \pm \frac{1}{2}\sqrt{\omega_h^4 - 4\Omega_{ce}^2\omega_{pe}^2 \cos^2\theta}, \tag{2.12}$$

and the frequency cutoffs are identical to those of the purely perpendicular and parallel modes.

2.2.4 Spatiotemporal Fourier Transforms

In Section 2.2.1 we analysed data using only spatial Fourier transforms. Spatial Fourier transforms can then be Fourier transformed in time. The resultant spatiotemporal Fourier transform is the dispersion relation. The signal analysis uncertainty principle states that:

$$\Delta\omega\Delta t \geq \frac{1}{2} \tag{2.13}$$

where $\Delta\omega$ is the frequency resolution and Δt is the time resolution. There is a fundamental limit on the frequency resolution which can be attained for a given time resolution. This means that it is only sensible to perform temporal Fourier transforms when the envelope of the oscillating signal varies slowly in time. The signal which we analysed in Section 2.2.1 grows too quickly in time for good frequency resolution to be attained.

Simulation data is not typically periodic in time. Performing Fourier transforms on signals which are not periodic will typically produce artefacts. To avoid this, we first multiply the signal by a Hann window[58]. A Hann window is defined as:

$$H(n) = \sin^2\left(\frac{\pi n}{N-1}\right) \tag{2.14}$$

where n is the index of the sample and N is the number of samples. When this window is multiplied by a signal, then Fourier transformed, the resulting spectrum has a slightly reduced frequency resolution but much less aliasing. This is advantageous for visualization.

To demonstrate the agreement between the analytical cold plasma dispersion relation which we computed in Section 2.2.3 and the dispersion relation which can be computed from PIC simulation, we perform a simple 1D simulation of a magnetized plasma in a periodic box. This simulation is performed with a background magnetic field oriented at 90^o to the direction of the simulation domain. The background magnetic field strength is $B = 2T$ and the electron number density is $n_e = 2.5{\times}10^{19} m^{-3}$, so that the ratio $\omega_{pe}/\Omega_{ce} = 0.8$. Although not strictly required, a population of protons is added. The electron and proton temperatures are initialized to $T_e = T_p = 1$keV. The simulation is performed with 1000 particles per cell, 1000 cells and a cell size of $\Delta x = \lambda_D$, where the Debye length is $\lambda_D = \sqrt{\epsilon_0 k_B T_e / n_e e^2}$. The simulation was performed for $100\tau_{ce}$, where $\tau_{ce} = 2\pi/\Omega_{ce}$.

2.2.5 Polarization of Electromagnetic Waves

An electrostatic wave is a wave for which the electric field oscillates in the direction parallel to the direction of wave propagation. The electric field of an electromagnetic wave oscillates in a direction perpendicular to the direction of wave propagation. Because there are two directions perpendicular to wave propagation, electromagnetic waves can be left, right or plane polarized, depending on the phase difference (or lack of) between the individual oscillating components. The polarization may be fully described by an ellipse rotated by an angle of orientation.

In a magnetized plasma waves can have components which are partially electrostatic and partially electromagnetic. Here the terminology “degree of electromagnetic polarization” is used to describe the degree to which a wave is electrostatic or electromagnetic. A wave which is fully electromagnetic has a degree of electromagnetic polarization of $\pi/2$, while a wave which is fully electrostatic has a degree of electromagnetic polarization of 0.

We can describe these quantities using either simulation or by solving the wave Equation 2.8. All three vector components of the simulated electric field may be independently spatio-temporally Fourier transformed. This gives the quantities $\hat{E}_{x,\omega,\mathbf{k}}$, $\hat{E}_{y,\omega,\mathbf{k}}$ and $\hat{E}_{z,\omega,\mathbf{k}}$. The degree of electromagnetic polarization may then be evaluated by computing DoEP $= \cos^{-1}\left(|\hat{\mathbf{E}}_{\omega,\mathbf{k}} \cdot \mathbf{k}|/|\mathbf{k}||\hat{\mathbf{E}}_{\omega,\mathbf{k}}|\right)$. This quantity is evaluated from simulation and plotted in the left panel of Figure 2.6. We can compare simulated DoEP to DoEP calculated by solving the wave equation for a

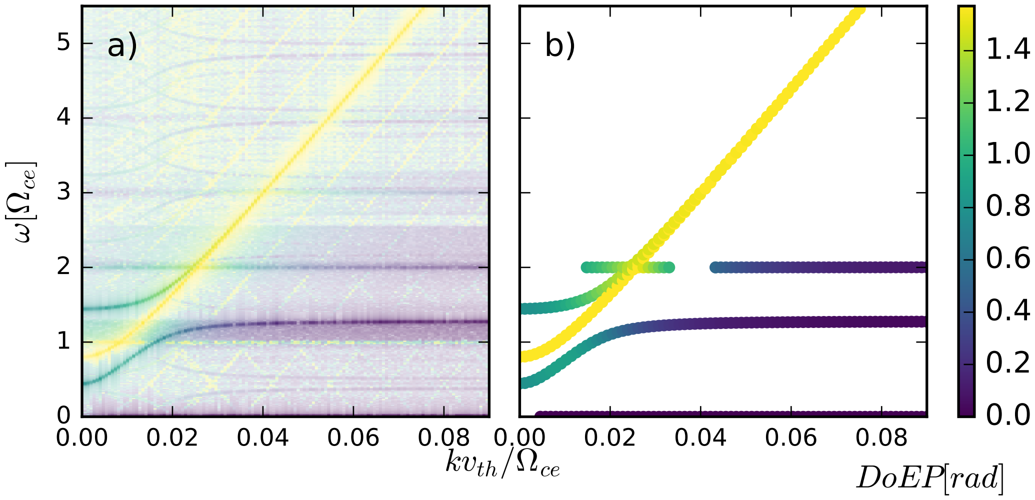

Figure 2.6: Panel a): Degree of electromagnetic polarization is computed from simulation at angle $\theta = 90^o$. Panel b): Corresponding degree of electromagnetic polarization is computed by solving the eigenvectors of Equation 2.8. Purely electromagnetic modes are shown in yellow and purely electrostatic modes are shown in purple. Panel a) is colourized according to the power density, so that white regions have low power.

cold plasma dielectric tensor. For a non singular 3×3 matrix there are three pairs of eigenvalues and corresponding linearly independent eigenvectors. Solutions to Equation 2.8 exist when one of the eigenvalues is zero. The eigenvector $\mathbf{E}_\lambda(\omega, \mathbf{k})$ corresponding to the zero-eigenvalue solution may be treated in the same manner as the electric field components produced in simulation. The degree of electromagnetic polarization is computed from $\mathbf{E}_\lambda(\omega, \mathbf{k})$ and shown in panel b) of Figure 2.6. The simulated DoEP on the left panel agrees very well with the DoEP computed by solving the cold plasma wave equation shown on the right panel. As would be expected, the "O" mode is purely electromagnetic, and the lower right whistler mode and second electron cyclotron harmonic are electrostatic at large k.

Chapter 3

Linear Physics in Gyrotropic Magnetized Plasmas

3.1 Introduction

It is useful to have a means available for computing linear growth rates for instabilities in magnetized plasmas driven by arbitrary gyrotropic velocity distributions. This would allow us to better predict the linear evolution of waves in plasmas given that sufficient information about their bulk parameters was known. This knowledge would both allow us to predict and benchmark the results from either particle-in-cell simulations at early times, or physical plasmas, particularly in terms of their stability properties. While many papers address the analytic solutions for a particular form of velocity distribution within a particular range of bulk parameters, these works typically make approximations which may limit their scope. We therefore examine an alternative approach.

In this chapter we begin by exploring some of the previous techniques used to calculate linear growth rates for velocity dependent plasma instabilities. We initially focus on two approaches, each covering similar physics but valid in different regimes. These are the hydrodynamic and kinetic regimes of instability. We next outline the much more involved derivation of a gyrotropic plasma susceptibility tensor. Knowledge of this tensor enables calculation of the dispersive properties of waves in magnetized plasmas.

We then discuss how exact solutions of this quantity are not simple to attain and that a numerical approach may instead be employed. In this chapter we outline the construction of two modules of a code, one which will describe solutions in the non-relativistic approximation and one which is fully relativistic. These codes are extensively benchmarked and their numerical performance is also considered. To begin with let us derive of one of the simplest velocity dependent plasma instabilities.

3.1.1 Two-Stream Instability and the Hydrodynamic Regime

One of the most well known collective plasma instabilities is the "two-stream instability". We will briefly summarize its derivation, both to act as a benchmark problem for later work in this chapter, and to outline the relevant approximations and conditions for its validity. The original work on this instability and its practical use as a two-stream amplifier was carried out in 1948[59–62]. The two-stream instability in its simplest form occurs when two opposing electron beams interact. Free energy is transferred from the counter-streaming electron beams into resonantly excited electrostatic waves. The initial exponential growth in amplitude of these waves is an example of a linear instability. The occurrence of two-stream instabilities is not limited to electrons, or indeed to charged particles. It may occur between any number of streaming charged particle species, or between massive bodies interacting gravitationally on interstellar or cosmological scales[63]. While the existence of this instability has been known for a significant time, its properties are still an area of active research particularly in the fully non-linear regime[64, 65].

The two-stream instability can be addressed by treating each individual beam population as a distinct cold fluid element. This means that kinetic effects caused by the velocity spread of particle distributions are not accounted for; in other words, it is a hydrodynamic description. To derive the dispersion relation for two counter streaming cold beams we apply a relatively simple process involving the linearization of fluid equations. We start with the continuity equation for a cold collisionless fluid and the equation of motion for a charged fluid in an electric field:

$$\frac{\partial n_s}{\partial t} + \nabla \cdot (n_s \mathbf{v}_s) = 0, \qquad \frac{\partial \mathbf{v}_s}{\partial t} + (\mathbf{v}_s \cdot \nabla)\mathbf{v}_s = \mathbf{E}\frac{q_s}{m_s}, \qquad (3.1,\ 3.2)$$

where s is a species label. Consider two separate electron species s_1 and s_2 with identical number densities $n_{01} = n_{02}$, where $n_{01} + n_{02} = n_e$, and opposing velocities $\mathbf{v}_{01} = -\mathbf{v}_{02}$. The electric field is given a small oscillating perturbation $\mathbf{E} = \mathbf{E}_1 \exp[i(\mathbf{k} \cdot \mathbf{r} - \omega t)]$ such that each species specific velocity is described by $\mathbf{v}_s = \mathbf{v}_{0s} + \mathbf{v}_{1s} \exp[i(\mathbf{k} \cdot \mathbf{r} - \omega t)]$ and species specific number density is described by $n_s = n_{0s} + n_{1s} \exp[i(\mathbf{k} \cdot \mathbf{r} - \omega t)]$. Substituting these expressions into equations 3.1 and 3.2 give us the following two expressions:

$$-\omega n_{1s} + n_{1s}\mathbf{k} \cdot \mathbf{v}_{0s} + n_{0s}\mathbf{k} \cdot \mathbf{v}_{1s} = 0, \qquad (3.3)$$

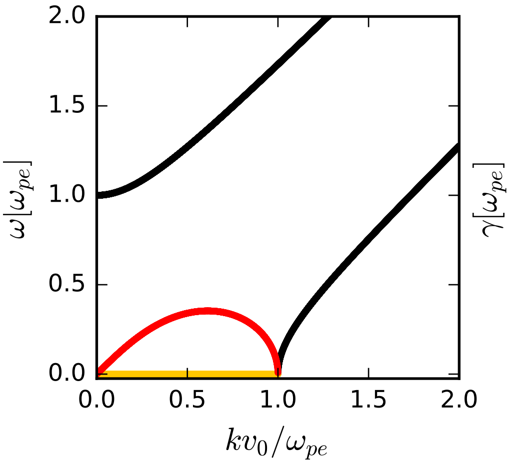

Figure 3.1: Numerical solution to Equation 3.7 describing two counter-streaming plasmas each with density $\frac{1}{2}n_e$ and velocity $\pm v_0$. Stationary solutions are depicted in black while the real part of growing solutions is shown in yellow. The corresponding imaginary component of growing solutions is shown in red.

$$-\omega \mathbf{v}_{1s} + (\mathbf{k}\cdot\mathbf{v}_{0s})\mathbf{v}_{1s} = -i\frac{q_s}{m_s}\mathbf{E}_1. \tag{3.4}$$

These may be combined to solve for either n_{1s} or $\mathbf{v}_{1s}$. We solve for n_{1s},

$$n_{1s} = \frac{iq_s n_0 \mathbf{k}\cdot\mathbf{E}_1}{m_s(\omega - \mathbf{k}\cdot\mathbf{v}_{0s})^2}. \tag{3.5}$$

Equation 3.5 may be applied to both of the counter-streaming species, and these two expressions are then coupled through Gauss's Law, which in linearized form becomes:

$$i\mathbf{k}\cdot\mathbf{E}_1 = \sum_s \frac{n_{1s}q_s}{\epsilon_0}. \tag{3.6}$$

Evaluating this equation using Equation 3.5 and noting the definition of the electron plasma frequency $\omega_{pe} = \sqrt{n_e e^2/m_e\epsilon_0}$, we arrive at an expression which is quartic in ω:

$$1 = \frac{\omega_{pe}^2}{2}\left[\frac{1}{(\omega + \mathbf{k}\cdot\mathbf{v}_0)^2} + \frac{1}{(\omega - \mathbf{k}\cdot\mathbf{v}_0)^2}\right] \tag{3.7}$$

Multiple solutions for Equation 3.7 exist where the wave frequency ω is purely real or complex. The physical meaning of a complex solution is that the envelope for a small oscillating perturbation is either growing or damping in time depending on whether the sign of the imaginary component of ω, hereafter denoted $\gamma = \omega_i$, is positive or negative. These are computed numerically and shown in Figure 3.1. For a given orientation of $\mathbf{k}$ with respect to $\mathbf{v_0}$, Equation 3.7 yields an expression for ω in terms of k which only depends on the two free parameters ω_{pe} and v_0, the specific values of each are not important provided that the axes variables ω and k are scaled appropriately. It is clear to see that this particular configuration is highly unstable with a maximum linear growth rate of $\gamma = \frac{1}{3}\omega_{pe}$ at $\omega_r = 0$ and $k = \frac{\omega_{pe}}{v_0}$. We now move on to the case where particle velocity distributions cannot simply be modelled by fluid equations.

3.1.2 Landau Damping and the Kinetic Regime

Many problems require a physical description containing a continous probability distribution of particles in velocity space, rather than a set of discrete particle beams. In this section we review the classical techniques that are used to calculate the growth and damping rates for plasma systems of the continuum type.

In principle the approach that was applied in Section 3.1.1 to the two-stream instability may also be applied to particle distribution functions. By combining the linearized collisionless Boltzmann (Vlasov) equation with the linearized Poisson equation, a solution should be attainable. However problems arise with the occurrence of singularities, a challenge first solved by Landau in 1946[66]. In this section we will briefly summarize the derivation originally performed by Landau and his solution to the damping of electrostatic waves travelling through a homogeneous Maxwellian particle distribution.

We again consider the application of a small perturbation, this time to an underlying particle probability distribution $f_0(\mathbf{v})$ which is spatially homogeneous and is not subject to any externally applied magnetic field:

$$f = f_0(\mathbf{v}) + f_1(\mathbf{v}, \mathbf{r}, t). \tag{3.8}$$

We choose to normalize f_0 such that $\int_{-\infty}^{\infty} f_0(\mathbf{v})d^3\mathbf{v} = 1$, where $f_1 \ll f_0$. This means that the species specific particle number density n_s must also be tracked in addition to f. Next we consider the collisionless Boltzmann equation under the action of an electric field $\mathbf{E}$ for particles with charge q_s and mass m_s

$$\frac{\partial f}{\partial t} + \mathbf{v} \cdot \nabla f = -\frac{q_s}{m_s}\mathbf{E} \cdot \frac{\partial f}{\partial \mathbf{v}} = 0. \tag{3.9}$$

Following the approach used in the previous section, we linearise Equation 3.9 through spatially Fourier transforming it. If the electric field is treated as having only a dependence on the first order perturbation such that $\mathbf{E} = \mathbf{E}_1$ then the two left-hand terms of Equation 3.9 are equal to the continuity equation and cancel for zeroth order terms. Neglecting terms that are quadratic in the perturbed quantities, we arrive at:

$$\frac{\partial f_{1k}}{\partial t} + i\mathbf{v}\cdot\mathbf{k}f_{1k} = -\frac{q_s}{m_s}\mathbf{E}_{1k}\cdot\frac{\partial f_0}{\partial \mathbf{v}}. \tag{3.10}$$

We couple this equation with the linearized Poisson equation:

$$i\mathbf{k}\cdot\mathbf{E}_{1k} = \frac{n_s q_s}{\epsilon_0}\int_{-\infty}^{\infty} f_{1k}(\mathbf{v})d^3\mathbf{v}, \tag{3.11}$$

for the velocity distribution of a single particle species with charge q_s and density n_s. To adhere to the mathematical rigour applied in the original Landau derivation, we apply a temporal Laplace transform over the complex variable p,

$$f_{k,p}(\mathbf{v}) = \int_0^{\infty} f_k(\mathbf{v},t)e^{-pt}dt. \tag{3.12}$$

This procedure is applied to both equations 3.10 and 3.11:

$$pf_{1k,p} - g_k + i\mathbf{v}\cdot\mathbf{k}f_{1k,p} = -\frac{q_s}{m_s}\mathbf{E}_{1k,p}\cdot\frac{\partial f_0}{\partial \mathbf{v}}, \tag{3.13}$$

$$i\mathbf{k}\cdot\mathbf{E}_{1k,p} = \frac{n_s q_s}{\epsilon_0}\int_{-\infty}^{\infty} f_{1k,p}(\mathbf{v})d^3\mathbf{v}, \tag{3.14}$$

where the function $g_k(\mathbf{v}) = f_{1k}(\mathbf{v}, t=0)$ is just the spatial Fourier transform of the initial perturbed velocity distribution function. Equation 3.13 may be arranged for f_p then substituted into Equation 3.14 to give an expression for $\mathbf{E}_{1k,p}$

$$\mathbf{E}_{1k,p}\cdot\left(i\mathbf{k} + \frac{n_s q_s^2}{m_s\epsilon_0}\int_{-\infty}^{\infty}\frac{\partial f_0/\partial\mathbf{v}}{p+i\mathbf{k}\cdot\mathbf{v}}d^3\mathbf{v}\right) = \frac{n_s q_s}{\epsilon_0}\int_{-\infty}^{\infty}\frac{g_k}{p+i\mathbf{k}\cdot\mathbf{v}}d^3\mathbf{v}. \tag{3.15}$$

This may now, in principle be solved for some initial distribution perturbation $g(\mathbf{v})$. If we assume that the electric field perturbation is of the form $\mathbf{E}_1 = \mathbf{E}_{1k,p}\exp[i\mathbf{k}\cdot\mathbf{r} - i\omega t + \gamma t]$, then when $p \approx i\omega - \gamma$ the term $\mathbf{E}_{1k,p}$ will be very large. That means that the right-hand side of Equation 3.15 may be neglected. We note that the Laplace transform is only valid for positive growth rates, and arrive at:

$$k + \omega_{ps}^2\int_{-\infty}^{\infty}\frac{\partial f_0/\partial v_{\|}}{\omega + i\gamma - kv_{\|}}dv = 0, \qquad \text{for } \gamma > 0. \tag{3.16}$$

Here we have integrated over two of the velocity dimensions, k denotes the magnitude

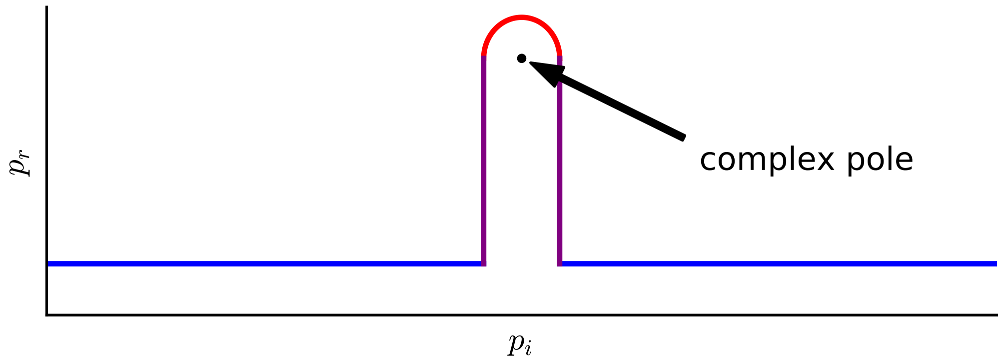

Figure 3.2: The Landau contour for damped modes, where $p = i\omega_r - \gamma$ and γ is negative.

of wavevector $\mathbf{k}$, and $v_{\|}$ is the component of $\mathbf{v}$ along $\mathbf{k}$. Landau observed that this solution could also be generalised to the case where growth rates are not positive, hence one must consider the variable p on the complex plane. Previously we have stated that solutions are valid only when p lies on the negative region of the complex plane, when $Re(p) < 0$. As long as we always approach the singularity from this side of the complex plane, we may extend Equation 3.16 to be valid for positive values of $Re(p)$, illustrated in Figure 3.2. The additional complex residue imposed by approaching the singularity from the lower half of the plane is equal to $2\pi i F(v_{\|})$, where the holomorphic (complex differentiable) function $F(v_{\|}) = (\omega_{ps}^2/k)\partial f_0/\partial v_{\|}$ is evaluated at the point $v_{\|} = \omega/k$. The resulting integral, which is valid for growth rates where $\gamma < 0$, is thus:

$$k + \omega_{ps}^2 \int_{-\infty}^{\infty} \frac{\partial f_0/\partial v_{\|}}{\omega + i\gamma - kv_{\|}} dv_{\|} - \frac{2\pi i \omega_{ps}^2}{|k|} \frac{\partial f_0(v_{\|})}{\partial v_{\|}}\bigg|_{v_{\|}=\omega_r/k} = 0, \qquad \text{for } \gamma < 0. \tag{3.17}$$

From here onwards we choose to follow Dendy[67], although many other accounts of Landau damping exist. We approximate the solution to Equation 3.17 through splitting it into components dominated by real and imaginary parts, then applying perturbation theory. We note here that this approach is only valid when γ is small compared to the real frequency ω_r. It is valid in the "kinetic" regime. The sum of equations 3.17 and 3.16 is simply an expression for k times the dielectric permittivity ϵ,

$$\epsilon(\omega, k) = \epsilon_r(\omega, k) + \epsilon_i(\omega, k) = 0. \tag{3.18}$$

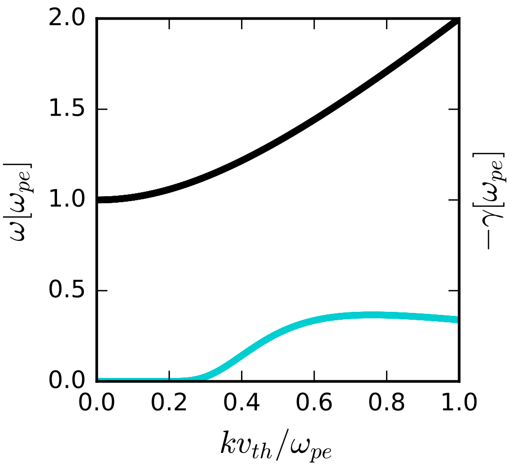

Figure 3.3: The analytical solution for Landau damping is computed from the kinetic description. The real frequency $\omega_r^2 = \omega_{pe}^2 + \frac{3}{2}k^2 v_{th}^2$ is plotted in black, while the corresponding damping rate calculated using Equation 3.21 for a Maxwellian electron distribution is plotted in cyan.

Here the real and imaginary terms are split as follows:

$$\epsilon_r = 1 + \frac{\omega_{ps}^2}{k} P \int_{-\infty}^{\infty} \frac{\partial f_0/\partial v_{\|}}{\omega + i\gamma - kv_{\|}} dv_{\|}, \tag{3.19}$$

$$\epsilon_i = -\frac{\pi i \omega_{ps}^2}{k|k|} \frac{\partial f_0(v_{\|})}{\partial v_{\|}}\bigg|_{v_{\|}=\omega/k}. \tag{3.20}$$

The Cauchy principal integral denoted by the P in Equation 3.19 may be evaluated by Taylor expanding when $kv_{\|}/\omega \ll 1$, giving the solution $\epsilon_r = 1 - \omega_{pe}^2/\omega^2 - 3\omega_{pe}^2 k^2 v_{th}^2/\omega^4 + O[\omega^{-4}]$. Ignoring higher order thermal terms, the expression $\omega = \omega_r + i\gamma$ may be reintroduced into this expression for ϵ_r, and Equation 3.18 solved. Combining the imaginary components this expression gives $2i\omega_r\gamma + \omega_r^2\epsilon_i = 0$. The previous term for ϵ_i may now be reintroduced, giving us a formula for the linear growth rate of Landau damping:

$$\gamma = \frac{\pi\omega\omega_p^2}{2k|k|}\left[\frac{\partial f(v)}{\partial v}\right]_{v=\omega/k}. \tag{3.21}$$

Inspecting this equation yields some important results. When the slope of the underlying distribution function is positive, electrostatic waves will grow in time. Likewise, when the slope is negative, these waves will be damped, a process known as “Landau damping”. In Figure 3.3 we illustrate a thermal Maxwellian plasma with an electron distribution in the wave propagation direction $f_e(v_\parallel) = \sqrt{1/2v_{th}^2} exp[-v_\parallel^2/2v_{th}^2]$, where v_{th} describes the electron thermal velocity. Scaling with respect to bulk parameters in Figure 3.3 follows from the normalization of the ω and k axes with respect to ω_{pe} and ω_{pe}/v_{th} respectively. We note also that the Debye length $\lambda_D = v_{th}/\omega_{pe}$. Now that we have indicated the main differences between the hydrodynamic and kinetic approaches to solving dispersion relations, let us move onto the case where a background magnetic field plays an important role.

3.1.3 Waves in Gyrotropic Magnetized Plasma

Many of the problems which we will consider require the inclusion of a guiding magnetic field. To effectively calculate linear growth rates in a magnetized plasma, we need to follow an approach which is slightly more complex than the unmagnetized case. The following was first developed in the late 1950s, motivated by the need to calculate microwave absorption and emission coefficients in magnetized plasmas[68]. We base this derivation instead on the textbook "Waves in Plasmas" by T. H. Stix[69]. Once again, we first consider the Vlasov equation:

$$\frac{df}{dt} = \frac{\partial f}{\partial t} + \frac{\partial f}{\partial \mathbf{r}} \cdot \frac{d\mathbf{r}}{dt} + \frac{\partial f}{\partial \mathbf{p}} \cdot \frac{d\mathbf{p}}{dt} = 0, \tag{3.22}$$

this time placing emphasis on the retention of the relativistic momentum term $\mathbf{p} = \Gamma m_0 \mathbf{v}$, where the Lorentz factor is defined as $\Gamma = \sqrt{1/(1-|\mathbf{v}|^2/c^2)}$. The retention of relativistic effects is necessary to capture certain physical processes, particularly for waves travelling close to the magnetic field direction. When calculating the Lorentz force, we must now include the magnetic field $\mathbf{B}$, so that the force term in the Vlasov equation is:

$$\frac{d\mathbf{p}}{dt} = q_s(\mathbf{E} + \frac{\mathbf{v}}{c} \times \mathbf{B}). \tag{3.23}$$

This is again split into zero order quantities and first order quantities, $\mathbf{E} = \mathbf{E}_1$ and $\mathbf{B} = \mathbf{B}_0 + \mathbf{B}_1$ such that the system is now characterized by a static guiding magnetic field $\mathbf{B}_0$ who's direction defines a spatial coordinate axis, whereas the small perturbations $\mathbf{E}_1$ and $\mathbf{B}_1$ may be oriented in arbitrary directions. The zero order solution to Equation 3.22 is now:

$$\frac{df_0}{dt} = \frac{\partial f_0}{\partial t} + \mathbf{v} \cdot \nabla f_0 + q_s(\frac{\mathbf{v}}{c} \times \mathbf{B}_0) \cdot \frac{\partial f_0}{\partial \mathbf{p}} = 0, \tag{3.24}$$

where the two leftmost terms vanish because f_0 is conserved along unperturbed particle paths in phase space. A corollary is that $\mathbf{v} \times \mathbf{B}_0$ is perpendicular to $\partial f_0 / \partial \mathbf{p}$, hence particles of species s travel in helical motion with gyrofrequency Ω_{cs}. The first order description of Equation 3.22 is then:

$$\frac{df_1}{dt} = \frac{\partial f_1}{\partial t} + \mathbf{v} \cdot \nabla f_1 + q_s (\mathbf{E}_1 + \frac{\mathbf{v}}{c} \times \mathbf{B}_1) \cdot \frac{\partial f_0}{\partial \mathbf{p}}, \tag{3.25}$$

where we neglect terms that are quadratic in first order quantities. We now replace the first order magnetic field term using the linearized Maxwell induction relationship for an oscillating electric field perturbation $\mathbf{B}_1 = (\mathbf{k}c/\omega) \times \mathbf{E}_1$. This leaves us with terms involving multiple cross products. For compactness of notation we express these in matrix form,

$$\frac{df_1}{dt} = q_s \mathbf{E}_1 \cdot \left[\mathbf{1} \left(1 - \frac{\mathbf{v} \cdot \mathbf{k}}{\omega} \right) + \frac{\mathbf{v}\mathbf{k}}{\omega} \right] \cdot \frac{\partial f_0}{\partial \mathbf{p}}, \tag{3.26}$$

where $\mathbf{1}$ is the unit dyadic and $[\mathbf{v}\mathbf{k}]_{ij} \equiv v_i k_j$. We apply a spatial Fourier transform combined with a temporal Laplace transform to $\mathbf{E}_1$. The initial distribution term $g(\mathbf{p})$ is omitted here as we have made the asymptotic field approximation $\mathbf{E}(\mathbf{r}', t') = \mathbf{E}_{\omega,\mathbf{k}} \exp(i\mathbf{k} \cdot \mathbf{r}' - i\omega t')$, which is valid when the influence of the initial distribution perturbation $g(\mathbf{p})$ is small. In this limit we may integrate from $t' = -\infty$ to $t' = t$.

$$f_1(\mathbf{r}, \mathbf{p}, t) = -q_s \int_{-\infty}^{t} \exp[i\mathbf{k} \cdot \mathbf{r}' - i\omega t'] \mathbf{E}_{\omega,\mathbf{k}} \cdot \left[\mathbf{1} \left(1 - \frac{\mathbf{v}' \cdot \mathbf{k}}{\omega} \right) + \frac{\mathbf{v}'\mathbf{k}}{\omega} \right] \cdot \frac{\partial f_0(\mathbf{p}')}{\partial \mathbf{p}'} dt'. \tag{3.27}$$

To progress further it is convenient to transform from Eulerian to Lagrangian coordinates, in a frame where the gyrating particle is at rest. In these coordinates the variables τ, $\mathbf{v}'$, $\mathbf{r}'$ and $\mathbf{k}$ are defined as follows:

$$\tau = t - t'$$

$$\mathbf{v}' = \left(v_\perp \cos(\phi + \Omega_{cs}\tau), v_\perp \sin(\phi + \Omega_{cs}\tau), v_\parallel \right),$$

$$\mathbf{r}' = \mathbf{r} + \left(-\frac{v_\perp}{\Omega_{cs}} [\sin(\phi + \Omega_{cs}\tau) - \sin(\phi)], \frac{v_\perp}{\Omega_{cs}} [\cos(\phi + \Omega_{cs}\tau) - \cos(\phi)], -v_\parallel \tau \right),$$

$$\mathbf{k} = \left(k_\perp \cos(\theta), k_\perp \sin(\theta), k_\parallel \right)$$

We now introduce these variables into Equation 3.27. The algebra here now becomes extremely unwieldy. Should the reader wish to reproduce this particular step of the derivation, we suggest that a symbolic algebra package may be helpful. Following

Ref[69], Equation 3.27 yields the expression,

$$f_1(\mathbf{r},\mathbf{p},t) = -q_s \exp[i\mathbf{k}\cdot\mathbf{r} - i\omega t]\int_0^\infty \exp[i\beta]\Big\{E_x U\cos(\phi+\Omega_{cs}\tau) \\ +E_y U\sin(\phi+\Omega_{cs}\tau) + E_z\left[\frac{\partial f_0}{\partial p_\parallel} - V\cos(\phi-\theta+\Omega_{cs}\tau)\right]\Big\}\,d\tau, \quad (3.28)$$

here the variables

$$U = \frac{\partial f}{\partial p_\perp} + \frac{k_\parallel}{\omega}\left(v_\perp\frac{\partial f}{\partial p_\parallel} - v_\parallel\frac{\partial f}{\partial p_\perp}\right), \quad (3.29)$$

$$V = \frac{k_\perp}{\omega}\left(v_\perp\frac{\partial f_0}{\partial p_\parallel} - v_\parallel\frac{\partial f_0}{\partial p_\perp}\right), \quad (3.30)$$

$$W = \left(1 - \frac{n\Omega_{cs}}{\omega}\right)\frac{\partial f}{\partial p_\parallel} + \frac{n\Omega_{cs}p_\parallel}{\omega p_\perp}\frac{\partial f}{\partial p_\perp} \quad (3.31)$$

are just convenient combinations of partial derivatives. The remaining expressions in Equation 3.28, namely $\exp[i\beta]$, contains trigonometric identities of ϕ which are nested within the exponential. The variable β is defined,

$$\beta = \frac{k_\perp v_\perp}{\Omega_{cs}}[\sin(\phi-\theta+\Omega_{cs}\tau) - \sin(\phi-\theta) + (\omega - k_\parallel v_\parallel)\tau]. \quad (3.32)$$

The two identities,

$$\exp[iz\sin\phi] = \sum_{n=-\infty}^{\infty} J_n(z)\exp[in\phi],$$

$$\exp[-iz\sin(\phi+\Omega\tau)] = \sum_{m=-\infty}^{\infty} J_m(z)\exp[-im(\phi+\Omega\tau)],$$

may be applied to the expression $\exp[i\beta]$, giving an expression containing two infinite sums multiplied together. We note that here, the Bessel function of the first kind is denoted by J_n and its derivative with respect to argument $z = k_\perp v_\perp/\Omega_{cs}$ is denoted by J_n'. We then integrate over gyrophase by performing the integral $\int_0^{2\pi} f_1(\mathbf{r},\mathbf{p},t)d\phi$ and eliminate one of the infinite sums through applying orthogonality relations when $n \neq m$ for J_n or when $n\pm 1 \neq m$ for $2J_n' = J_{n-1} - J_{n+1}$. Following significant algebra this results in an expression which describes the first order distribution perturbations for an arbitrary gyrotropic distribution function. It is again convenient to express this in matrix form when considering the operation on the asymptotic electric field $\mathbf{E}_{\omega,\mathbf{k}}$.

Given an expression for the first order particle distribution f_1, the associated plasma current $\mathbf{j}_{\omega,\mathbf{k}}$ and hence plasma susceptibility $\boldsymbol{\chi}$ may be calculated from:

$$\mathbf{j}_{\omega,\mathbf{k}} = q \int \mathbf{v} f_1(\mathbf{r}, \mathbf{p}, t) d^3\mathbf{p} = -i\omega \boldsymbol{\chi} \cdot \mathbf{E}_{\omega,\mathbf{k}}. \tag{3.33}$$

These expressions are additive between multiple species so we reintroduce a sum over particle species s:

$$\boldsymbol{\chi}(\omega, \mathbf{k}) = \sum_s \frac{\omega_{ps0}^2}{\omega \Omega_{cs0}} \sum_{n=-\infty}^{\infty} \int_{-\infty}^{\infty} \int_0^{\infty} \frac{2\pi \Omega_{cs} p_\perp dp_\perp dp_\parallel}{\omega - k_\parallel v_\parallel - n\Omega_{cs}} \mathbf{S}_n \tag{3.34}$$

Here we have defined the variables Ω_{cs0} and ω_{ps0} to represent the species-specific cyclotron and plasma frequencies using the species rest mass and number density. The matrix $\mathbf{S}_n$ is defined by:

$$\mathbf{S}_n = \begin{bmatrix} n^2 J_n^2 p_\perp U/z^2 & in J_n J_n' p_\perp U/z & n J_n^2 p_\perp U/z \\ -in J_n J_n' p_\perp U/z & (J_n')^2 p_\perp U & -i J_n J_n' p_\parallel U \\ n J_n^2 p_\perp U/z & i J_n J_n' p_\parallel U & J_n^2 p_\parallel W \end{bmatrix}, \tag{3.35}$$

The final steps required to calculate a dispersion relation involve a process identical to that applied to the cold plasma dispersion relation in Section 2.2.3. We note that the dielectric tensor,

$$\boldsymbol{\epsilon}(\omega, \mathbf{k}) = \mathbf{1} + \sum_s \boldsymbol{\chi}_s, \tag{3.36}$$

is defined as the addition of an identity matrix to the sum of the species-specific susceptibilities that we have calculated earlier. Given the dielectric tensor and using Equation 2.8, we may determine the linear dispersive properties of electromagnetic waves by solving the wave equation,

$$\frac{c^2}{\omega^2}\left(\mathbf{kk} - k^2\mathbf{1}\right) + \boldsymbol{\epsilon}(\omega, \mathbf{k}) = 0, \tag{3.37}$$

for the gyrotropic particle distribution functions that we are interested in.

Classically we would now input an analytic expression for the gyrotropic particle distribution functions f_s into Equation 3.37. In all but the simplest cases of f_s, no direct analytic expression may be found to solve this equality. This means that many guiding assumptions and approximations must be made in order to achieve analytical tractability. However these assumptions often limit the generality or accuracy of analytically derived expressions for the linear growth rates of kinetic instabilities. We instead opt to solve this equation numerically, and the next two sections follow through with the process of calculating dispersion solutions and growth rates numerically. Numerical codes are constructed for solving both the simple non-relativistic case and a more complex fully relativistic case in Section 3.3.

3.2 Non-Relativistic Kinetic Dispersion Solver

3.2.1 Objective

In order to accurately evaluate a general solution for the linear growth rate γ of waves with frequency ω and wavevector $\mathbf{k}$ in a magnetized homogeneous plasma with a gyrotropic description of the velocity component of phase space for many species $f_s(v_\parallel, v_\perp)$, we must solve the wave equation,

$$\mathbf{M} = \frac{c^2}{\omega^2}\left(\mathbf{kk} - k^2\mathbf{1}\right) + \mathbf{1} + \sum_s \frac{\omega_{ps0}^2}{\omega\Omega_{cs0}} \sum_{n=-\infty}^{\infty} \int_{-\infty}^{\infty} \int_0^{\infty} \frac{2\pi\Omega_{cs} p_\perp dp_\perp dp_\parallel}{\omega - k_\parallel v_\parallel - n\Omega_{cs}} \mathbf{S}_n = \mathbf{0}. \tag{3.38}$$

Here ω_{ps} denotes the species-specific plasma frequency, and Ω_{cs} denotes the species-specific cyclotron frequency using the relativistic particle mass. The subscript zero represents quantities that are calculated using the species rest mass m_{s0}.

As mentioned in the previous section, we choose not to consider an analytical representation of the underlying particle distribution functions. Instead we use a gridded representation of velocity space to describe the distribution of each particle species. This representation can be evaluated for any value of ω_r, ω_i and $\mathbf{k}$ provided that a suitable numerical integration scheme is applied.

Given a means to evaluate the integrals in the dielectric tensor $\boldsymbol{\epsilon}$, Equation 3.38 may be solved using iterative methods. We observe that the solubility condition of this equation is that $det|\mathbf{M}| = 0$. In numerical optimization, a cost function is a function which may be evaluated to give a single scalar output and is suitable for minimization. In numerical optimization a real valued cost function is maximized or minimized. We define the cost function as:

$$C(\omega_r, \omega_i, \mathbf{k}) = abs[det|\mathbf{M}(\omega_r, \omega_i, \mathbf{k})|]. \tag{3.39}$$

To reduce the number of free parameters, we fix $\mathbf{k}$ to a series of specific values prior to minimizing the cost function. This means that we are only minimizing a function with two arguments, ω_r and ω_i. Provided that a local minimum can be identified and that the cost function C is sufficiently smooth, the parameters corresponding to soluble values of $\mathbf{M}$ may be found. Methods for numerical minimization all work by evaluating the cost function for multiple different parameters. This means that we have to compute the integrals within the dielectric tensor $\boldsymbol{\epsilon}$ quickly to attain a solution in a reasonable amount of time. This provides the primary motivation for our first simplification.

In the fully non-relativistic regime where $\Gamma = 1$, $\Omega_{cs} = \Omega_{cs0}$ and $\mathbf{p} = m_0\mathbf{v}$ the integrals over perpendicular velocity may be performed separately with no dependence on ω or $k_\parallel$. This means that we can perform the perpendicular integral once, and cache the result for later evaluations with different values of ω and $k_\parallel$. This approximation effectively reduces the integral from two dimensional to one dimensional for the majority of iterations, granting a significant computational speed-up. In this section we will describe the implementation of these prescriptions.

3.2.2 Implementation

We are free to choose the perpendicular direction of the wavevector such that $\mathbf{k}c^2/\omega^2 = (n_x, 0, n_z)$ without loss of generality. The left-hand term of Equation 3.38 is then:

$$\frac{c^2}{\omega^2}\left(\mathbf{kk} - k^2\mathbf{1}\right) = \begin{bmatrix} -n_z^2 & 0 & n_x n_z \\ 0 & -n_x^2 - n_z^2 & 0 \\ n_x n_z & 0 & -n_x^2 \end{bmatrix}, \tag{3.40}$$

where we have used the notation n_x and n_z to represent wave normals. We also note that the susceptibility matrix $\boldsymbol{\chi}$ has several symmetric and anti-symmetric terms, $\boldsymbol{\chi}_{1,3} = \boldsymbol{\chi}_{3,1}$, $\boldsymbol{\chi}_{2,1} = -\boldsymbol{\chi}_{1,2}$ and $\boldsymbol{\chi}_{3,2} = -\boldsymbol{\chi}_{2,3}$. This further reduces the number of integrals we must perform. We define the following two-dimensional integrals which must be performed every time $k_\perp$ is altered. As these integrals must be performed over multidimensional data, they constitute the most expensive operation of the code:

$$q_1 = \int_0^\infty J_n^2 \frac{\partial f(v_\parallel, v_\perp)}{\partial v_\perp} dv_\perp, \tag{3.41}$$

$$q_2 = \int_0^\infty J_n^2 v_\perp \frac{\partial f(v_\parallel, v_\perp)}{\partial v_\parallel} dv_\perp, \tag{3.42}$$

$$q_3 = \int_0^\infty J_n J_n' v_\perp \frac{\partial f(v_\parallel, v_\perp)}{\partial v_\perp} dv_\perp, \tag{3.43}$$

$$q_4 = \int_0^\infty J_n J_n' v_\perp^2 \frac{\partial f(v_\parallel, v_\perp)}{\partial v_\parallel} dv_\perp, \tag{3.44}$$

$$q_5 = \int_0^\infty {J'}^2_n v_\perp^2 \frac{\partial f(v_\parallel, v_\perp)}{\partial v_\perp} dv_\perp, \tag{3.45}$$

$$q_6 = \int_0^\infty {J'}^2_n v_\perp^3 \frac{f(v_\parallel, v_\perp)}{\partial v_\parallel} dv_\perp. \tag{3.46}$$

In the fully non-relativistic limit, these integrals do not need to be performed every time ω or $k_\parallel$ are updated, as these depend only on $k_\perp$. To perform these integrals numerically we use a Simpson integrator[70]. This very simple method is effective when the function being integrated is well represented by a series of quadratic splines. The grid resolution in velocity space can be increased until the particle distributions are well represented by splines. We recall that the argument of the Bessel functions is $z = k_\perp v_\perp / \Omega_{cs}$, which is always small for waves whose perpendicular phase velocity lies within the region of interest. This means that the Bessel functions do not oscillate rapidly and can be well represented by splines. Even in the most extreme cases, involving heavy ion cyclotron harmonics at large values of $k_\perp$, the number of perpendicular cells may simply be extended until numerical convergence is attained.

To compute the susceptibilities we compute the following six integrals in the parallel direction:

$$\boldsymbol{\chi}_{11} = \frac{2\pi\omega_{ps}^2 n^2 \Omega_{cs}^2}{\omega^2 k_\perp^2} \int_\infty^\infty \frac{\omega q_1 - v_\parallel k_\parallel q_1 + k_\parallel q_2}{\omega - k_\parallel v_\parallel - n\Omega_{cs}} dv_\parallel, \tag{3.47}$$

$$\boldsymbol{\chi}_{12} = i\frac{2\pi\omega_{ps}^2 n \Omega_{cs}}{\omega^2 k_\perp} \int_\infty^\infty \frac{\omega q_3 - v_\parallel k_\parallel q_3 + k_\parallel q_4}{\omega - k_\parallel v_\parallel - n\Omega_{cs}} dv_\parallel, \tag{3.48}$$

$$\boldsymbol{\chi}_{13} = \frac{2\pi\omega_{ps}^2 n \Omega_{cs}}{\omega^2 k_\perp} \int_\infty^\infty \frac{\omega v_\parallel q_1 - v_\parallel^2 k_\parallel q_1 + k_\parallel v_\parallel q_2}{\omega - k_\parallel v_\parallel - n\Omega_{cs}} dv_\parallel, \tag{3.49}$$

$$\boldsymbol{\chi}_{22} = \frac{2\pi\omega_{ps}^2}{\omega^2} \int_\infty^\infty \frac{\omega q_5 - v_\parallel k_\parallel q_5 + k_\parallel q_6}{\omega - k_\parallel v_\parallel - n\Omega_{cs}} dv_\parallel \tag{3.50}$$

$$\boldsymbol{\chi}_{23} = -i\frac{2\pi\omega_{ps}^2}{\omega^2} \int_\infty^\infty \frac{\omega v_\parallel q_3 - v_\parallel^2 k_\parallel q_3 + k_\parallel v_\parallel q_4}{\omega - k_\parallel v_\parallel - n\Omega_{cs}} dv_\parallel, \tag{3.51}$$

$$\boldsymbol{\chi}_{33} = \frac{2\pi\omega_{ps}^2}{\omega^2} \int_\infty^\infty \frac{\omega v_\parallel q_2 - v_\parallel n\Omega_{cs} q_2 + n\Omega_{cs} v_\parallel^2 q_1}{\omega - k_\parallel v_\parallel - n\Omega_{cs}} dv_\parallel. \tag{3.52}$$

Every time ω or $k_\parallel$ is updated, these one-dimensional integrals must be evaluated. At the complex poles, the arguments of the six integrals listed above will not be smooth even when the underlying distribution functions are themselves smooth. We cannot approximate this behaviour directly in terms of a polynomial. Extra care must be taken to treat the poles correctly.

Classically we would split these integrals into a principal part and a complex residual. While the residual is easy to evaluate, unfortunately the calculation of the principal part requires just as much effort as performing the integral without separating the parts at all. We therefore opt to use a numerical approach where the integral is discretized into simpler parts and calculated analytically. We choose to reformulate the integrals using midpoint interpolation and evaluate each analytically as a series. Symbolic expressions for each of the integrals may then be computed numerically by summation. Each integral contains a term proportional to $\log(\omega - n\Omega_{cs} - k_\parallel v_{\parallel 0}) - \log(\omega - n\Omega_{cs} - k_\parallel v_{\parallel 1})$, where $v_{\parallel 0}$ and $v_{\parallel 1}$ are the limits of parallel integration for a particular grid cell. We refer to this term as the complex logarithm. Conveniently, it is impossible for branch cuts to occur under the current prescription, so that the complex logarithm is easy to evaluate.

We can introduce the correction prescribed by analytic continuation by simply multiplying the imaginary component of the complex logarithm by the sign of the imaginary component of the input frequency ω_i. The complex logarithm also poses the greatest risk for loss of numerical precision.

In our problem the complex logarithm takes an argument which may be represented as $1+x$, where x is complex. When x is very small, the value of $1+x$ is well approximated by unity, even though the result of the complex logarithm goes as x when Taylor expanded to first order. This means that a significant loss of numerical precision may occur. To get around this problem, a fourth order Taylor expansion is selectively applied only when $|x|$ is small. This conveniently cancels a large number of terms in the analytically calculated integral, resulting in greatly reduced loss of numerical precision. When $|x|$ is large, we evaluate the complex logarithm directly to attain an accurate computation. We can achieve the best of both approaches via this selection approach.

Given a way to evaluate the susceptibilities $\boldsymbol{\chi}$ and hence the determinant of matrix $\mathbf{M}$ for given values of $\mathbf{k}$, ω_r and ω_i, we may now numerically minimize the cost function. This works well as the cost function is smooth and continuous at all points. Local minima are first identified by performing a scan over the parameters ω_r, ω_i and $\mathbf{k}$. Where a local minimum exists in this scan, a root is assumed present. This root is then iteratively converged upon using a Nelder Mead gradient descent algorithm[71]. Once converged, the root is then plotted to show linear growth scaling against the chosen parameters.

This approach still requires a degree of insight by the user. The region of instability must be known prior to the performance of a parameter scan so that the necessary local minimums can be identified. This can be achieved by exploiting the large body of literature which catalogues the great majority of plasma instabilities. To benchmark this code, we compare it to some well known instabilities in the next section.

3.2.3 Benchmark Problems

For the code to be useful in general, it should work for a multitude of dispersion and linear growth calculations. We first test it against the previous derivations in this chapter, beginning with the two-stream instability. Finding a solution to Equation 3.7 demonstrates a technique which may be used to calculate linear growth rates within the hydrodynamic regime, when $v_{th} < |v_{\parallel} - \omega/k_{\parallel}|$. We computed growth rates for a system of two counter-streaming electron beams in Section 3.1.1.

Figures 3.4 and 3.5 are produced using the same bulk parameters of $n_e = 2.5 \times 10^{-19} m^{-3}$ and $B_0 < 10^{-6} T$ and with k oriented in the direction of the magnetic normal. While it may seem strange to specify a magnetic field at all in this calculation, which is for unmagnetized plasmas, the code was constructed to specifically analyse magnetized plasmas and cannot operate without a guide field. Fortunately we observe that at angles around $\theta \approx 0^o$, the prescription of a very small magnetic field has no effect on the result. As a delta function is unphysical and does not map directly to a continuous velocity distribution function, a small thermal spread is introduced for each beam such that $v_{th} = 0.01 v_0$. The drift velocity for each of the counter-streaming beams is set to be $v_0 = 10^5 ms^{-1}$. This places the beam velocities well below the relativistic regime where we may expect to see effects which are not purely electrostatic. For visualization purposes, and referring back to Equation 3.39, we also define the function:

$$z_1(\omega, \mathbf{k}) = \frac{1}{\sqrt{C(\omega, \mathbf{k})}} = \frac{1}{\sqrt{abs[det|\mathbf{M}(\omega, \mathbf{k})|]}}, \tag{3.53}$$

This function is plotted in Figure 3.4 and provides a means to easily identify roots in the complex frequency plane. In this figure we have fixed the value of k to be equal to $0.5\omega_{pe}/v_0$. When an exact solution is present, the value of z_1 approaches infinity. In practice, due to finite numerical precision, z_1 instead just becomes very large. A root is determined to exist only when $z_1(\omega, \mathbf{k}) > 10$. From viewing the complex plane shown in Figure 3.4 it is clear that the function z_1 is both smooth and continuous. Functions with these properties are typically easy to numerically

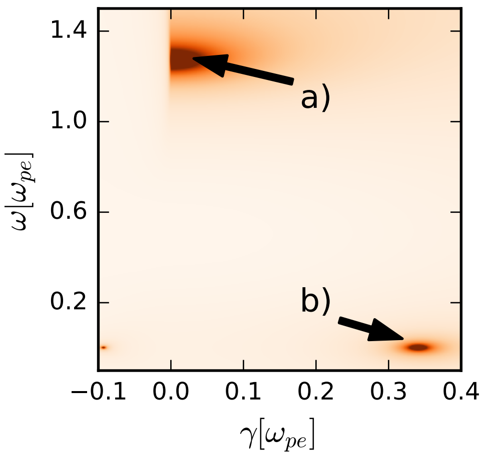

Figure 3.4: Equation 3.53 with argument $\mathbf{k} = (0.5\omega_{pe}/v_0, 0)$ is plotted for the same two-stream instability that we have described in the main body of text. Dark regions show where the solubility condition is close to being satisfied while lighter regions show where this condition is not met. A stationary solution at $\omega_r \approx 1.25\omega_{pe}$ is marked by annotation a) and a growing solution at $\omega_r = 0$ is shown by annotation b).

optimize providing that a local minimum may first be identified. Stationary solutions are marked by annotations a) and b). There is also a local minimum located at $\omega \approx 0$ and $\omega_i \approx -0.1\omega_{pe}$. This minimum is not an exact solution to the wave equation because $det|\mathbf{M}| \neq 0$ and $z_1 < 10$. This approach may be repeated for a large number of values of wavevectors. We may then plot these to show a dispersion relation in (ω, k), as in Figure 3.5.

In Figure 3.5 we fix the imaginary component of frequency so that we can evaluate function z_2 for every point in the region of $(\omega, \mathbf{k})$ space of interest. We have shaded the background of Figure 3.5 in red and blue to reflect the properties of the function:

$$z_2(\omega, \mathbf{k}) = Sign[Re[det|\mathbf{M}(\omega, \mathbf{k})|]] \times z_1(\omega, \mathbf{k}). \tag{3.54}$$

This method for visualization is useful when analysing more complex dispersion relations. Where dark red and dark blue regions meet, an exact solution exists. If the point of red and blue intersection is less dark, then only a local minimum may be present. The process of gradient descent and the marginalisation scan are highlighted by the functions shown in figures 3.4 and 3.5. The background shading shown here, which is intended to shed light on the numerics underlying dispersion relation plots, is removed from similar plots in later chapters where we focus more

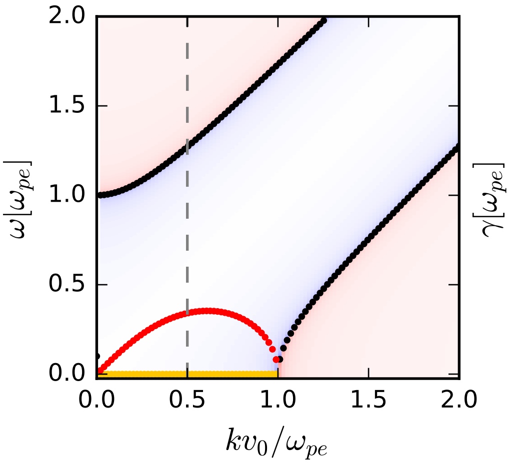

Figure 3.5: Numerical solution to Equation 3.38 for a system comprising of two counter-streaming plasmas, each with density $\frac{1}{2}n_0$ and velocity $\pm v_0$. Black lines show non growing roots while the yellow line at $\omega = 0$ shows the real component of frequency for growing roots. The corresponding positive linear growth rate for the yellow line is shown in red. The red and blue tinted background on this figure reflects the value of function 3.54 with imaginary argument $\omega_i = 0.0001\omega_{pe}$: regions in red designate positive z_2 and regions in blue designate negative z_2. The grey dashed line traces $k = 0.5\omega/v_{th}$, which we inspected in Figure 3.4.

on the questions of physics. Figures 3.4 and 3.5 thus depict the same phenomena but from different perspectives. The analytical solution to the equation which we have solved numerically was also shown in Figure 3.1. We have reproduced this figure using the new gyrotropic kinetic dispersion solver that we have constructed. This is shown in Figure 3.5. There is excellent agreement between figures 3.1 and 3.5.

The second derivation that we performed in Section 3.1.2 was that of Landau damping in the kinetic regime. As this derivation is itself an approximation, we cannot directly compare our results to the analytical expressions without first running kinetic simulations. Instead, let us address the general features of damping in a magnetized plasma, so as to show the effectiveness of the prescription for analytic continuation that we have previously identified. The problem that we select is to show the real and damped solutions for the dispersion relation of a warm magnetized plasma. We select bulk parameters of magnetic field $B = 2T$, electron number density $n_e = 10^{19}m^{-3}$ and electron temperature $T_e = 1$keV. For these parameters the ratio of plasma frequency to electron cyclotron frequency is $\omega_{pe}/\Omega_{ce} = 0.8$. The particle distribution function is discretized on a 1000×1000 velocity grid and only the electron cyclotron harmonics $n = -1$, $n = 0$ and $n = 1$ are considered. Here

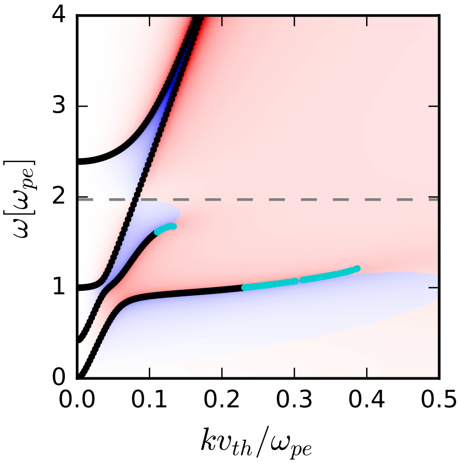

Figure 3.6: Warm plasma dispersion relation plotted from our solution of Equation 3.37 using a Maxwellian velocity distribution and bulk parameters $B = 2T$, $n_e = 10^{19}m^{-3}$, $T_e = 1$keV with propagation angle $\theta = 45^o$. From highest to lowest frequency, and following the formalism discussed in the introduction to this thesis, the black lines show accurate portrayal including thermal corrections of the extraordinary, ordinary, upper bulk and lower bulk modes. The cyan lines show solutions which are damped, while the dashed grey line shows the $n = 1$ electron cyclotron resonance.

the velocity distribution is set to be Maxwellian and isotropic, and the angle of wave propagation is set to be $\theta = 45^o$ from the magnetic normal. We present the dispersion relation computed for these parameters in Figure 3.6.

This figure closely resembles a cold plasma dispersion relation. The primary observable differences are due to effects caused by the non-zero thermal spread in the electron velocity distribution function. In particular the lower bulk mode as described in the cold plasma formalism in Section 2.2.3 increases with frequency as k is increased. The values of ω_r in cyan have imaginary components of frequency which are negative. It is important to note that without the prescription of analytic continuation, the result of the resonant integral is not determined by the sign of the imaginary component of frequency. This means that in order to calculate damped modes it is necessary to apply analytic continuation. The choice to simply reverse the sign of the imaginary part of the complex logarithm is appropriate as it creates no discontinuities as ω_i is varied from positive to negative values. At very high values of k, damped solutions still exist with $\gamma < 0.2\omega_{pe}$, although they are not seen in this figure. Unfortunately we are unable to easily identify the location of local minimum due to a constrained range of imaginary samples. This in practice is not a huge problem as these waves are so strongly damped that they very quickly self dissipate.

While solutions found using the Friede Conte plasma dispersion function, which is specific to Maxwellian plasmas, have been available for considerable time[72], the capability to compute exact solutions for arbitrary gyrotropic distribution functions on a single desktop computer is very recent. A code which is claimed to solve kinetic dispersion relations for magnetized plasmas was recently released by Xie et al.[73], however this code is limited to describing the plasma by a series of drifting Maxwellians. Astfalk and Jenko have recently constructed a similar code which describes plasmas with a arbitrary gyrotropic distribution functions. This code was used to investigate the parallel ion firehose instability[74]. The code presented in this publication works in a very similar way to the code that we have now outlined. The primary difference is that the authors use a numerical technique involving hyper-geometric series to exactly evaluate the integrals of Bessel functions of the fist kind. While there may be a subset of problems where it is necessary to use this approach, we found that for the problems of our own interest, the Bessel functions only varied very gradually with perpendicular velocity. Our approach involves simply interpolating the Bessel functions evaluated on the grid. We are able to check that this approach is correct by testing convergence. We check that varying the number of perpendicular grid cells does not change the result. Astfalk and Jenko suggest that they may be the first to construct a gyrotropic kinetic dispersion solver of this class[74].

Prior to the work by Astfalk and Jenko, we have found a case where Hellinger et al. used a similar, but less sophisticated code to investigate the oblique kinetic electron firehose instability[75]. This work shows that the kinetic approach to solving the dispersion relation for a gyrotropic plasma gives solutions which differ to the previous analytical approach of solving linear growth rates classically for that problem. The work by Hellinger et al. is very useful to us. We can directly compare our solution to theirs and determine whether or not agreement exists. As many PIC simulations were performed and benchmarked against in the work by Helling et al., we can be confident that their solution is correct.

The oblique and parallel electron firehose instabilities[76] are mechanisms where the free energy associated with a parallel temperature anisotropy drives the instability of non-propagating waves with $\omega_r \approx 0$. To recreate the first figure in Hellinger et al.[75], which is shown here in Figure 3.7, we used the following temperatures: parallel temperature of $T_{\|} = 1$keV and perpendicular temperature of $T_{\perp} = 216$eV. This gave a temperature anisotropy of $T_{\|}/T_{\perp} = 0.216$. Velocities were sampled on a 1000×1000 grid and only the electron cyclotron harmonics

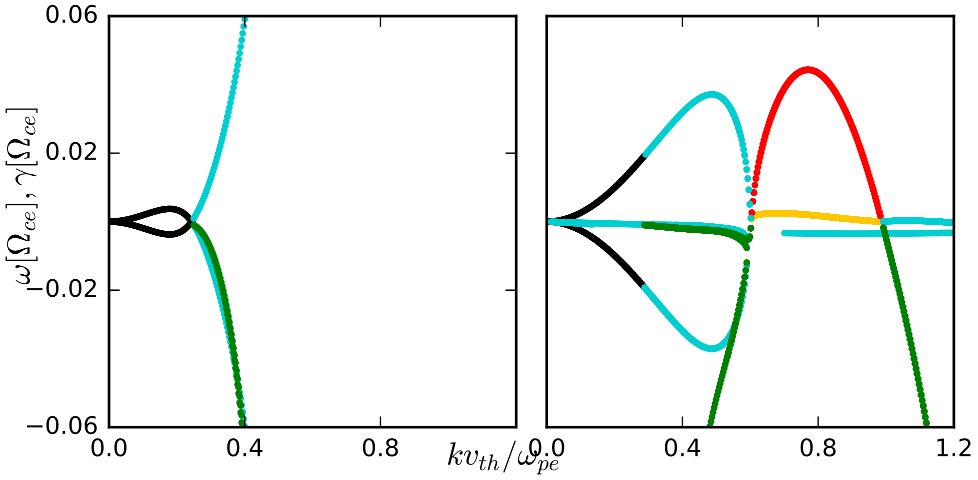

Figure 3.7: Dispersion relations and linear growth rates of the kinetic electron firehose instability calculated at $\theta = 0^o$ and $\theta = 64^o$ from the magnetic normal. A temperature anisotropy of $T_\parallel/T_\perp = 0.216$ and a parallel electron plasma beta of $\beta_{e\parallel} = 2$ is used. The colour scheme used here is consistent with Figures 3.1, 3.3, 3.5 and 3.6, where negative growth rates are now shown in green.

$n = -1$, $n = 0$ and $n = 1$ were considered. The background magnetic field was set to $B = 0.0707T$ and the background density was set to $n_e = 2.5 \times 10^{19} m^{-3}$, giving a ratio of plasma to electron cyclotron frequency of $\omega_{pe}/\Omega_{ce} = 22.7$. For these parameters, the plasma frequency is significantly lower than the electron cyclotron frequency. This means that the firehose instability sets in at a much lower temperature anisotropy threshold than would be possible at the higher magnetic fields we address in later chapters.

When both the dispersion relation and linear growth rates are calculated for the oblique firehose instability we arrive at a figure which is nearly identical to that presented in the Hellinger et al. We see no observable differences in the plot produced at $\theta = 0^o$, while in the right panel at $\theta = 64^o$ a slight difference exists in the damped solution. While the damping rate in our solution appears smooth and continuous, a kink exists in the rightmost damped solution of the Hellinger et al.[75]. As the difference arises only in damped solutions, our current working hypothesis is that it is related to differences in the precise prescriptions for analytic continuation which are used. We cannot currently be sure which code is correct although the deviation only occurs for strongly damped modes. So far we have only investigated problems involving a single electron species. We will now move on to a problem where energetic ions play a key role.

Ion cyclotron emission is caused by a collective instability involving wave-particle resonance between a population inversion in the perpendicular velocity distribution of energetic ions and magneto-acoustic waves travelling perpendicular to the magnetic field. This problem has been extensively studied and both PIC and hybrid simulations (with kinetic ions and fluid electrons) have been performed to study the linear and nonlinear stages[77–79]. Much of the original analytical work was performed by Dendy et al.[80, 81], where the relevant linear theory was outlined for several cases.

One particular scenario, which has been extensively studied, involves a thermal background population of 1keV deuterons and a much more energetic ring beam of 3.5MeV fusion born alpha particles. We demonstrate that not only can we reproduce the linear instability results attained from kinetic simulation using our dispersion solver but also we can predict the excitation and non-excitation of specific cyclotron harmonics.

In Figure 3.2.3 we attempt to reproduce growth rates derived from simulations of ion cyclotron emission performed by Cook et al.[77]. The initial suprathermal particle velocities in this work were sampled from a distribution with a fixed perpendicular velocity forming a ring beam distribution. As we cannot use delta functions in this code, we instead add a slight thermal spread to the perpendicular and parallel velocities of the ring beams examined in this simulation. The distribution function $f_\alpha(v_\parallel, v_\perp) = \exp[-(v_\parallel^2 + (v_\perp - v_B)^2)m_\alpha/2k_bT_\alpha]$ is therefore used to describe the alpha-particle ring beam. The electron and deuteron populations are taken to be Maxwellian with temperatures $T_\alpha = T_e = T_d = 1$keV. The ring beam velocity is described by $v_B^2 = 2E_B/m_\alpha$ where $E_B = 3.5$MeV is the source energy for fusion born alpha particles. A fixed background magnetic field of $B = 2.1T$ and an electron number density of $10^{19}m^{-3}$ is used. The minority alpha particle fraction is set to $\xi = 10^{-3}$ and the deuteron number density is chosen so that charge neutrality is satisfied. In accordance with the work by Cook et al. we consider waves travelling at an angle of $\theta = 89.5^o$ from the magnetic field direction.

Our results show agreement with the PIC simulations in the work by Cook et al.[77]. The Alfven wave is well reproduced and appears non-dispersive up to around $kv_A/\Omega_{c\alpha} = 12$. We see that strong linear growth occurs for alpha-particle cyclotron harmonics between $n = 6$ and $n = 12$. We also see that, of the modes with alpha cyclotron resonance number $n < 16$, the strongest growth occurs for the 12th harmonic. All of this is in strong agreement with the simulations presented in Cook et al.

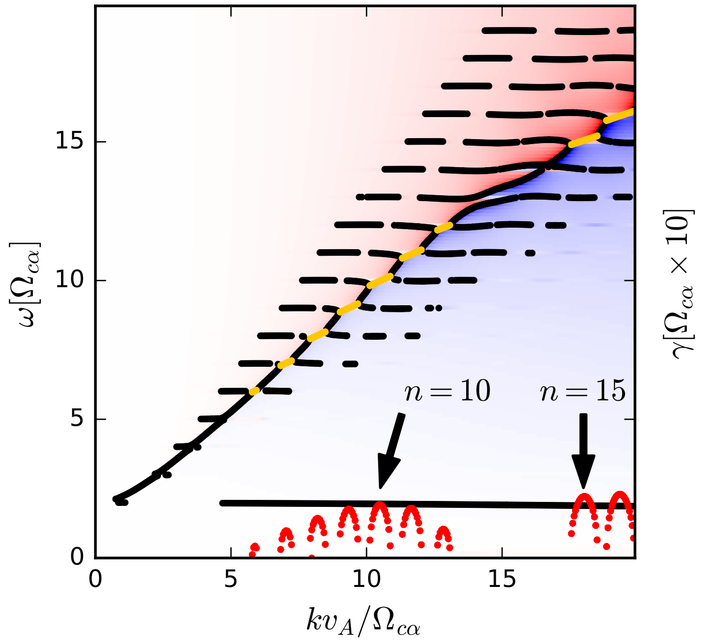

Figure 3.8: Linear growth rates calculated from Equation 3.38 for a ring beam containing 3.5MeV alpha-particles and a background plasma comprising 1keV deuterons and electrons. The background magnetic field strength is $B = 2.1T$ and electron density $n_e = 10^{19}m^{-3}$. The ring beam fraction is $\xi = 10^{-3}$ and propagation angle is $\theta = 89.5^o$. Growth rates are shown in red, and are multiplied by a factor of 10 for ease of display. Stationary solutions are shown in black, while the real parts of growing solutions are shown in yellow.

Our treatment makes no approximations beyond the linearization procedure. This means that we can also make well informed predictions about the behaviour of linear physics for the parameters investigated. We see that, while the $n = 13$ and $n = 14$ modes are non-growing, the $n = 15$ and $n = 16$ modes have large linear growth rates. This gap is not expected by the analytical treatment performed by Dendy et al.[80], although our predictions do appear to agree with the results from kinetic simulation in Cook et al.[77]. Now that we have demonstrated that the non-relativistic solver produces accurate results, we will move on to discussing its numerical efficiency and performance.

3.2.4 Numerical Performance

For any numerical code to be useful, it must run within an acceptable time frame. We aimed for this code to be able to produce useful output in under five minutes on a standard desktop computer. Prototyping was initially performed in the programming language Python using the collection of open source numerical libraries aggregated in the SciPy collection[82]. While these numerical libraries helped to minimize the effort required for both prototyping and implementation, it soon become apparent that calculating solutions using this approach was too demanding on computational resources. The bottleneck was identified to be the computation of the integrals in the parallel direction. As we had based the code on libraries within the SciPy ecosystem, we chose only to rewrite the portion of the code which calculated the result of the integrals in Equation 3.38.

For easy interoperability between Python and native code we chose to write this function in C++ using the boost-python library to support interfacing between languages. Using a programming language with an optimizing compiler allows us to format the integrals in such a way as to minimize the number of numerical operations which must be performed. We found that the most expensive operation in the parallel integral was the complex logarithm. The number of calls to this function were therefore minimized by the selection of appropriate temporary variables. Care was taken to align memory correctly, as well as to avoid any further unnecessary computations. These efforts improved the performance of the code by around a factor of 100 on a single process.

As the problem is "embarrassingly parallel" we are able to solve for multiple values of k concurrently with no inter-process communications. This means that we can trivially fully utilize all cores of a desktop workstation. The resulting improved performance allows the user to modify input parameters and plot dispersion relations tens of times at reasonable resolution within a single hour. One avenue for optimization that we did not employ was root following. Once the existence of a root is known, it is possible follow this root as wavevector is varied. Calculation of linear physics with this computationally aided analytical approach allows for a much more guided approach than does directly running PIC simulations due to the reduced iteration time. We can predict the linear behaviour of a PIC simulation, which may take several hours to run on hundreds of cores, in several minutes.

3.2.5 Conclusions

In this section we have discussed the mathematical and numerical methodology required to calculate the real and imaginary parts of linear dispersion relations for multi-species gyrotropic magnetized plasmas which are spatially homogeneous. We have constructed a code which can compute these results within a few minutes, providing that the underlying particle distribution functions may be represented on a regular grid in parallel and perpendicular velocity space. We have performed numerous benchmark tests on this code which show that this code accurately calculates growth rates for plasmas of the type described. These benchmarks included the two-stream instability, Landau damping in a magnetized plasma, the oblique kinetic firehose instability for anisotropic electrons, ion cyclotron emission driven by population inversion in the perpendicular direction. The latter two of these benchmarks show remarkable agreement with the cited literature and we expect that similarly accurate results are attainable from applying this code to other problems.

As linear results may be attained quickly through application of this code, we suggest that it may be helpful to precede every particle-in-cell simulation of linearly unstable homogeneous gyrotropic plasmas with a calculation of this kind. A mechanism to calculate reliable growth rates which may be readily computed is a very useful resource. This code is fully open sourced and may be freely downloaded[83].

In our analysis we found that, for certain instabilities, a non-relativistic treatment did not produce the correct results. It therefore seems useful to modify our dispersion solver such that a fully relativistic description may be captured. As far as we know this task has not until now been completed. We therefore have sufficient motivation to construct a fully relativistic adaptation for this code. The implementation, testing and numerical performance of this modification will be discussed in the following section.

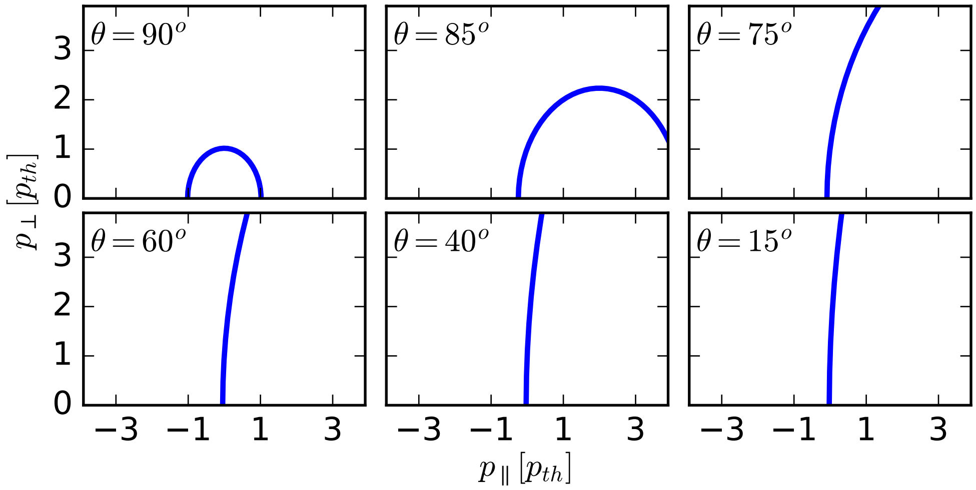

Figure 3.9: The resonance condition prescribed by $\Gamma\omega - k_\parallel p_\parallel/m_s - n\Omega_{cs0} = 0$ is plotted in momentum space for various values of the angle θ between the magnetic normal and wavevector. All figures are plotted where the electron temperature $T_e = 1keV$, frequency terms are described by $(\omega - n\Omega_{ce})/\Omega_{ce} = 10^{-3}$ and the parallel wavevector is set to $k_\parallel = \cos\theta\Omega_{ce}/c$.

3.3 Relativistic Kinetic Dispersion Solver

3.3.1 Objective

In the previous section we discussed solving the linear kinetic dispersion relation for a gyrotropic plasma in the non-relativistic regime. While most of the problems that we may encounter in the context of MCF are only slightly relativistic, we will demonstrate that the presence of a fully or partially relativistic treatment is still important. We note that each element of the susceptibility tensor for a specific species $\boldsymbol{\chi}_s$ is characterized by the infinite sum of terms divided by a denominator of the form $\omega - k_\parallel p_\parallel/m_s\Gamma - n\Omega_{cs0}/\Gamma$, where $\Gamma(p_\parallel, p_\perp) = \sqrt{1 + p_\perp^2/m_s^2c^2 + p_\parallel^2/m_s^2c^2}$ is the relativistic Lorentz factor for a particle with momentum $\mathbf{p}$ and rest mass m_s. When the wavenumber and frequency are selected such that the denominator approaches zero, the integral would be singular without the prescription of a complex frequency. We describe this condition by stating that a particle with momentum $\mathbf{p}$ is resonant with waves with parallel wavenumber $k_\parallel$ and complex frequency ω.

The resonance condition for a range of angles from the magnetic normal is shown in Figure 3.9. It can be seen that as the angle from magnetic normal θ is increased the resonant curve is progressively transformed from a circle at $\theta = 0^o$

toward an almost straight line at $\theta = 15^o$. The non-relativistic resonance condition is simply a straight line, which corresponds closely to the panel set at $\theta = 15^o$. This means that the presence of a small relativistic correction has a relatively small effect for small values of θ and a non-negligible effect for wave propagation angles close to $\theta = 90^o$. This means that in order to capture certain kinetic effects, particularly when $\theta \approx 90^o$, we must construct a code which describes a relativistic resonance condition.

3.3.2 Implementation

While in the previous section we were able to separate the parallel and perpendicular integrals efficiently, the existence of a relativistic correction now means that the parallel and perpendicular integrals are inseparable. This creates a large performance problem. Repeatedly computing integrals on a higher dimensional grid is prohibitively expensive. To begin with however, we will assume that this problem does not exist and instead focus on a direct means to evaluate the necessary integrals ignoring the computational constraints. We will only later discuss the optimization techniques that are employed.

We discretize the particle distributions on a two dimensional regular grid. Derivatives are then evaluated on a staggered grid. One of the simplest methods to perform a two dimensional integral would be to use a Simpson integrator as was done for the non-relativistic code. This time around however, we cannot guarantee that the integrand is well approximated by quadratic splines. Instead, we choose to reformulate the integrand into two interpolated quantities, namely the numerator and denominator. As the numerator does not describe the singularity it can be accurately represented by quadratic splines which we may describe by some polynomial $P(p_{\|}, p_{\perp})$.

Since the denominator is much smoother than the numerator, the choice of representation for the denominator was primarily influenced by what kind of integrals were the easiest to perform analytically. The double integral

$$\int\int \frac{P(p_{\|}, p_{\perp})}{m_{\|}p_{\|} + m_{\perp}p_{\perp} + c_d} dp_{\|} dp_{\perp} \tag{3.55}$$

is the simplest way to integrate denominator gradients in both the parallel and perpendicular directions and is relatively easy to evaluate. In this notation c_d is some complex constant defined by the denominator, $m_{\|}$ and $m_{\perp}$ are the gradients of the denominator and $P(p_{\|}, p_{\perp})$ denotes a bivariate polynomial containing powers of $p_{\|}$ and $p_{\perp}$ which interpolates the numerator. While this integral can be tackled

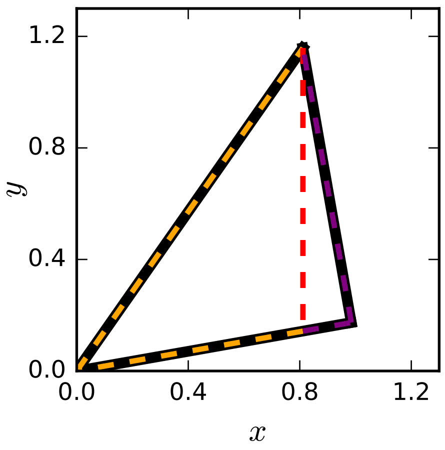

Figure 3.10: Sample rotated right angle triangle in its new basis. We see that this may be split into two separate triangle primitives which may be integrated through parametrization of the limits $x_i(y) = m_i y$ and coordinate translations.

directly, it is simplest to first rotate into a basis where the singularity only exists in one direction. The integral may then be evaluated through consideration of the complex logarithm. Unfortunately it is not possible to construct a surface which intersects each vertex of a rectangle using just three free parameters. Using this scheme to interpolate on a rectangular grid would result in the surface defined by the denominator having discontinuities where neighbouring cells meet. This means that it would be possible to select a value of ω where the singularity would not be captured by any of the neighbouring cells. Not only would this result in a solution which was noisy, it would be possible to lose the majority of the complex component of a solution.

To avoid this issue, we instead split each rectangle of the grid into two right angled triangles. A flat surface may intersect each vertex of a triangle. These right angled triangles form the primitives which we use to calculate all integrals in this section. When considering parametrizing the boundaries for integration over a triangle, it is necessary that at least one edge of the triangle be aligned with one of the basis vectors of integration. Once a right angled triangle has been rotated, this condition is no longer satisfied. For any arbitrarily rotated triangle there exists a decomposition into two sub triangles which satisfy this condition. This is shown visually in Figure 3.10, where the red dashed line is aligned with the y direction.

This leaves us with a total of four triangles to integrate over for each rectangular grid cell. Thankfully the denominator is identical for every component of the per species susceptibility tensor $\boldsymbol{\chi}$. This means that as long as the spline coefficients are only ever evaluated at the end of an integral evaluation, the numerically demanding component of the integrals must only be performed once for each triangle. Now that we have outlined the integration scheme we may move on to a description of which values we choose to store in memory.

We will discuss these variables in order of lifetime. As the susceptibility parameters are typically modified in the order of $k_\perp$, $k_\parallel$ and finally ω we can afford to keep variables which do not depend on ω longer than variables which do. It is also possible to select several variables which have no dependence on $k_\perp$. To compute the six non symmetric elements of plasma susceptibility we must store a minimum of three separate quantities in two dimensions. We also choose to absorb all dependencies on parallel momentum which raises the number of stored variables to six. The same is not possible for perpendicular momentum as the Bessel functions are dependent on both $k_\perp$ as well as the resonance number dependent quantities. Storing quantities which depend on resonance numbers in two dimensions would consume a prohibitive amount of memory. The choice of values stored in two dimensions is thus defined as follows:

$$U_1 = \frac{\partial f_s}{\partial p_\perp}\Gamma^{-1}, \tag{3.56}$$

$$U_2 = p_\parallel \frac{\partial f_s}{\partial p_\perp}\Gamma^{-1}, \tag{3.57}$$

$$U_3 = \left(p_\perp \frac{\partial f_s}{\partial p_\parallel} - p_\parallel \frac{\partial f_s}{\partial p_\perp}\right)\frac{\Gamma^{-2}}{m_s}, \tag{3.58}$$

$$U_4 = p_\parallel \left(p_\perp \frac{\partial f_s}{\partial p_\parallel} - p_\parallel \frac{\partial f_s}{\partial p_\perp}\right)\frac{\Gamma^{-2}}{m_s}, \tag{3.59}$$

$$W_1 = p_\parallel p_\perp \frac{\partial f_s}{\partial p_\parallel}\Gamma^{-1}, \tag{3.60}$$

$$W_2 = p_\parallel \left(p_\parallel \frac{\partial f_s}{\partial p_\perp} - p_\perp \frac{\partial f_s}{\partial p_\parallel}\right)\Gamma^{-2}, \tag{3.61}$$

where p denotes momentum in the parallel or perpendicular direction, f_s is the species distribution function and Γ is the Lorentz factor. All of these terms must be computed only once, when the solver is first initialized. We can also cache several more terms in one dimension which do not depend on ω. Many of the terms involve Bessel functions and multiples of perpendicular velocity. These terms only need to be updated when the value of $k_\perp$ is modified which does not happen for every integral evaluation. Conveniently, the Lorentz factor in the cyclotron frequency and perpendicular velocity cancel in the Bessel functions when converting from velocity to momentum coordinates. This gives an argument of $z = k_\perp p_\perp / m_s \Omega_{cs0}$ for the Bessel functions J_n and their derivatives J_n' with respect to the argument. The following one dimensional terms are then stored for every harmonic number and in the perpendicular direction each time $k_\perp$ is updated.

$$q_{1,n} = \frac{n^2 J_n^2 \Omega_{cs0}^2 m_s^2}{k_\perp^2}, \tag{3.62}$$

$$q_{2,n} = \frac{n J_n J_n' p_\perp \Omega_{cs0} m_s}{k_\perp}, \tag{3.63}$$

$$q_{3,n} = \frac{n J_n J_n \Omega_{cs0} m_s}{k_\perp}, \tag{3.64}$$

$$q_{4,n} = J_n'^2 p_\perp^2, \tag{3.65}$$

$$q_{5,n} = J_n J_n' p_\perp, \tag{3.66}$$

$$q_{6,n} = J_n^2, \tag{3.67}$$

where m_s is the species rest mass and Ω_{cs0} is the species cyclotron frequency calculated using the rest mass. Given these temporary variables the arguments for the splines in the numerator may be calculated efficiently. As these expressions each involve factors of ω they may be evaluated only when the integrals are performed. The integrals which must be performed to calculate the susceptibilities for each species are then defined as follows,

$$\chi_{11} = \frac{2\pi\omega_{p0}^2}{\omega} \sum_n \sum_{i,j} \mathbf{G} \cdot \left[\mathbf{P}(U_1 q_{1,n}) + \frac{1}{\omega}\mathbf{P}(U_3 q_{1,n}) \right] 4\Delta p_\parallel 4\Delta p_\perp, \tag{3.68}$$

$$\chi_{12} = -i\frac{2\pi\omega_{p0}^2}{\omega} \sum_n \sum_{i,j} \mathbf{G} \cdot \left[\mathbf{P}(U_1 q_{2,n}) + \frac{1}{\omega}\mathbf{P}(U_3 q_{2,n}) \right] 4\Delta p_\parallel \Delta p_\perp, \tag{3.69}$$

$$\chi_{13} = \frac{2\pi\omega_{p0}^2}{\omega} \sum_n \sum_{i,j} \mathbf{G} \cdot \left[\mathbf{P}(U_2 q_{3,n}) + \frac{1}{\omega}\mathbf{P}(U_4 q_{3,n}) \right] 4\Delta p_\parallel \Delta p_\perp, \tag{3.70}$$

$$\chi_{22} = \frac{2\pi\omega_{p0}^2}{\omega} \sum_n \sum_{i,j} \mathbf{G} \cdot \left[\mathbf{P}(U_1 q_{4,n}) + \frac{1}{\omega} \mathbf{P}(U_3 q_{4,n}) \right] 4\Delta p_{\|} \Delta p_{\perp}, \tag{3.71}$$

$$\chi_{23} = -i\frac{2\pi\omega_{p0}^2}{\omega} \sum_n \sum_{i,j} \mathbf{G} \cdot \left[\mathbf{P}(U_2 q_{5,n}) + \frac{1}{\omega} \mathbf{P}(U_4 q_{5,n}) \right] 4\Delta p_{\|} \Delta p_{\perp}, \tag{3.72}$$

$$\chi_{33} = \frac{2\pi\omega_{p0}^2}{\omega} \sum_n \sum_{i,j} \mathbf{G} \cdot \left[\mathbf{P}(W_1 q_{6,n}) + \frac{1}{\omega} \mathbf{P}(W_2 q_{6,n}) \right] 4\Delta p_{\|} \Delta p_{\perp}, \tag{3.73}$$

where the function **P** is defined to convert the gridded argument into a vector of nine coefficients describing the bivariate quadratic interpolation of the function argument at position i, j on the grid. The function **G** describes the result attained from analytically computing the integrals over rotated triangles for each of the nine quadratic interpolation coefficients. The trailing factor of 4 arises from the fact that in order to perform quadratic interpolation in two dimensions 4 cells must be interpolated across. The functions **G** and **P** are too lengthy to define here, and are defined in appendix A.1. Much of the code in these two functions was generated directly from the symbolic algebra package Mathematica[84]. Using automated code generation to both solve systems of equations as well as perform the integrals analytically, we were able to save effort and avoid many potential human errors. Special care was taken in setting up the triangles to avoid loss of numerical precision. This goal was attained giving results which agreed up to at-least four significant figures with Monte-Carlo integration over thousands of sample surfaces including complex poles and a multitude of rotations. Before discussing the primary optimizations that were performed on this code we will quickly discuss some of the benchmark calculations that were performed. For all non-relativistic problems that we attempted to analyse results were equivalent to the non-relativistic solver. We will therefore focus on examining problems with properties that depend on the relativistic correction.

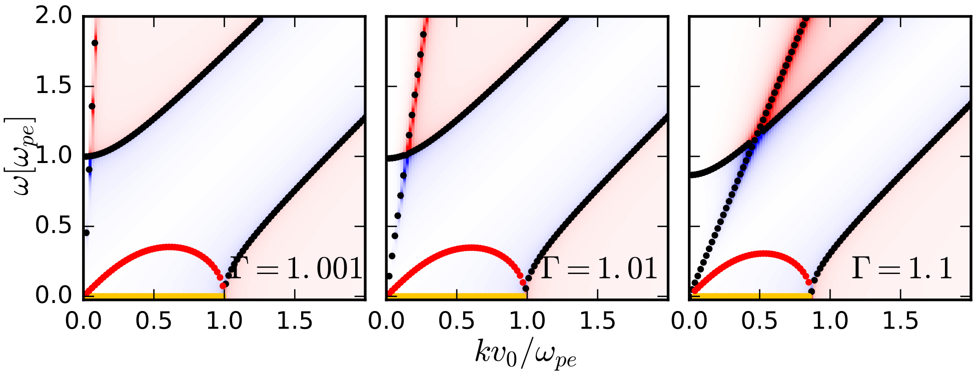

Figure 3.11: The relativistic two-stream instability is solved for the three cases of Lorentz factor $\Gamma = 1.001$, $\Gamma = 1.01$ and $\Gamma = 1.1$. Shading is performed using the same techniques as is applied in previous figures of this type. As the Lorentz factor is increased the cut-off frequency is lowered by an amount proportional to Γ as we would expect.

3.3.3 Benchmark Problems

The first problem we investigate using a fully relativistic description is again the two-stream instability. We return to this problem due to its simplicity and the fact that it has already been documented in this chapter. Initially, we verify that the relativistic version of this code produces the same output as the non-relativistic version. We then chose to progressively increase the relativistic Lorentz factor Γ until a deviation occurred. In Figure 3.3.3 we present the dispersion relations for two-stream instabilities which have been computed at Lorentz factors of $\Gamma = 1.001$, $\Gamma = 1.01$ and $\Gamma = 1.1$.

This figure was produced using bulk parameters of $n_e = 2.5 \times 10^{19} m^{-3}$ and beam velocities of $v_0^2 = c^2(1 - \Gamma^{-2})$. The static dispersion of the 'O' mode appears to change due to the scaling of the k axis on v_0. We see that both the frequency and linear growth rates are reduced by similar amounts. This is ultimately uninteresting as the growth and frequencies are only modified by an amount similar to the Lorentz factor. In MCF plasmas we do not typically reach highly relativistic temperatures, so the omission of a small correction would be acceptable. We discussed earlier that for angles close to $\theta = 90^o$ the relativistic correction could have a much larger impact. One instability where this is the case is that of the electron cyclotron maser instability.

The electron cyclotron maser instability (ECMI) is characterized by coherent emission at the electron cyclotron harmonics and in the direction perpendicular to

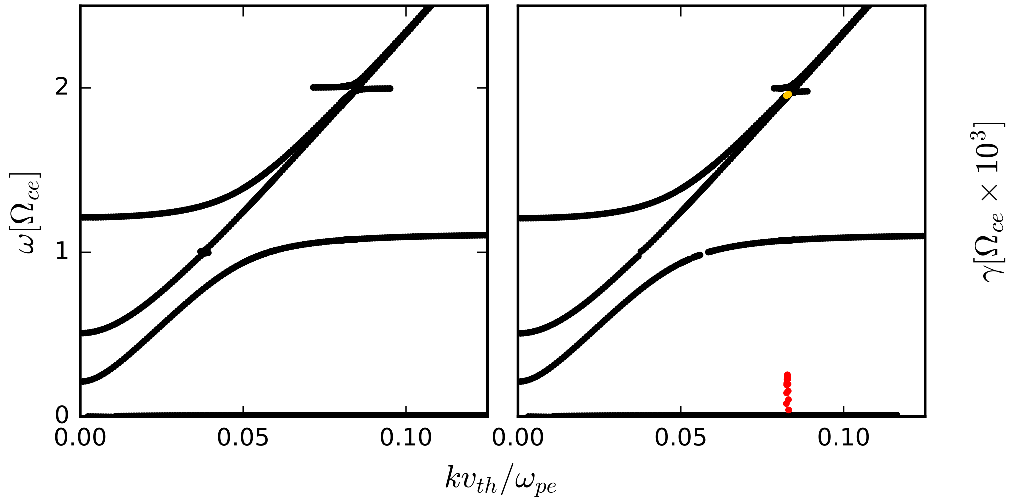

Figure 3.12: Comparison between electron cyclotron maser instability calculated using the non-relativistic and fully relativistic approaches on the left and right panels respectively. For these parameters only the relativistic solver appears to produce results which are linearly unstable. This plot was calculated for a system comprising of background electrons and an energetic ion ring beam. Growth was calculated at angle $\theta = 89^o$ from the magnetic normal.

the magnetic normal. The ECMI was first investigated by Harris et al. for a ring beam distribution and using a non-relativistic resonance condition[85]. Similar work was later performed by Melrose investigating the same instability but driven by a drifting bi-Maxwellian electron distribution[86, 87].

Wu and Lee pointed out that when the the resonance condition is described by a relativistic Lorentz factor, the resonance condition has a qualitatively different solution than when the condition $\Gamma = 1$ is prescribed[88]. This derivation was fleshed out further in 1982 by Melrose et al. and applied to explain millisecond bursts of auroral kilometric radio emission driven by loss cone distributions[89]. Satellite measurements have shown that electron horseshoe distributions exist which are unstable to the ECMI[90]. It has also been shown that the ECMI plays an important role in generating coherent emission during astrophysical shocks[91]. As the literature cited in this paragraph suggests that the growth rates of the ECMI are strongly dependent on a relativistic correction, we decided to demonstrate the differences between the non-relativistic and relativistic regimes using this code.

In Figure 3.12 we attempt to calculate growth rates for the ECMI driven by a superposition of an electron ring beam and electron background. The parameters used to construct this figure are defined as follows. The background electrons were described by a temperature of $T_e = 1keV$, density of $n_e = 10^{19}$ and the background magnetic field was set $B = 2T$. The ring beam was given a perpendicular drift velocity of $v_b = 5v_{th}$ and a beam fraction of $\xi = 0.01$. The thermal spread of the ring beam was set to be the same as that of the background electron temperature.

The panel on the left-hand side shows growth rates which were calculated using the non-relativistic approximation, while the figure on the right shows those computed using a fully relativistic description. We can see that instability is only predicted using the relativistic treatment. Growth rates are largest at the $n = 2$ electron cyclotron harmonic. This, in addition to the cited literature, means that for certain problems it is necessary to solve dispersion relations using a code which is fully relativistic. Having the option to use both a non-relativistic implementation as well as a relativistic implementation allows the user to pick and choose the appropriate description for every problem. While the numerical performance of the relativistic version of this code was always going to be lower than the non-relativistic one, we took several steps to improve matters. These are discussed in the following section.

3.3.4 Numerical Performance

In the form that we have outlined so far, the solution of a simple dispersion relation may take several hours or even days to compute for higher resolution problems. This is measured after applying the optimization techniques outlined in section 3.3.2. This level of performance was deemed to be unacceptable. To improve this, we determined an optimization strategy that would greatly reduce the frequency at which the full integral must be updated. We aimed to expand the integral into polynomials of $\omega = \omega_0 + \delta\omega$. We observe that the a sum of several polynomials may be computed before the polynomial is evaluated. We describe the denominator by $\omega - n\Omega_{cs} - k_{||}v_{||}$. As $v_{||}$ and Ω_{cs} vary across the grid in $p_{||}$ and $p_{\perp}$, different regions must be expanded around different values so that $\delta\omega$ may be kept small. We sort grid cells into lists containing similar values of $n\Omega_{cs} + k_{||}v_{||}$. Typically, 1000 or so of such lists may be collected. For each cell in this list, a polynomial in $\delta\omega$ is computed from its Taylor series. We then compute the sum of each of the coefficients for these polynomials. The coefficients of the summed expansions are stored up to fourth order. The summed polynomials may then be repeatedly evaluated later using different values of ω.

Through this approach we can significantly reduce the time taken to evaluate the integral. Finally, we observe that this approach breaks down close to the singularities. For everywhere except the region around the complex poles, an expansion may be chosen which gives a result which has an error comparable to floating point precision. The accuracy of this expansion was tested by directly comparing to the numerically evaluated result attained by the previous technique of integrating triangles. When the small expansion condition $\delta\omega/(\omega_0 - n\Omega_{cs} - k_\parallel v_\parallel)$ is not true, we instead fall back to the more computationally expensive original method involving evaluating the analytical solution to the integral of triangle primitives. In the examples which we tested against, the application of this series expansion typically removed the need to evaluate the full primitive integrals for somewhere in the region of $90 - 99\%$ of cases. We found that worse performance was observed for more relativistic problems. Even after these improvements, the integration time was still dominated by the integration of triangle primitives, although the overall performance was reduced by a factor similar to the reduction in number of triangle primitive integrals which were performed. This code ultimately calculated roots significantly slower than the non-relativistic solver due to its increased complexity required by a fully relativistic treatment. Most problems may be investigated on the order of tens of minutes using this approach.

3.3.5 Conclusions

At the time of writing, as far as we know, we have constructed the first fully relativistic kinetic dispersion solver capable of operating on dielectric tensors characterized by fully relativistic gyrotropic plasmas[1]. This approach appears to make predictions which deviate significantly from the non-relativistic approximation, even when the underlying particle distributions are only weakly relativistic. These deviations are in agreement with the literature and may be readily demonstrated when applied to the electron cyclotron maser instability for a perpendicular momentum distribution function characterized by an energetic electron ring beam and thermal background.

---

[1] Shortly following the writing of this chapter, Verscharen et al. published a paper outlining a similar code[92]. Work on this code likely began before we had initiated work. It is possible that performance advantages exist within our version of the code, however this remains untested.

Chapter 4

Anomalous Doppler Instability

4.1 Introduction

The anomalous Doppler instability or "fan instability" is a key relaxation mechanism for suprathermal electrons in MCF plasmas. The anomalous Doppler effect was first investigated by Ginzburg[93]. This was followed by Kadomtsev and Pogutse[94], who theorized that it could play an important role in the isotropization of accelerated electrons and thus in creating an observable anomalous resistance in tokamak plasmas. This work was shortly followed by Sharpiro and Shevchenko[95], who showed that the quasilinear evolution of a bump on tail distribution under excitation at the Cerenkov ($\omega = k_{\|}v_{\|}$) wave-particle resonance would lead towards the formation of a plateau distribution. They also showed that there was a possibility for this plateau to be unstable to waves at the resonant electron cyclotron frequency driven by the anomalous Doppler instability (ADI). Wave-particle resonance occurs at the n'th cyclotron harmonic when the condition:

$$v_{\|} = \frac{\omega - n\Omega_{cs}}{k_{\|}} \tag{4.1}$$

is satisfied. The ADI occurs when waves at the lower bulk branch are resonant with the $n = -1$ electron cyclotron harmonic. In this context, the term "anomalous" arises in contrast to the "normal Doppler" $n = 1$ resonance. When the condition $\omega_{pe} \ll \Omega_{ce}$ is met, waves at the lower bulk branch may be described by $\omega_L \approx \cos\theta\omega_{pe}$, where θ is the angle between the wavevector $\mathbf{k}$ and the magnetic field $\mathbf{B}$, ω_{pe} is the plasma frequency and Ω_{ce} is the electron cyclotron frequency. Importantly, the ADI is able to excite waves when the parallel derivative of the electron velocity distribution function is zero. This means that the ADI is able to operate on flat tails. For waves to be excited by the ADI, it is necessary that Landau damping is small. This means that the distribution function must be close to flat for $F(\omega/k_{\|})$, where $\omega/k_{\|}$ defines the velocity at the Cerenkov resonance. As the ADI is able to operate on extended flat tails, it is thought that it plays a key role in determining the dynamics of runaway electrons during tokamak disruptions[96]. The ADI may also play an important role in governing the dynamics of runaway electrons during argon puffing[97].

Nezlin showed that for certain systems containing plasma beams, it was possible for waves to exist with "negative energy"[98]. This means that the energy of the medium is less when the wave is present than when the wave is absent. Nezlin also showed that in order for the wave to grow, there must be a mechanism in place for it to dissipate energy back to the medium. Nezlen then linked this physics to the anomalous Doppler effect, where the particle distribution may be modified by waves at the anomalous Doppler resonance. It has also been suggested that the ADI may produce a positive slope in the parallel electron distribution function. The formation of a positive slope in the parallel electron distribution was first suggested by Molvig et al.[99], and this suggestion was shortly repeated by Parail and Pogutse[100]. The formation of a positive slope is one of the key physical predictions which we attempt to verify in this chapter.

The ADI has also been suggested as an important driver in several aspects of tokamak physics. Relativistic electrons have been suggested to be resonant with lower hybrid waves in tokamak plasmas[101, 102]. This has relevance in understanding the evolution of the runaway current in tokamaks. This effect has been suggested to show that confinement improvements may be possible[103]. Recently, observations in ELMs have suggested that energetic electrons may be present. It has been hypothesised that these electrons may be exciting waves through the anomalous Doppler resonance[23]. Links have also been suggested to exist between the ADI and electron cyclotron emission observed during ramp down[104].

Physics of the anomalous Doppler resonance is also thought to play a role in space plasmas and the production of auroral kilometric radiation. It has been shown that the anomalous Doppler instability can excite very low frequency (whistlers and lower hybrid) waves in the solar wind[105]. The anomalous Doppler resonance has additionally been considered as a method for exciting lower-hybrid waves in auroral plasmas[106]. This work suggests that for certain parameters, the growth rate of lower hybrid waves which are resonant with electrons in the tail exceeds the growth rate for waves on the lower bulk branch. The anomalous Doppler resonance has also been linked to stellar disks and the Lindbald resonance[107].

In this chapter we begin by examining several approaches to calculating the linear behaviour of the ADI. These linear calculations are followed up by comparison to fully kinetic 2D3V PIC simulations spanning the linear phase of instability, quasi-linear evolution of the underlying velocity distributions and finally the non-linear phase of the instability where coherent wave coupling plays a role.

4.2 Linear Theory of the ADI

Before attempting to simulate the ADI, it is important to develop a good understanding of the relevant linear theory. Here we will review several of the approaches that have previously been employed to describe the linear physics of the ADI. The central theme of each approach is to solve the wave equation for a description of the dielectric tensor which is relevant to runaway electrons. It is usual to apply the approximation that waves are purely electrostatic. This means that only the longitudinal component of the wave equation needs to be solved. Here we will discuss two separate approaches which were employed by Dendy et al. to describe the ADI in different regimes. We then benchmark these analytical solutions for the linear growth rates against solutions which we have computed exactly using the dispersion solver which we constructed in Chapter 3. We show which approximations are valid to our problem parameters and compare these results against derivations which have been performed elsewhere.

4.2.1 Wave-Wave Resonance Linear Theory of the ADI

We first outline a variant of the ADI known as the “wave-wave” resonance ADI. This description of instability at the anomalous Doppler electron cyclotron resonance was outlined by Dendy and Lashmore-Davies in 1984[108]. The derivation starts by considering an electron velocity distribution function characterized by the superposition of a Maxwellian background population of electrons at rest and a Maxwellian beam of electrons drifting in the magnetic field direction with velocity v_0:

$$f_e(v_\parallel, v_\perp) = \frac{1}{1+\xi}\left[\frac{1}{(2\pi)^{3/2} v_{T0}^3} e^{-(v_\parallel^2+v_\perp^2)/2v_{T0}^2} + \frac{\xi}{(2\pi)^{3/2} v_{B\parallel} v_{B\perp}^2} e^{-(v_\parallel - v_0)^2/2v_{B\parallel}^2} e^{-v_\perp^2/2v_{B\perp}^2}\right]. \tag{4.2}$$

The thermal background is isotropic with temperature T_0 and thermal velocity $v_{T0} = \sqrt{k_b T_0/m_e}$. The beam fraction is defined by $\xi/(1+\xi)$ where $\xi \ll 1$. The beam is allowed to be anisotropic, with separate thermal velocities in the parallel and perpendicular directions defined by $v_{B\parallel}$ and $v_{B\perp}$.

The assumption is made that the instability is purely electrostatic. It is then possible to solve the dispersion relation by considering only the longitudinal component of the dielectric tensor. The longitudinal component of the dielectric tensor is calculated by computing $\epsilon_L = \mathbf{k} \cdot (\boldsymbol{\epsilon} \cdot \mathbf{k})/k^2$ and may be defined as follows[109]:

$$\epsilon_L = 1 - \sum_s \frac{\omega_{ps}^2}{k^2} \sum_{n=-\infty}^{\infty} \int_{-\infty}^{\infty} \int_0^{\infty} \frac{2\pi v_\perp dv_\perp dv_\parallel}{k_\parallel v_\parallel + n\Omega_{cs} - \omega} \left(k_\parallel \frac{\partial f_s}{\partial v_\parallel} + \frac{n\Omega_{cs}}{v_\perp} \frac{\partial f_s}{\partial v_\perp} \right) J_n^2 \left(\frac{k_\perp v_\perp}{\Omega_{cs}} \right), \tag{4.3}$$

where ω_{ps} and Ω_{cs} are the species specific plasma and cyclotron frequencies and J_n is a Bessel function of the first kind. The first step is to expand the longitudinal component of the dielectric tensor to leading order in thermal terms. This expansion is easiest to understand with foreknowledge of the solution for both the upper and lower bulk branches. In the limit of $\omega_{pe} \ll \Omega_{ce}$, the upper and lower branches are described by the expressions $\omega_U^2 = \omega_{pe}^2 \sin^2\theta + \Omega_{ce}^2$ and $\omega_L = \omega_{pe}\cos\theta$. The evaluation and expansion of Equation 4.3 then gives the following expression:

$$\epsilon_r = 1 - \frac{\omega_{p0}^2 \cos^2\theta}{\omega^2} - \frac{\omega_{p0}^2 \sin^2\theta}{\omega^2 - \Omega_{ce}^2} - \frac{\omega_{pB}^2 \cos^2\theta}{(\omega - k_\parallel v_0)^2} - \frac{\omega_{pB}^2 \sin^2\theta}{(\omega - k_\parallel v_0)^2 - \Omega_{ce}^2}, \tag{4.4}$$

where ω_{p0} denotes the background plasma frequency, ω_{pB} the beam plasma frequency Ω_{ce} the electron cyclotron frequency and θ the orientation of $\mathbf{k}$ with respect to the magnetic field $\mathbf{B}$. The cold plasma dispersion relation $\epsilon_r = 0$ then defines four families of electrostatic waves. From left to right in Equation 4.4 these are the lower and upper bulk supported branches, together with two pairs of streaming branches that exist only in the presence of a beam. The terms describing the upper branch are then removed, leaving only the terms describing the lower bulk plasma branch and the two streaming branches. The substitution $\omega_L = \omega_{p0}\cos\theta$ highlights the longitudinal bulk plasma terms, so that:

$$\epsilon_r = \frac{\omega^2 - \omega_L^2}{\omega^2} - \frac{\omega_{PB}^2 \cos^2\theta}{(\omega - k_\parallel v_0)^2} - \frac{\omega_{PB}^2 \sin^2\theta}{(\omega - k_\parallel v_0)^2 - \Omega_{ce}^2}. \tag{4.5}$$

Here we diverge from the original work, which provides analytical approximations for the growth rates and density scaling: we directly solve these equations numerically. The standard approach for solving high order polynomials numerically is to compute the eigenvalues of the Frobenius companion matrix[110]. To apply this method to solve equations 4.4 or 4.5 we first represent them as polynomials of variable ω, then evaluate all other variables with exact numerical values. The roots of this polynomial

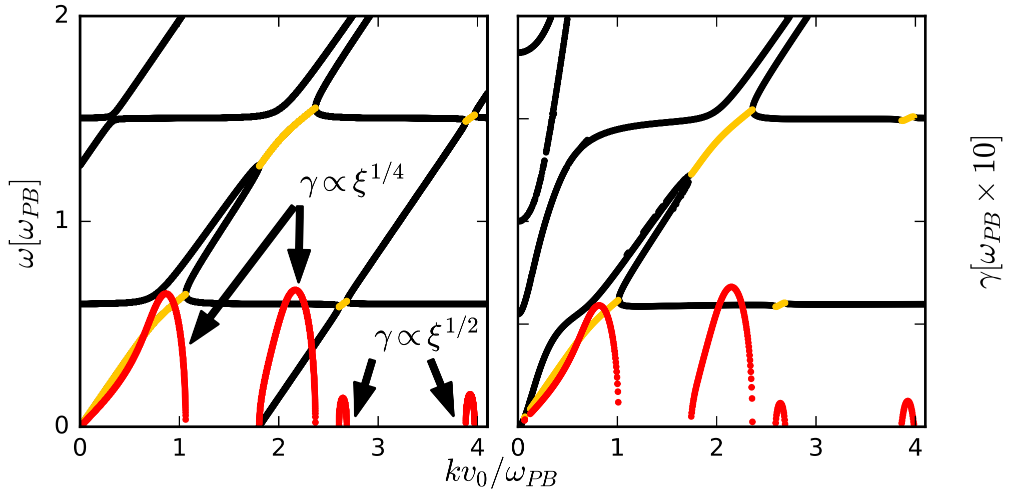

Figure 4.1: Real and imaginary parts of the dispersion relation for the wave-wave resonant ADI. (Left) Solutions of Equation 4.4. (Right) Solutions computed using the distribution function 4.2 and the gyrotropic dispersion solver outlined in Chapter 3. The real component of a stable mode is shown in black and the real component of a growing mode is shown in yellow. Growth rates shown in red are exaggerated by a factor of 10. For parameters, see main text.

may then be computed.

In Figure 4.1 we compare (left) solutions calculated by applying this technique to Equation 4.4 to (right) solutions calculated using the dispersion solver which we outlined in Chapter 3 for the distribution function 4.2. Both panels are calculated using the same parameters: $\theta = 45^o$, $\xi = 0.005$, $B = 2T$, $n_e = 2.5 \times 10^{19} m^{-3}$, $T_e = 1eV$, $v_{T0} = v_{B\|} = v_{B\perp} = v_{th} = \sqrt{k_b T_e / m_e}$ and $v_0 = 200 v_{th}$.

The Cerenkov branch occurs at the $n = 0$ wave-particle resonance of the beam and is described approximately by $\omega = k_\| v_0$. The two fastest growing modes occur when the Cerenkov branch is in resonance with the upper and lower bulk branches. This occurs when the line of Cerenkov resonance defined by $\omega \simeq k_\| v_0$ intersects with the upper and lower bulk branches at $\omega_U = \sqrt{\omega_{pe}^2 \sin^2\theta + \Omega_{ce}^2}$ and $\omega_L = \omega_{pB} \cos\theta$. If we inspect the Cerenkov resonance in more detail it is apparent that the resonant frequency may be modified by the presence of the beam when the beam fraction is sufficiently great. The modified resonance assumes the form $\omega = k_\| v_0 \pm \omega_{pB}$. These are the fast and slow modes supported by the beam. If the beam fraction is low enough this modification will not be well resolved and the resonance will revert to the condition $\omega = k_\| v_0$.

By comparing solutions obtained using different values of the beam fraction parameter ξ we infer that these growth rates scale as $\gamma \propto \xi^{\frac{1}{4}}$ when the fast and slow modes are resolved. We can determine whether the fast and slow modes are resolved through visual inspection of the dispersion solution. Two separated black lines exist above each of the purple Cerenkov unstable solutions in the regions $(0.6 < \omega/\omega_{PB} < 1.6, 1 < kv_0/\omega_{PB} < 1.6)$ and $(1.4 < \omega/\omega_{PB}, 2 < kv_0/\omega_{PB})$ respectively. These are the fast and slow modes. When the beam density is reduced below $\xi \simeq 1/225$ these lines begin to merge, with full merging having occured at $\xi < 1/300$, so that the fast and slow modes are not resolved. In this regime we find that growth rates scale as $\gamma \propto \xi^{\frac{1}{3}}$. Dendy and Lashmore-Davies made the prediction that this transition should occur at around $\xi \approx 1/256$[108]. Both the growth rate scaling and point of scaling transition which we have measured show very strong agreement with the predictions made by equations 14 and 18 of Dendy and Lashmore-Davies.

Two unstable regions are also present at the wave-wave ADI resonance. These two instabilities have much lower growth rates, which scale with density as $\xi^{\frac{1}{2}}$. This density scaling also agrees with equation 7 of Dendy and Lashmore-Davies[108]. The fact that we observe instability here and that the scaling agrees with predictions, validates both the present and the previous work and shows that the wave-wave resonant ADI has properties which differ from the wave-particle resonant ADI, which is discussed in Section 4.2.2.

Several differences also exist between the left and right panels of Figure 4.1. The dispersion solutions differ for small values of k, due to the added description of electromagnetic effects in the right-hand panel. Here, the electromagnetic O (ordinary) and X (extraordinary) modes dominate. The O and X modes both asymptotically tend toward $\omega = kc$ at higher values of k, so they may be neglected in the region of interest. The other key difference which exists is that much of the stable part of the wave-wave ADI resonance is missing on the right panel. On the left panel a black line is present which may be described by the equation $\omega = k_{\parallel}v_0 - \Omega_{ce}$. This line is missing from the right panel, because a small thermal spread in the beam distribution damps this mode. This damping is also manifest by a very slight reduction in the growth rates of the two wave-wave ADI instabilities shown in red on the right panel when compared to those in the left.

The observation of this effect introduces the question of what happens when we increase the thermal spread of the beam further. We address this question in Figure 4.3. To properly consider a non-zero thermal spread, we must use a kinetic description of the underlying velocity distribution functions. This means that we must use the latter of the two methods presented in Figure 4.3. In Figure 4.3 we vary

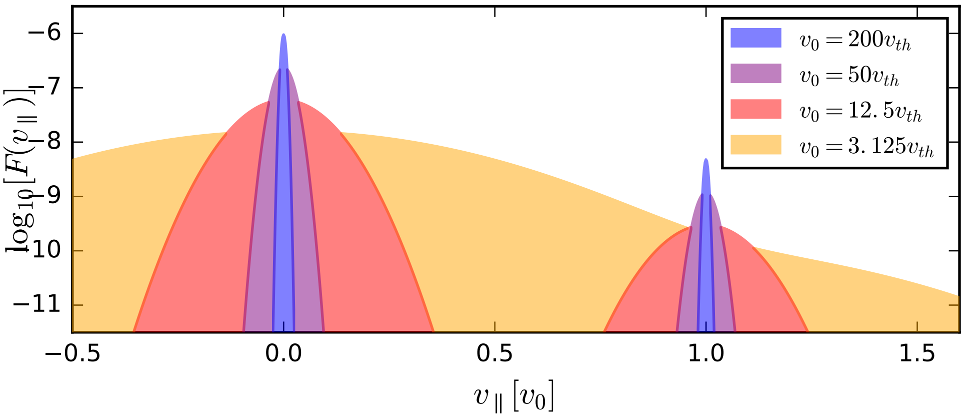

Figure 4.2: Parallel velocity distributions corresponding to those used in Figure 4.3. The ratio of beam velocity to thermal velocity is varied from $v_0/v_{th} = 200$ to $v_0/v_{th} = 3.125$ through the intermediate values of $v_0/v_{th} = 50$ and $v_0/v_{th} = 12.5$.

the thermal velocity while keeping the beam velocity v_0 constant. This is preferable to changing the beam velocity and keeping the thermal velocity fixed as the ratio v_0/c remains unaltered, and the electromagnetic effects are therefore held constant between panels. The ratios $v_0/v_{th} = 200$, 50, 12.5 and 3.125 are compared. The parallel velocity distributions constructed for the parameters which we examine in Figure 4.3 are shown in Figure 4.2. The remaining parameters remain identical to those examined in Figure 4.1. Raising the thermal velocity from $v_0 = 200v_{th}$ to $v_0 = 50v_{th}$ has very little effect on either of the two Cerenkov resonant instabilities at $k < \omega_{pB}/v_0$ and $k \simeq 2\omega_{pB}/v_0$. For these parameters modes remain within a hydrodynamic regime of instability where thermal terms may be neglected. The anomalous Doppler resonant modes at $k \simeq 2.5\omega_{pB}/v_0$ and $k \simeq 4\omega_{pB}/v_0$ are however greatly reduced by this small increase in thermal velocity. For this panel they are situated in a transient regime, where the wave-wave resonant effects are still present but are much reduced by kinetic damping. Increasing the thermal velocity to $v_{th} = v_0/12.5$ completely eliminates the presence of instability at the wave-wave anomalous Doppler resonance. We see that in the third panel the upper of the two Cerenkov resonances is also eliminated. Finally, in the case where $v_0 = 3.125v_{th}$, all of the previous instabilities are removed. This is to be expected as the underlying velocity distribution now very closely resembles a Maxwellian, with only a small change in slope at the beam velocity. While this behaviour has not yet been investigated in the context of the wave-wave resonant ADI, the transition from a hydrodynamic to kinetic regime has previously been investigated for the two-stream instability on several accounts[111–113].

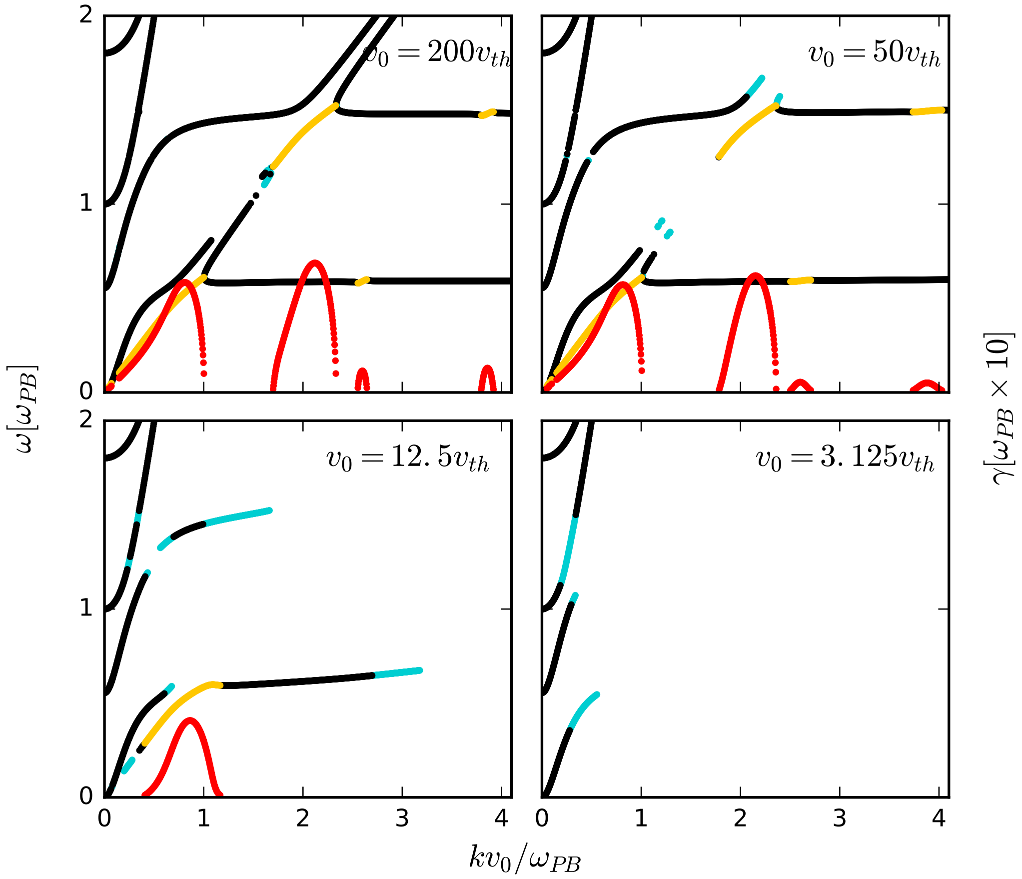

Figure 4.3: The wave-wave ADI is examined for various values of the beam velocity v_0. Equation 3.38 is solved using the distribution function 4.2 where the ratio of beam velocity to thermal velocity is varied from $v_0/v_{th} = 200$ to $v_0/v_{th} = 3.125$. The colour scheme matches figure 4.1, where cyan now depicts the real part of damped modes.

The original motivation for examining wave-wave instability at the anomalous Doppler resonance was that a bump on tail distribution could in principle be unstable to this instability. We find however that in order for this to be the case the bump would have to be very large when compared to the flat tail. We find that the wave-wave ADI is only linearly unstable for systems that are within the hydrodynamic regime where the beam and background are separated by large velocities. This configuration is also highly unstable to the wave-wave resonant Cerenkov instability. It was shown by Sharpiro and Shevchenko that a distribution with a beam would be flattened by Cerenkov emission originating from the positive slope in the distribution[95]. Due to the large growth rates of the wave-wave Cerenkov resonant instability for this configuration, we would expect that these flattening effects will tend to occur on very short time-scales. We therefore cannot perform first principles simulations for these parameters which last long enough for effects of the wave-wave resonant ADI to be detected. Instead, we may perform simulations which are initialized with an extended flat tail. To investigate distributions with a velocity plateau in the parallel direction we must use a description which is applicable to the kinetic regime. Several descriptions of the ADI which are relevant in the kinetic regime also exist. In the next section we will outline a treatment presented by Dendy and Lashmore-Davies[114].

4.2.2 Wave-Particle Resonance Theory of the ADI

Before we outline a wave-particle resonance treatment for the ADI, we first discuss our choice of analytical representation for the electron velocity distribution function. This will define the initial state for the particle-in-cell simulations presented in this chapter. We set the background magnetic field to $B = 2T$ and the initially spatially uniform electron number density to $n_e = 2.5 \times 10^{19} m^{-3}$. These parameter values are generically representative of the MCF plasma conditions found in tokamaks and stellarators. This gives a ratio of electron plasma frequency to electron cyclotron frequency of $\omega_{pe}/\Omega_{ce} = 0.8$. The electron wave-particle cyclotron resonance at the n'th harmonic occurs when the condition $\omega = k_{\|} v_{\|} + n\Omega_{ce}$ is satisfied for a wave with given $(\omega, k_{\|})$. The anomalous Doppler instability occurs when particles are resonant with waves at the $n = -1$ electron cyclotron resonance. For overall growth, instability at the wave-particle anomalous Doppler resonance must exceed damping caused by particles which are Cerenkov resonant at the $n = 0$ resonance. Landau damping occurs when the slope of the electron distribution function is negative. In this derivation we assume that negligibly few electrons satisfy the normal Doppler ($n = 1$) resonance or any of the higher resonances.

If we consider a distribution which is flat at the $n = 0$ resonance and non-zero at the $n = -1$ resonance for a wave with a given $(\omega, k_\parallel)$, we expect the system to be unstable to the ADI. A distribution consisting of a thermal Maxwellian background and an extended flat tail can satisfy this criterion, provided ω and $k_\parallel$ have values such that: the Cerenkov velocity $\omega/k_\parallel$ significantly exceeds (by a factor $\simeq 4$) the bulk thermal velocity, so that $\partial f/\partial v_\parallel\big|_{v_\parallel \approx \omega/k_\parallel}$ is very small; and the anomalous Doppler velocity $v_{AD} = (\omega + \Omega_{ce})/k_\parallel$ does not exceed the maximum velocity of the electrons in the tail. This form of distribution may be represented analytically as follows:

$$f_e(v_\parallel, v_\perp) = \begin{cases} (1-\xi)\exp[-v_\parallel^2/2v_{th}^2]\exp[-v_\perp^2/2v_{th}^2]/(8\pi^3 v_{th}^6)^{1/2}, & \text{if } \; v_0 > v_\parallel, \\ \xi\exp[-v_\perp^2/2v_{th}^2]/(2\pi v_{th}^2 v_1), & \text{if } \; v_1 > v_\parallel > v_0, \\ \xi\exp[-(v_\parallel - v_1)^2/2v_{th}^2]\exp[-v_\perp^2/2v_{th}^2]/(2\pi v_{th}^2 v_1), & \text{if } \; v_\parallel > v_1. \end{cases} \tag{4.6}$$

Here the electron thermal velocity is $v_{th} = (k_b T_e/m_e)^{1/2}$, ξ is the tail fraction, and $v_0 = v_{th}\log\left[v_1^2(1-\xi)^2/(2\pi\xi^2 v_{th}^2)\right]^{1/2}$ is the velocity at which the thermal bulk transitions to the plateau. The tail extends up to, and slightly beyond, v_1 which is the plateau maximum velocity; we have chosen to smooth the end of the electron tail so that no discontinuity exists within the distribution. This distribution is normalized so that $2\pi\int_{-\infty}^{\infty}\int_0^{\infty} v_\perp f_e(v_\parallel, v_\perp)dv_\perp dv_\parallel = 1$. The notation $F_e(v_\parallel) = 2\pi\int_0^\infty v_\perp f(v_\parallel, v_\perp)dv_\perp$ is used to indicate the perpendicular integrated distribution function. We note that the first derivative in $v_\parallel$ is discontinuous, but this is unimportant because no second derivatives are needed in this derivation. We use $T_e = 100eV$ for the electron thermal temperature, which is characteristic of the outer region of a tokamak plasma; $v_1 = 18.5v_{th}$ for the maximum tail velocity, corresponding to electron kinetic energy of 17.1kev and $\xi = 0.04$ for the tail fraction, which is exaggerated to accelerate the growth of instability. The parallel component of the electron distribution for these parameters is plotted in Figure 4.4.

Following the construction of this distribution function, we now compute linear growth rates. We base this derivation on work performed by Dendy and Lashmore-Davies[114]. Their paper outlines a means to calculate growth rates analytically by solving the longitudinal component of the dielectric tensor for a magnetized homogeneous plasma. Separate probability distribution functions are used for both ions and electrons. Here we revisit the longitudinal component of the dielectric

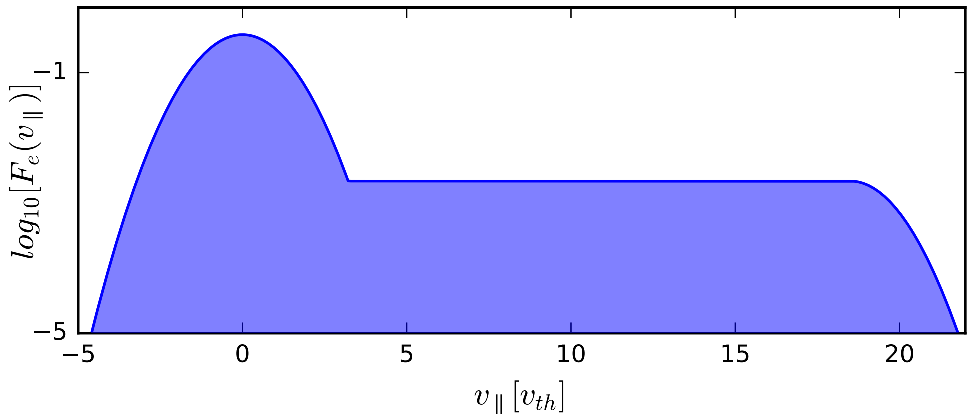

Figure 4.4: Analytical model for the parallel component of the electron velocity distribution function defined by Equation 4.6, for the parameters stated in the main text. The vertical axis is plotted on a logarithmic scale and is normalized so that $\int_{-\infty}^{\infty} F_e(v_\parallel) dv_\parallel = 1$.

tensor which may be defined as follows:

$$\epsilon_L = 1 - \sum_s \frac{\omega_{ps}^2}{k^2} \sum_{n=-\infty}^{\infty} \int_{-\infty}^{\infty} \int_0^{\infty} \frac{2\pi v_\perp dv_\perp dv_\parallel}{k_\parallel v_\parallel + n\Omega_{cs} - \omega} \left(k_\parallel \frac{\partial f_s}{\partial v_\parallel} + \frac{n\Omega_{cs}}{v_\perp} \frac{\partial f_s}{\partial v_\perp} \right) J_n^2 \left(\frac{k_\perp v_\perp}{\Omega_{cs}} \right). \tag{4.3 revisited}$$

Here ω_{ps} and Ω_{cs} are the species-specific plasma and cyclotron frequencies, and J_n is a Bessel function of the first kind. The solubility condition requires that $\epsilon_L = 0$ for a stable or growing purely longitudinal mode to exist. If the perpendicular distribution functions are Gaussian, we can integrate analytically over the Bessel functions of the first kind using their known indefinite integrals. Writing $f_s(v_\parallel, v_\perp) = F_s(v_\parallel) exp(-v_\perp^2/2v_{th}^2)/2\pi v_{th}^2$ such that $\int_{-\infty}^{\infty} F_s(v_\parallel) dv_\parallel = 1$, we may then integrate out the perpendicular dependence of the integral. Following the notation of ref [114], we define the expressions $v_B^2 = 2v_{th}^2$, $\beta_B = k_\perp^2 v_B^2 / 2\Omega_{ce}^2$ and $\Lambda_n(\beta) = \exp(-\beta) I_n(\beta)$, where $I_n(x)$ is a modified Bessel function of the first kind. The perpendicular integrated longitudinal dielectric tensor element then reduces as follows:

$$\epsilon_L = 1 - \sum_s \frac{\omega_{ps}^2}{k^2} \sum_{n=-\infty}^{\infty} \int_{-\infty}^{\infty} \frac{dv_\parallel}{k_\parallel v_\parallel + n\Omega_{cs} - \omega} \left(k_\parallel \frac{\partial F_s}{\partial v_\parallel} - \frac{2n\Omega_{cs}}{v_B^2} F_s(v_\parallel) \right) \Lambda_n (\beta_B). \tag{4.7}$$

Let us now consider the complex component of each cyclotron resonance in Equation 4.7 independently. As the complex component is small, the individual perturbations from each resonance may be treated separately and their solutions only later combined. First, let us consider the $n = 0$ Landau resonance for electrons only. In this case, the integral reduces to a single term depending on the slope of the parallel distribution function:

$$\epsilon_L = 1 - \frac{\omega_{pe}^2 k_\parallel \Lambda_0(\beta_B)}{k^2} \left[P \int_{-\infty}^{\infty} \frac{dv_\parallel}{k_\parallel v_\parallel - \omega} \frac{\partial F_e}{\partial v_\parallel} - \frac{i\pi}{k_\parallel} \left(\frac{\partial F_e}{\partial v_\parallel} \right)_{v_\parallel = \omega / k_\parallel} \right]. \tag{4.8}$$

The contour integral is calculated by integrating around a complex pole[115]. We let ω tend towards zero from the domain $\omega_i > 0$ and integrate around a semicircle of infinitesimal radius. If the distribution does not deviate much from a Maxwellian, the principal part P, which defines ϵ_r, is dominated by the cold plasma terms with solution $\omega = \omega_r$.

If the imaginary component is small compared to the real part of the integral, it may be treated as a small perturbation such that the linear growth rate is described by:

$$\gamma = -\frac{\omega_r \epsilon_{im}}{2}. \tag{4.9}$$

We note here that this expression is only valid when the condition $\omega_{pe} \ll \Omega_{ce}$ is true. If this is not the case, we can instead expand:

$$1 - \frac{\omega_{pe}^2 \cos^2\theta}{\omega^2} - \frac{\omega_{pe}^2 \sin^2\theta}{\omega^2 - \Omega_{ce}^2} + \epsilon_{im} = 0, \tag{4.10}$$

for $\omega \approx \omega_0 + i\gamma$. This expansion yields the expression:

$$\gamma = -\frac{\omega_r \epsilon_{im}}{2} \left(\frac{\omega_r^2 \left(\Omega_{ce}^2 - \omega_r^2 \right)^2}{\omega_{pe}^2 \left(\Omega_{ce}^2 \left(\Omega_{ce}^2 - \omega_r^2 \right) \cos^2\theta \right)} \right), \tag{4.11}$$

which differs slightly from the expression used in Dendy et al.[114]. Following the original work, and substituting the imaginary part of Equation 4.8 into Equation 4.9 gives an expression to describe the linear growth rate γ of only the $n = 0$ Cerenkov resonance,

$$\gamma_{LE} = -\omega_r \frac{\omega_{pe}^2 \Lambda_0(\beta_B)}{2k^2} \left(\pi \frac{\partial F}{\partial v_\parallel} \right)_{v_\parallel = \omega / k_\parallel}. \tag{4.12}$$

This expression describes Landau damping when the slope of the distribution function evaluated at $\omega / k_\parallel$ is negative and inverse Landau damping when the slope is positive. In the limit of $\omega_{pe} \ll \Omega_{ce}$ we may use the expression $\omega_r = \omega_{pe} k / k_\parallel$ to describe the longitudinal bulk plasma mode. Plugging this into Equation 4.12 we arrive at the same result as was calculated by Dendy and Lashmore-Davies:

$$\frac{\gamma_{LE}}{\omega_{pe}} = -\pi^{1/2}\left(\frac{\omega_{pe}}{kv_B}\right)^2 \Lambda_0(\beta_T)\frac{k_\parallel}{k}\left(\frac{\pi^{1/2}v_B^2}{2}\frac{dF}{dv_\parallel}\right)_{v_\parallel=\omega_{pe}/k_\parallel}. \tag{4.13}$$

The same process that is outlined above may also be applied to the $n=-1$ electron cyclotron resonance:

$$\epsilon_L = 1 - \frac{\omega_{pe}^2\Lambda_1\left(\beta_B\right)}{k^2}\int_{-\infty}^{\infty}\frac{dv_\parallel}{k_\parallel v_\parallel - \Omega_{ce} - \omega}\left(k_\parallel\frac{\partial F_e}{\partial v_\parallel} + \frac{2\Omega_{ce}}{v_B^2}F(v_\parallel)\right). \tag{4.14}$$

Removing the principle part of the integral gives the expression:

$$\epsilon_{im} = -\frac{\omega_{pe}^2\Lambda_1(\beta_B)}{k^2}\left[\pi\frac{\partial F_e}{\partial v_\parallel} + \pi\frac{2\Omega_{ce}}{k_\parallel v_B^2}F_e(v_\parallel)\right]_{v_\parallel=(\omega+\Omega_{ce})/k}. \tag{4.15}$$

Finally, we may substitute this into Equation 4.9,

$$\gamma_{AD} = -\frac{\omega_r\omega_{pe}^2\pi\Lambda_1(\beta_B)}{2k^2}\left[\frac{\partial F_e}{\partial v_\parallel} + \frac{2\Omega_{ce}}{k_\parallel v_B^2}F_e(v_\parallel)\right]_{v_\parallel=(\omega+\Omega_{ce})/k}. \tag{4.16}$$

This gives the same linear growth as those which were calculated by Dendy and Lashmore-Davies when the principle solution $\omega_r = \omega_{pe}k_\parallel/k$ is applied,

$$\frac{\gamma_{AD}}{\omega_{pe}} = \pi^{1/2}\left(\frac{\omega_{pe}}{kv_B}\right)^2\Lambda_1(\beta_T)\left[\frac{\Omega_{ce}}{kv_B}\left(\frac{v_B}{v_{T_\perp}}\right)^2\pi^{1/2}v_BF(v_\parallel) + \frac{k_\parallel}{k}\frac{\pi^{1/2}v_B^2}{2}\frac{dF}{dv_\parallel}\right]_{v_\parallel=(\omega+\Omega_{ce})/k}. \tag{4.17}$$

Rather than describing the longitudinal mode by the expression $\omega = \omega_{pe}\cos(\theta)$ we may instead use the expression $\omega_r^2 = \omega_-^2 = \frac{1}{2}\omega_h^2 - \frac{1}{2}\sqrt{\omega_h^4 - 4\Omega_{ce}^2\omega_{pe}^2\cos^2\theta}$. This slight modification is more applicable as we consider parameters where ω_{pe} is comparable to Ω_{ce}. The small modification slightly shifts the location in k space where we may expect to see growth and also slightly modifies the magnitude of the growth which we predict.

In these calculations we have neglected to consider the $n=1$ normal Doppler electron cyclotron resonance. Under most conditions this approximation is reasonable although we note that linear calculations performed which additionally considered damping at the normal Doppler resonance were later performed by Omelchenko et al.[116]. We do not outline these linear calculations here, although they state that

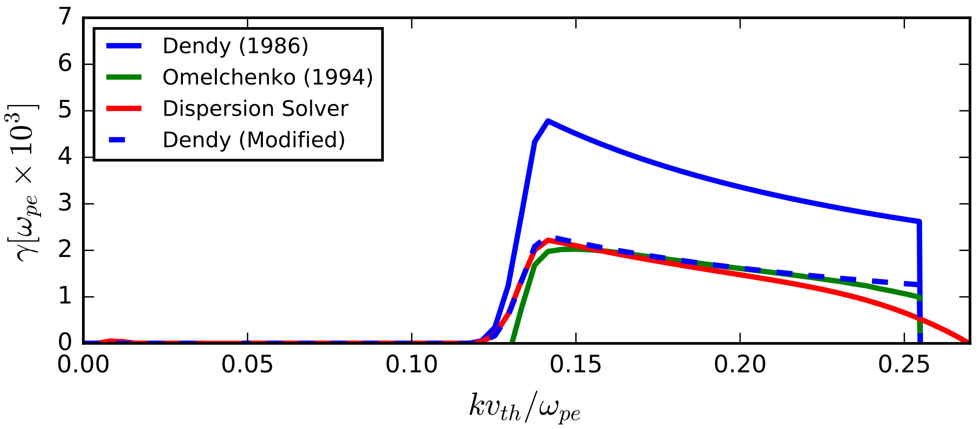

Figure 4.5: Comparision of analytically calculated wave-particle linear growth rates at angle $\theta = 45^o$ from the magnetic field for distribution function 4.6. Growth rates calculated using the prescription from Dendy and Lashmore-Davies are shown in blue[114], while growth rates based on work by Omelchenko et al. are shown in green[116]. Growth rates computed by numerically solving Equation 3.38 for the same distribution function are shown in red. We apply Equation 4.11 instead of Equation 4.9 to compute the dashed blue line.

the growth rates are given by:

$$\gamma = \frac{\pi \alpha^3 \Omega_{ce}^2 k_\perp^2}{4 n_0 k^3} \left[F_0 \left(\frac{\omega + \Omega_{ce}}{k_\parallel} \right) - F_0 \left(\frac{\omega - \Omega_{ce}}{k_\parallel} \right) + \frac{2\Omega_{ce} k_\parallel}{k_\perp^2} \frac{\partial F_0}{\partial v_\parallel} \left(\frac{\omega}{k_\parallel} \right) \right], \tag{4.18}$$

where the constant $\alpha = 1/(1 + \omega_{pe}^2/\Omega_{ce}^2)^{1/2}$ is defined. This result was calculated using a technique broadly similar to that used by Dendy and Lashmore-Davies[114], where only the longitudinal component of the dielectric tensor was solved. Calculations by Omlchenko et al. also appear to be applicable when the condition $\omega_{pe} \ll \Omega_{ce}$ is not necessarily true as the normal Doppler resonance is also considered.

We have outlined three separate methods to calculate linear growth rates and now compare these methods. This comparison is shown in Figure 4.4. We see that good agreement exists between growth rates calculated by the solver which we have constructed and Omelchenko et al.[116]. There appears to be some disagreement between the two, particularly at high k. This is likely because the growth rates calculated by Omelchenko do not consider the effect which thermal corrections have on the frequency of the lower bulk branch. This correction in turn modifies the resonant velocity for a particular value of k.

In the work by Dendy and Lashmore-Davies the assumption $\omega_{pe} \ll \Omega_{ce}$ is

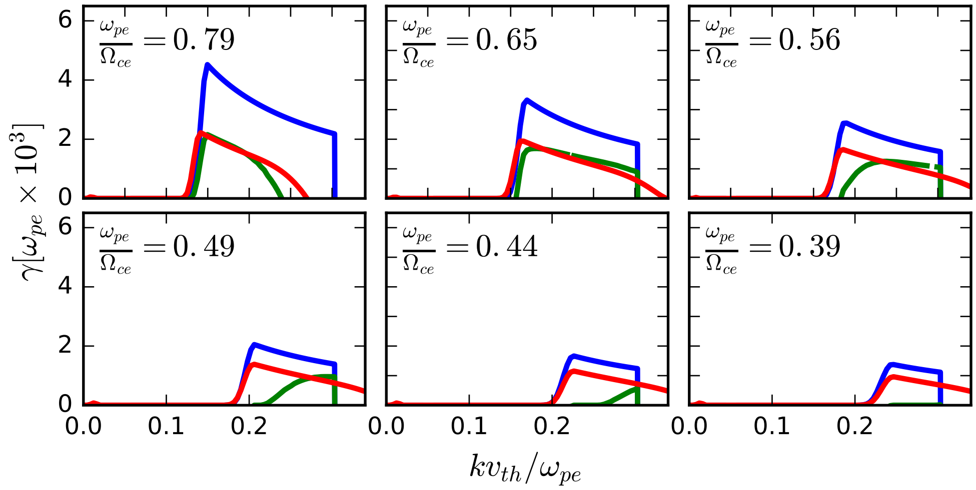

Figure 4.6: Agreement between growth rate calculations is compared for a range of values of the ratio ω_{pe}/Ω_{ce}. Growth rates calculated using the prescription from Dendy and Lashmore-Davies are shown in blue[114], growth rates based on work by Omelchenko et al. are shown in green[116] and growth rates computed by numerically solving Equation 3.38 are shown in red.

made[114]. In this regime normal Doppler damping is not important on the lower branch. Even when relaxing this assumption to the parameters that we have used ($\omega_{pe}/\Omega_{ce} = 0.8$) the addition of normal Doppler damping still appears to have little effect at this angle. If we were to consider the upper bulk plasma branch instead of the lower one this would not be the case. We see that for these values of ω_{pe} and Ω_{ce}, the growth rates computed by Dendy and Lashmore-Davies are out by over 50%. If we instead substitute Equation 4.11 instead of Equation 4.9 in this calculation, the growth rates are rectified.

The assumptions that growth rates are small and that the distribution function is within the kinetic regime both appear to be valid. The longitudinal component of the dielectric tensor may be separated by evaluating the expression $\epsilon_L = \mathbf{k}\cdot(\boldsymbol{\epsilon}\cdot\mathbf{k})$. During this investigation we verified that the longitudinal approximation is appropriate for study of the ADI, giving growth rates which differ from those calculated using the complete dielectric tensor by only a fraction of a percent. This result is to be expected as the degree of polarization of the lower bulk branch is very close to zero. In Figure 4.6 we vary the ratio ω_{pe}/Ω_{ce} in order to check the first assumption.

It can be seen that when the ratio of ω_{pe}/Ω_{ce} is small the growth rates which we have calculated by solving the full gyrotropic wave equation agree much better with those of Dendy and Lashmore-Davies than when this ratio is large. This small ratio was the original intended regime for validity. We note that even at $\omega_{pe}/\Omega_{ce} \approx 0.4$ this agreement is not perfect, although for most purposes it is likely to be sufficiently accurate. The growth rates calculated by Omelchenko et al. do not appear to be accurate for low values of the ratio ω_{pe}/Ω_{ce}.

Although we can compute linear growth rates through numerical means the previous approaches developed by Dendy and later Omelchenko are much simpler to compute and therefore still remain useful. These approaches offer a large computational performance advantage due to their relative simplicity. Certain applications, such as quasilinear codes, still benefit from derivations using this approach which can be computed quickly[117]. In our work however, we are satisfied with the reduced performance offered by the more general root finding approach used in our dispersion solver. This dispersion solver is used to calculate linear growth rates later in this chapter. The most robust means to benchmark the accuracy of linear growth rate calculations (short of laboratory experiments) is to compare against growth rates measured fully from kinetic PIC simulations. The simulation setup which we use to study the physics of the ADI is outlined in the next section.

4.3 Kinetic Simulation

4.3.1 Simulation motivation

Previously, kinetic PIC simulations of the ADI were investigated by Lai et al.[118, 119]. Simulations of this nature are a far more powerful tool to investigate physics than just linear calculations. We can investigate the time evolution of phase space, the saturation energy of various waves and fully non-linear effects such as wave-wave coupling or even turbulence[120].

The previous 1D3V PIC simulations were performed with only one spatial direction of variation so that the authors could only resolve waves travelling in that simulated direction. In this limited configuration the ADI is resolved specifically for angle θ, where the magnetic field is oriented at angle θ from the simulation domain. To resolve a larger spectrum of wavevectors propagating in other directions, we must perform 2D3V simulations where the magnetic field is oriented parallel to one of the directions of spatial variation. This higher dimensionality incurs a significantly increased computational cost. With the ever increasing availability of high performance computing resources, this cost is only now tractable. Due to the rotational symmetry in phase angle ϕ there is no immediate motivation to perform spatially homogeneous simulations in 3D3V.

Performing simulations which are 2D3V is useful because we can not only resolve the ADI at many angles simultaneously in time, but also other physical effects which may occur at entirely separate angles. A treatment which more closely resembles that found within tokamak devices could in principle consider effects of device geometry. We are able to somewhat skirt this requirement through the observation that the physical length and time scales at which electron physics occurs are relatively small compared to those implicated at device scale. Over the entire simulation duration only a few photon crossing times occur. We will now move on to discussing the specific simulation parameters that we have used.

4.3.2 Bulk parameters

In the 2D3V particle-in-cell simulations reported here, the full gyro-orbit electron dynamics, together with all three vector components of $\mathbf{E}(\mathbf{r},t)$ and $\mathbf{B}(\mathbf{r},t)$ evolve self-consistently under the relativistic Lorentz force law and Maxwell equations. In these simulations the following bulk parameters were used. Electron number density was set to $n_e = 2.5 \times 10^{19} m^{-3}$ and a constant background magnetic field of $B = 2T$ was applied. These were selected to be loosely in accordance with bulk parameters found in large tokamaks such as JET, DIII-D, K-Star or Asdex-U.

These parameters gave a ratio of electron cyclotron frequency to plasma frequency of $\Omega_{ce}/\omega_{pe} = 1.31$. Assuming that both relativistic effects and collisions may be neglected, the simulation results presented here may be scaled as long as this ratio is held constant. Both the proton and electron bulk thermal temperatures were set to $T_e = T_p = 100eV$ where the thermal velocity is defined as $v_{th} = \sqrt{k_b T/m_s}$ for both protons and electrons. These temperatures are sufficiently high that the collisional time-scale greatly exceeds the simulation duration while not so high that relativistic effects play an important role at oblique angles. At simulation initialization, electrons were sampled from a distribution composed of a flat tail and a warm Maxwellian background which was described in Equation 4.6.

The parameters used to define this distribution were a maximum flat tail velocity of $v_1 = 18.5v_{th}$ and an electron tail fraction of $\xi = 0.04$. Following distribution initialization a small shift was applied to the parallel electron velocity distribution such that the zero current condition $\mathbf{J}_e = \sum_i w_i \mathbf{v}_i q_e = \mathbf{0}$ was satisfied. This is a requirement imposed by the periodic boundaries that we have used. A background proton population was added to the simulation in order to satisfy quasineutrality, although it is not strictly necessary that this requirement be satisfied. This species was sampled from a Maxwellian distribution defined by $f_p(v_\parallel, v_\perp) = \exp[-v_\parallel^2/2v_{th}^2]\exp[-v_\perp^2/2v_{th}^2]/(2\pi v_{th}^6)^{1/2}$. We will also list the procedures which we have used to attain sufficiently high quality numerical resolution for these physical parameters.

4.3.3 Fine tuning

As we were interested in resolving waves for as large a number of different values of $\mathbf{k}$ as possible, we aimed to use a periodic simulation domain with many cells. A trade-off exists between the simulation domain size and the availability of computational resources. The performance cost of simulation is significantly greater in higher numbers of spatial dimensions. Considering this trade-off, simulations were performed on a 1000×1000 grid. As we are not interested in waves with the highest values of $\mathbf{k}$, it is useful to use cell sizes which are as large as possible. In this simulation we found that unrealistic dispersive effects started to occur for cell sizes around $\Delta x \approx 3\lambda_D$, where λ_D is the Debye length. We therefore configured each cell to have a size of $2.4\lambda_D$ in both of the spatial dimensions.

In addition to choosing cell sizes correctly, it is also important to select a sufficiently large number of particles per cell. In Section 4.4.3 of this chapter we will explain why the the physics of flat distributions which are unstable at the anomalous Doppler resonance requires a particularly large number of particles per cell to resolve. The most particles per cell which we could realistically utilize on a 1000 × 1000 spatial grid, given the computational limitations at the time of this study, was of the order of 1000 particles per cell. Macro-particle sampling was performed at a resolution of 1200 particles per cell, where species weighting was calibrated so that only 1/6 of the simulation macro-particles represented protons. Individual electron particle weights were varied such that the initial second moment of macro-particle momentum $\sum w_i p_i^2$ was minimized. Now that we have outlined the bulk parameters and fine tuning for the 2D3V PIC simulation that we have performed we will discuss the simulation results.

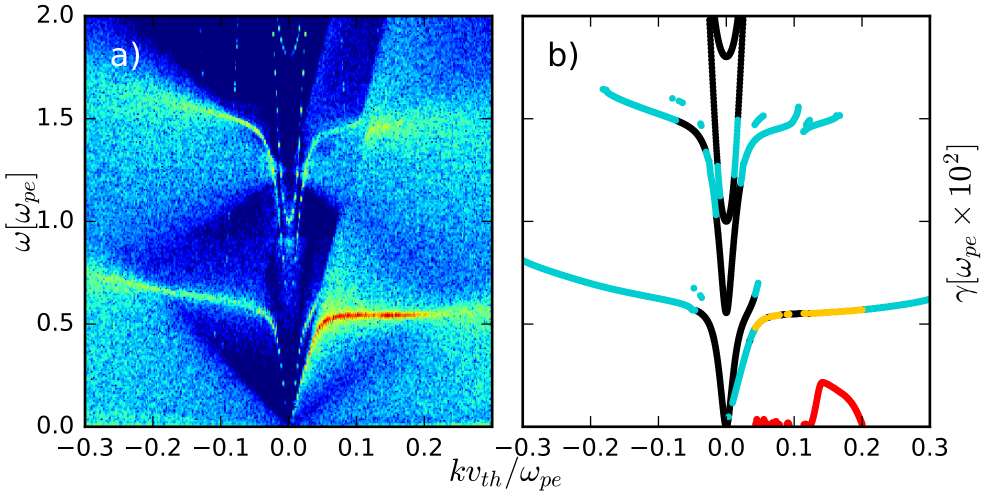

Figure 4.7: Panel a): Spatiotemporal Fourier transform of the parallel component of the electric field computed at angle $\theta = 45$ for early times between $t_1 = 83\tau_{ce}$ and $t_2 = 250\tau_{ce}$. Regions in blue indicate low power while regions in red indicate high power. Panel b): The solution to the gyrotropic wave Equation 3.38 is computed numerically using an electron distribution function and bulk parameters corresponding directly to simulation data averaged between times t_1 and t_2. Black lines correspond to the real part of stationary solutions, cyan lines show damped solutions and yellow lines show growing solutions. Red lines show the imaginary component of growing solutions and are exaggerated by a factor of 10^2.

4.4 Simulation Results

A large number of diagnostics were investigated during the analysis of simulation data. We will begin by comparing the linear dispersive properties of these simulations to linear predictions which we have made. This is followed by an examination of the quasilinear evolution of the underlying particle distribution functions under action of this linear physics. Finally, we will examine some of the non-linear physics associated with coherent wave-wave coupling. We aim to demonstrate that we have contributed to the knowledge base by providing a highly detailed account of the physical effects which may be associated with the fanning out of runaway electron tails.

4.4.1 Dispersive Properties

In Figure 4.7 we compare the spatiotemporal Fourier transform of the parallel electric field computed at early times from simulation output to a corresponding dispersion relation which was calculated using the electron velocity distribution function sampled directly from the same numerical simulation and time period. Both panels are computed using identical bulk parameters and for the same angle from the magnetic field. The methodology used to compute the 2D spatiotemporal Fourier transform of the electrostatic fields was defined in Section 2.2.4 and the dispersion relation in Section 3.2. We highlight that on the right-hand panel growth rates are also computed. The real and imaginary parts of the dispersion relation are represented on different scales. To ease comparison, the imaginary part is magnified by a factor of 100 relative to the real part. The real part of stationary solutions is represented by black lines. The real component of unstable solutions is plotted in purple, where the magnified imaginary component is shown in red. Damped solutions are also shown in grey although we do not show the imaginary component of these modes here. A near one to one mapping may be seen between the real component of the solved dispersion relation and the spatiotemporal Fourier transform. All cold electron plasma dispersive modes are captured fully, including an accurate description of the effects caused by non-zero electron temperature. This can be seen by the increasing frequency at high values of k. The unstable regions marked in purple closely correspond to enhancements on the bulk branch in panel a).

As we have performed simulations in more than one spatial dimension, it is also useful to compare Fourier transforms over a range of angles. In Figure 4.8 we show Fourier transforms which are computed using the parallel component of the electric field for angles between $\theta = 0^o$ and $\theta = 90^o$ from the magnetic field direction. These plots were computed between times $t_1 = 83\tau_{ce}$ and $t_2 = 166\tau_{ce}$ from the simulation onset.

In panel a) we can clearly see that the dispersion relation is dominated by Langmuir waves travelling in the magnetic field direction with frequency $\omega \approx \omega_{pe}$. These waves are purely electrostatic and should be stable against collective instability for a monotonically decreasing tail. Interestingly, significant power appears to exist at this mode from simulation onset. To fully explain the initial power of this mode it is necessary to understand the process behind spontaneous Cerenkov emission. We will discuss this in Section 4.4.3.

Panel b), which is situated at 30^o from the magnetic field direction, shows the two bulk modes at separate frequencies. The resonant frequency of these modes may be approximated by Equation 2.12. In this simulation the non-thermal electron tail constitutes a non negligible part of the distribution function. The precise frequency of these modes therefore slightly deviates from what would be predicted by a purely cold plasma model. As we have outlined in Section 2.2.3, these are known as the

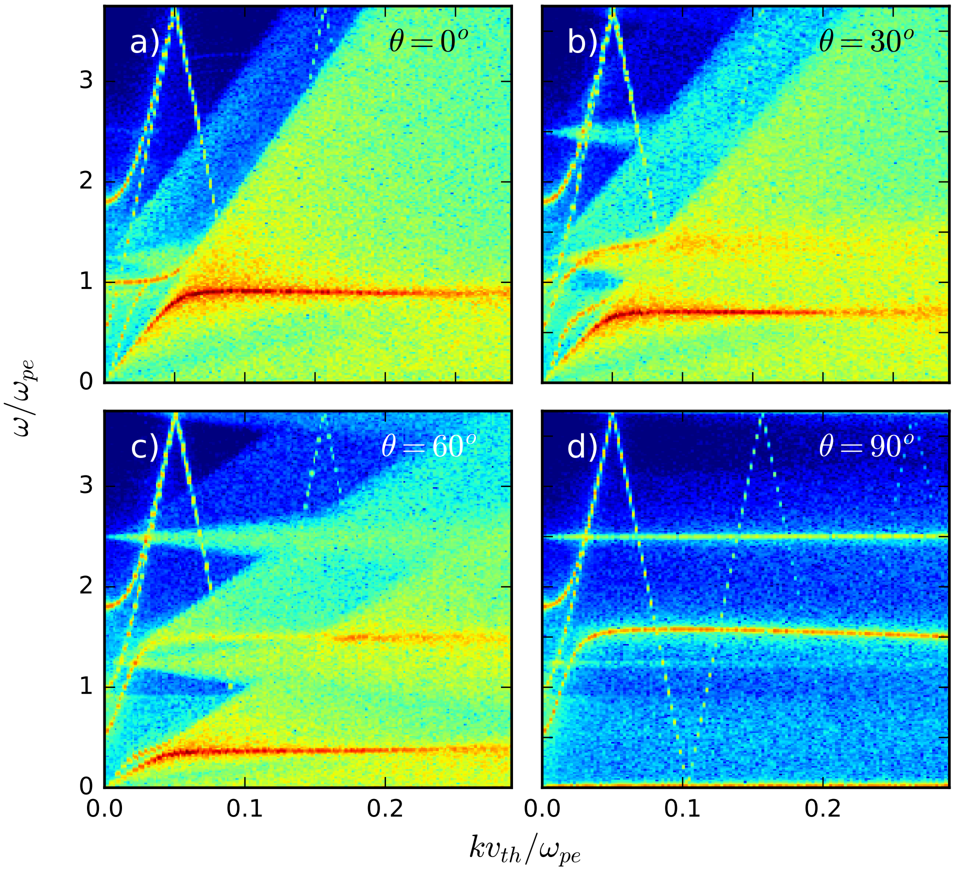

Figure 4.8: Spatiotemporal Fourier transforms are computed at various different angles for each component of the electric field. The total magnitude of all three components is then plotted. Panels a), b), c) and d) are computed for angles $\theta = 0^o$, 30^o, 60^o and 90^o respectively. Fourier transforms are performed between times $t_1 = 83\tau_{ce}$ and $t_2 = 166\tau_{ce}$

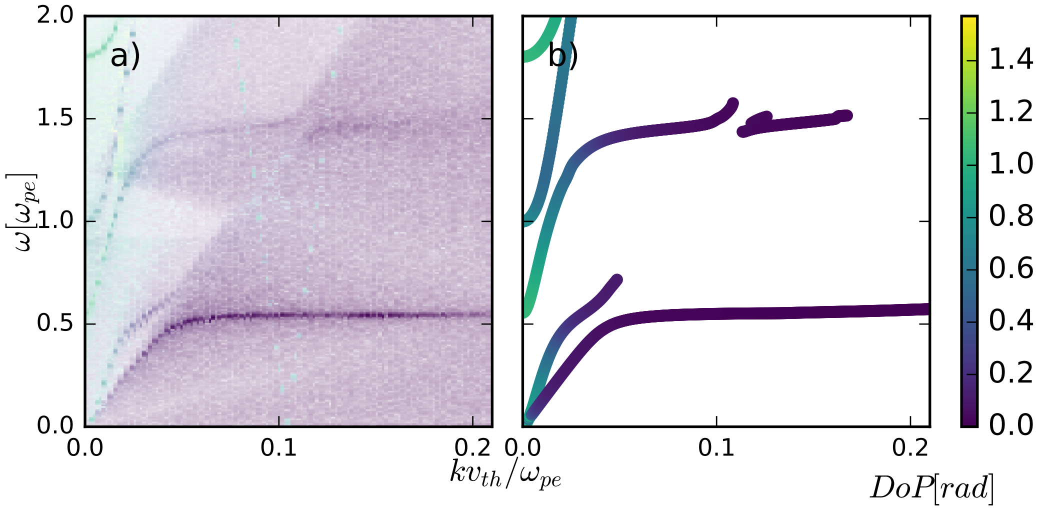

Figure 4.9: Degree of electromagnetic polarization computed for wave propagation angle $\theta = 45^o$ from the magnetic normal. Purely electrostatic waves are shown in blue, while purely electromagnetic waves are shown in yellow. Waves which are partly electrostatic and partly electromagnetic are shown in teal. Panel a) shows results computed from simulation while panel b) shows the analytically computed counterpart. To illustrate intensity panel a) is also tinted to convey the power, where lighter regions are less intense.

Z and W modes. They are also frequently referred to as the upper and lower bulk plasma modes. Panel c) shows broadly the same features as panel b). The frequencies of the upper and lower bulk modes are modified in accordance with their dependence on θ. The O and X modes can be seen to vertically reflect in every panel at $\omega \approx 3.7\omega_{pe}$. This spurious effect is due to the finite frequency at which the electric field was sampled. As 2D simulations produce larger amounts of data, we were data constrained in sampling frequency. Panel d) shows only waves travelling in the direction perpendicular to the magnetic field. The upper hybrid resonance, $n = 1$ cyclotron resonance and $n = 2$ cyclotron resonance are visible here. Finally, in all but the first panel, the $n = 1$ and $n = 2$ cyclotron harmonics are also visible. In principle, the $n = 2$ and $n = -2$ harmonics may have a wave-particle interaction similar to the normal and anomalous Doppler effects. In practise these interactions are much less important due to the more stringent requirements on non-damping at the resonance conditions of these higher harmonics. So far, we have not differentiated between polarized and non-polarized modes. In Figure 4.9 we investigate these properties more closely.

Rather than considering the sum of electric field oscillations, it is perhaps more useful to consider the polarization of particular modes. In Figure 4.9 we examine the degree of polarization for waves travelling at angle $\theta = 45^o$ from the magnetic field.

We use the phrase "degree of electromagnetic polarization" to describe the degree to which waves are electrostatic or electromagnetic. A degree of polarization of 0 indicates a wave which is purely electrostatic while a degree of polarization of $\pi/2$ represents a wave which is purely electromagnetic. Degree of electromagnetic polarization is computed, through the techniques outlined in Section 2.2.5, at time $t = 83\tau_{ce}$ in the simulated results reported here. We see that very good agreement exists between the degree of electromagnetic polarization measured in simulations and the degree of electromagnetic polarization that was calculated analytically for the velocity distribution at this time period.

A key observation is that waves at the anomalous Doppler resonance are not purely electrostatic. At $\theta = 0^o$ the degree of polarization of the longitudinal mode is exactly electrostatic. As θ is increased, the degree of polarization on the bulk branch deviates slightly from being purely longitudinal. For the wavevector $k = 0.2\omega_{pe}/v_{th}$ and propagation angle equal to $\theta = 45^o$ tensor $\mathbf{M}$ has an eigenvalue of $\lambda = 0$ when the argument $\omega = 0.57\omega_{pe} + 0.00015j\omega_{pe}$ is supplied. The normalized electric field eigenvector corresponding to this solution is $\mathbf{E}_{\omega,\mathbf{k}} = (0.709, -0.002j, 0.705)$. The unit vector of wave propagation is $(1, 0, 1)/\sqrt{2}$. These vectors are not completely parallel which means that the wave is not purely electrostatic. Taking the inverse cosine of their dot product reveals a degree of polarization of $DoEP = 0.0038$. While the majority of wave excitation is electrostatic, a non-negligible electromagnetic component still exists. This has significant implications for the possibility of directly detecting electromagnetic radiation originating from the ADI. Now that we have examined the dispersive and linear properties of the ADI we will examine the quasilinear effects that waves caused by this instability may have on the electron velocity distribution.

4.4.2 Quasilinear Evolution in Phase Space

Quasilinear effects occur when the unperturbed velocity distribution function evolves self-consistently in response to the presence of excited waves. The first analytical treatment for wave-particle resonant quasilinear diffusion in velocity space for magnetized plasmas was performed by Kennel and Engelmann[121]. Relativistic quasilinear treatments were also later adapted by Kulsrud and Ferrari[122]. Quasilinear diffusion in the context of single particle lagrangian dynamics and the ADI was explored by Dendy in 1987[123]. More recently this was in part verified by Lai et

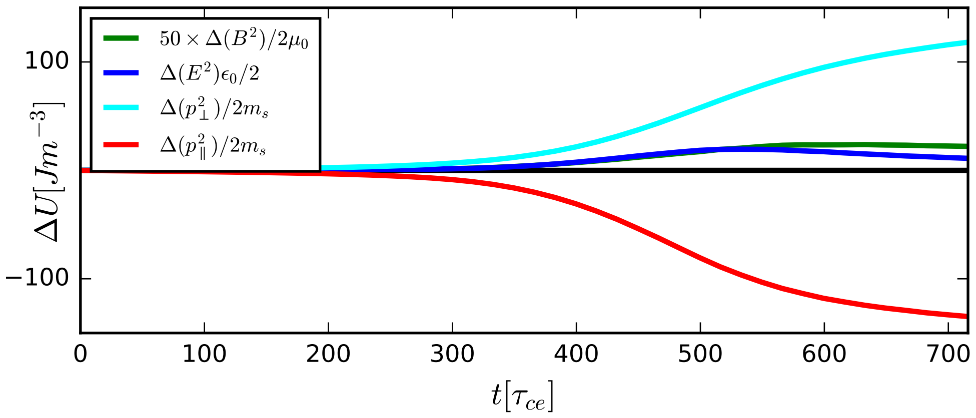

Figure 4.10: Deviation from initial energy density is computed between times 0 and $700\tau_{ce}$. Kinetic energy density change of the parallel and perpendicular momentum components are shown in red and cyan respectively. The change in electric field energy density is shown in blue and the magnetic field energy density (adjusted for visibility) in green. The black line shows change in total energy density.

al. who tracked single particle electron trajectories in PIC simulations[119]. The verification of bulk quasilinear diffusion rates driven by the ADI using the ensemble averaging of many particles remains an unanswered question for future research. Accurate quasilinear diffusion modelling is necessary to understand kinetic effects on collisional time-scales which exceed those which may be addressed with PIC codes.

In our work we only consider the modification of growth rates caused by the evolution of the zeroth order electron distribution. We do not consider the action of the electric and magnetic fields on the zeroth order particle distributions. It is well known that the ADI causes electron velocity diffusion from the parallel to perpendicular directions. A postulate which has hitherto been unverified is whether or not this diffusion can lead to the formation of a positive slope in the parallel direction of the electron distribution. This was first proposed by Molvig et al.[99], who suggested that the fanning out of an extended flat electron tail could lead to the formation of positive slope in the perpendicular integrated electron distribution. This suggestion was shortly followed by a similar prediction by Papadopoulos et al. [124]. In this section we aim to address this postulate by first investigating the evolution of the velocity component of phase space which is calculated in numerical simulation. We will then attempt to measure the effect which this modification of phase space has on growth rates at later times in the simulation.

To begin with we examine the time evolution and energy transfer between the electromagnetic fields and electron momentum components in the parallel and

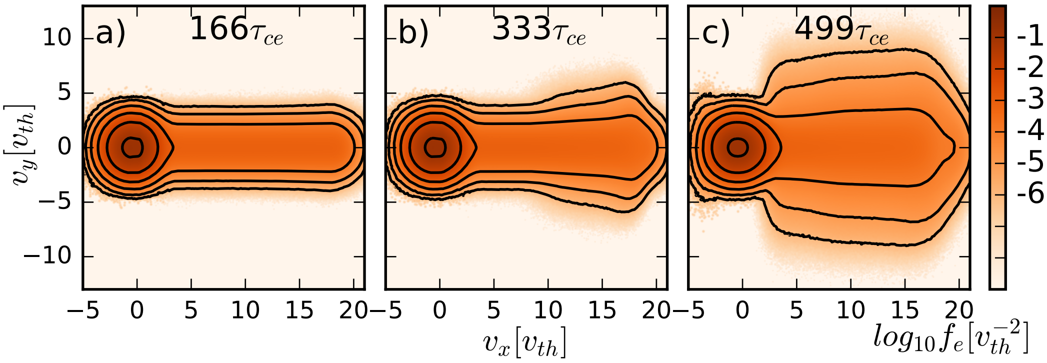

Figure 4.11: Electron distribution functions for velocity components v_x and v_y are plotted at various times. On the left-hand side in panel a) we see that the initial configuration remains unchanged at time $t = 166\tau_{ce}$. The central and right-hand panels show times $t = 333\tau_{ce}$ and $499\tau_{ce}$ respectively.

perpendicular directions. This is shown in Figure 4.10. The lack of any visible deviations from zero in the black line shows that total energy is conserved throughout the simulation. Very little change in the particle distributions occurs before $t = 300\tau_{ce}$. This period is dominated by linear growth of the electric field. After this time significant energy transfer occurs between the parallel and perpendicular momentum components. This is the quasilinear stage of the ADI. The result is a fanning out of the initially highly anisotropic energetic electron tail. We see that the electric and magnetic fields reach saturation at around $t \approx 600\tau_{ce}$. Beyond the saturation time a large amount of momentum transfer still continues to occur, although the rate is progressively reduced. To understand the process of quasilinear diffusion in more detail we may investigate the parallel and perpendicular components of the electron velocity distribution function. This is shown in Figure 4.11.

In the central panel of Figure 4.11, at time $t = 333\tau_{ce}$, we see that a slight fanning out of the electron tail has occurred. This quasilinear diffusion in phase space is caused by the wave-particle Anomalous Doppler resonance between the lower bulk branch and energetic particles in the electron tail driving electrostatic waves on the lower bulk branch. These waves then act to modify the underlying particle distribution. Panel c) shows a time at which significant deviation from the initial distribution has occurred. Although saturation of wave energy has occurred at this time, quasilinear diffusion in phase space still continues to occur at a reduced rate, further isotropizing the electron tail.

In Figure 4.12 we examine parallel momentum rather than velocity. This is done to demonstrate that we are not simply observing a slight relativistic correction

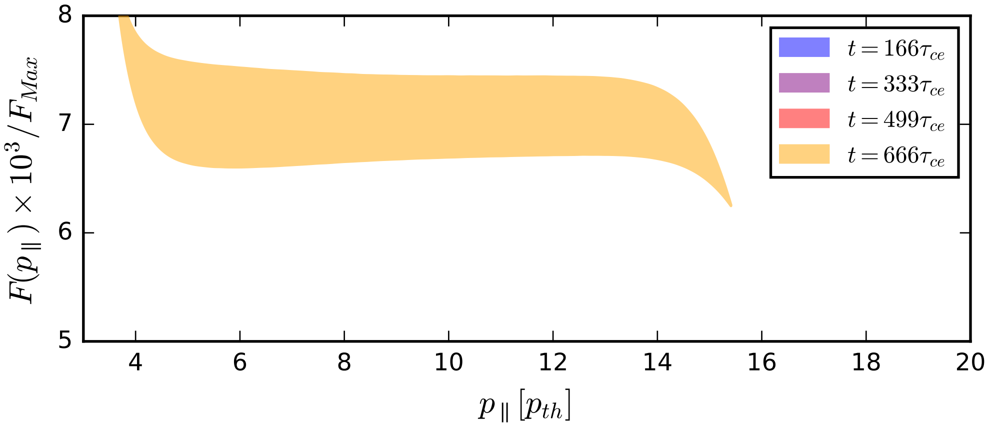

Figure 4.12: Perpendicular integrated parallel electron momentum is computed directly from simulated particle distributions for various times. These correspond to the same times that are shown in Figure 4.12 with the addition of time $t = 666\tau_{ce}$. A positive slope is clearly visible at times $t = 333\tau_{ce}$ and $t = 499\tau_{ce}$.

to an otherwise flat momentum tail, but in fact a parallel distribution which has a positive slope in both velocity and momentum space. At early times the parallel distribution remains unchanged from the simulations initial configuration. At times $t = 333\tau_{ce}$ and $t = 499\tau_{ce}$ we see the emergence of a small positive slope. To explain this phenomena we must consider the effect of the Anomalous Doppler instability on the underlying particle distributions. The instability operates primarily to transfer particle momenta from the parallel direction to the perpendicular direction. Coupled with the fact that the ADI is strongest when the lower bulk branch is resonant with particles travelling at higher velocities towards the end of the tail, it becomes apparent that a positive slope may emerge.

4.4.3 Power Absorption and Spontaneous Emission

In Figure 4.13 we show the variation of electrostatic power density as a function of $\mathbf{k}$ for times between $t_1 = 83\tau_{ce}$ and $t_4 = 333\tau_{ce}$ in the simulation. The early-time electrostatic power density at the anomalous Doppler resonant region in $\mathbf{k}$-space is highlighted by annotation A. The power at this region rises incrementally between each panel. This behaviour is indicative of linear growth, which we shall analyse in more detail in Section 4.4.4. The Cerenkov resonant region is highlighted by annotation B. For this region a large amount of power exists even at early times in the simulation. The early excitation of electrostatic waves, which is strongest at $k_\perp = 0$ and $k_\parallel \approx 0.6\omega_{pe}/v_{th}$, cannot be explained by collective linear growth

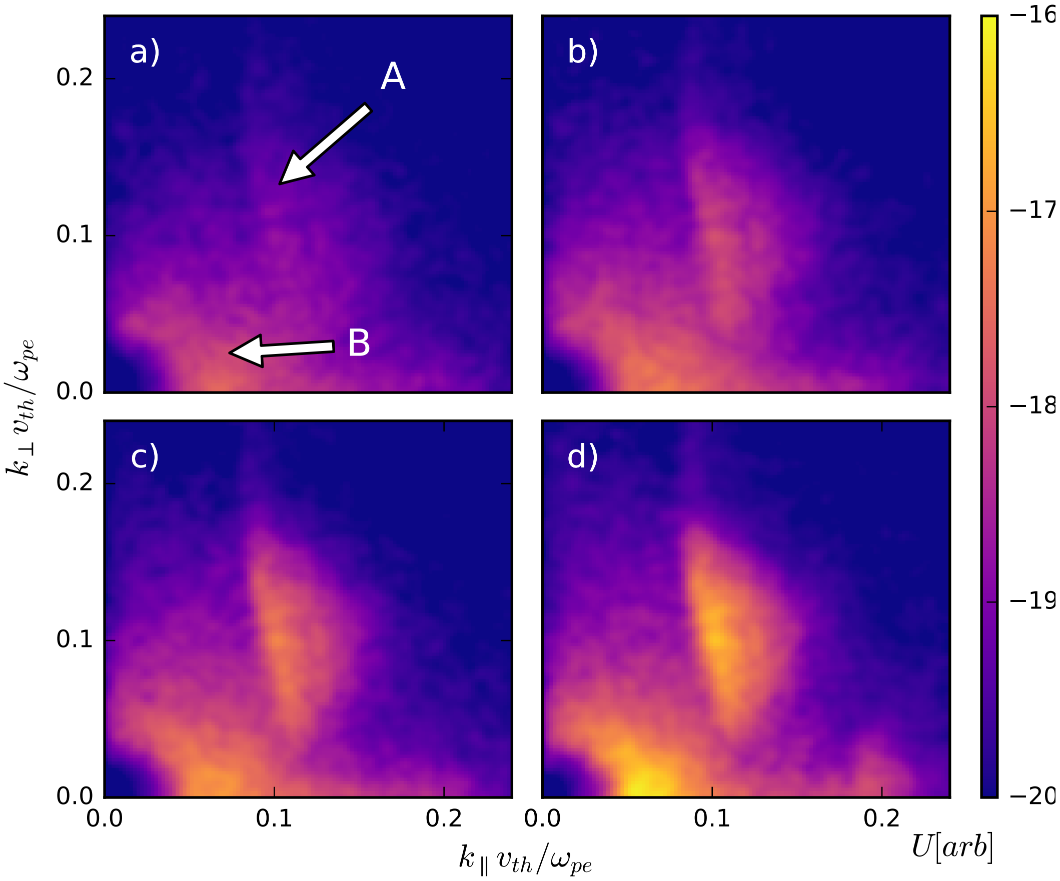

Figure 4.13: Electrostatic power density is shown for times $t_1 = 83\tau_{ce}$, $t_2 = 166\tau_{ce}$, $t_3 = 250\tau_{ce}$ and $t_4 = 333\tau_{ce}$ in panels a), b), c) and d) respectively. Areas marked in yellow indicate regions of $\mathbf{k}$ space where electrostatic wave energy is concentrated, while areas in blue show regions where it is not. Annotation A indicates the wave-particle anomalous Doppler resonant region, while annotation B shows the wave-particle Cerenkov resonant region.

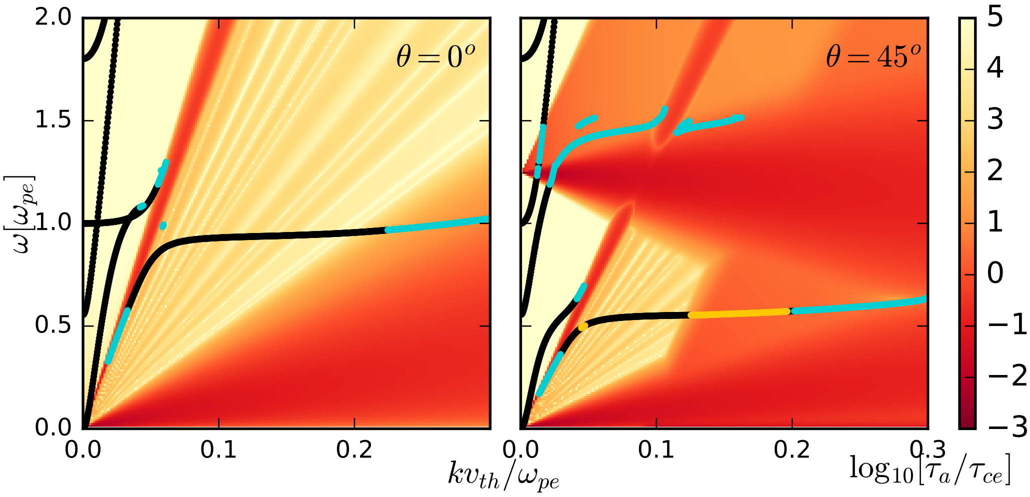

Figure 4.14: The characteristic decay time for an electrostatic fluctuation with frequency ω and wavevector $\mathbf{k}$ is calculated from Equation 4.19 for angles $\theta = 0^o$ and $\theta = 45^o$. The real part of the dispersion relation solution is overlaid for comparison.

as we have shown that a flat tail is stable against linear instability in this region of $\mathbf{k}$-space. Instead, we account for early power at this region by considering the physics of both absorption and spontaneous emission.

It is well known that black bodies emit and absorb thermal radiation. When a system is in equilibrium the rate of power absorption equals the rate of spontaneous power emission. This is best known as Kirchhoff's law of thermal radiation[125]. Kirchhoffs law also relates absorption and emission in steady state magnetized plasmas. The rate of spectral power absorption in magnetized plasmas may be readily calculated by considering the complex part of the dielectric tensor $\boldsymbol{\epsilon}$[69]. The rate of power absorption for electromagnetic waves in a dielectric media may be described as follows:

$$\frac{\partial W(\omega,\mathbf{k})}{\partial t} = \omega_r \frac{\epsilon_0}{2} \mathbf{E}^* \cdot \boldsymbol{\epsilon}^A(\omega,\mathbf{k}) \cdot \mathbf{E}, \tag{4.19}$$

where $\boldsymbol{\epsilon}^A(\mathbf{k},\omega) = \frac{1}{2}(\boldsymbol{\epsilon} - \boldsymbol{\epsilon}^\dagger)$ is the anti-hermitian component of the dielectric tensor. Using this expression we may solve a differential equation to evaluate the decay time $\tau_a(\omega,\mathbf{k})$ of an electric fluctuation with a specific wavenumber $\mathbf{k}$ and real frequency ω. In Figure 4.14 this quantity is calculated using the simulated electron distribution function at time $t_1 = 83\tau_{ce}$.

Fluctuation dissipation theorem was first investigated by Nyquist in 1928[126].

Fluctuation dissipation theorem relates the linear response of a system as it relaxes from a non-equilibrium state to its statistical fluctuation properties in equilibrium[127]. The longer a system takes to relax from a perturbed state, the longer it will take to reach statistical equilibrium. If the perturbation response is linear, then the time that it takes the system to reach an equilibrium state will not depend on the magnitude of the perturbation or fluctuation. We can relate this property to the fluctuation decay time shown in Figure 4.14. Strongly damped regions of the simulation will quickly reach equilibrium regardless of the magnitude of fluctuations, while regions which are not strongly damped will take much longer.

To determine the equilibrium power in the electric and magnetic fields we first need to determine the rate of spontaneous power emission. The rate of power emission and power absorption may then be equated and the equilibrium field energy solved as a function of $(\omega, \mathbf{k})$. Several different approaches to determining the spontaneous power emission rate exist.

The formalism for calculating the rate of spectral spontaneous power emission is more complex than the calculation of spectral absorption. Statistical physics must be considered in addition to the collective response of the dielectric medium. Much of the necessary statistical machinery is outlined in the textbook by Sitenko "Electromagnetic Fluctuations in Plasma"[128]. This textbook applies a Klimontovich formalism to allow the construction of the space-time correlation function and derives spontaneous emission rates in non-magnetized plasmas with isotropic velocity distributions. An approach which has been used previously was to calculate the rate at which test particles do work on the plasma[129]. This approach has been used in conjunction with the approximation that the real part of the dielectric tensor may be computed using only the cold plasma terms of the dielectric tensor to perform 1D ray tracing calculations of electron cyclotron emission in tokamaks which use electron cyclotron resonance heating[130]. As this approach assumes that spontaneous emission only occurs at solutions to the dispersion relation it is limited in generality. It is possible to calculate spontaneous emission rates for any values of $(\omega, \mathbf{k})$. From PIC simulations we can see that power does not exist just on the solution to the dispersion relation, but across a wide range of values in ω and $\mathbf{k}$.

Another approach to calculating the equilibrium field energy which does not have this limitation is to solve the inhomogeneous wave equation. This approach has recently been explored in detail for magnetized plasmas with Maxwellian[131] and Kappa[132] velocity distribution functions. This theory has been verified against fully kinetic PIC simulations[133] and for thermal magnetized plasmas[134]. The inhomogenous wave equation is:

$$\mathbf{M}_{ij}(\mathbf{k},\omega)\left\langle\delta E_i\delta E_j\right\rangle_{\mathbf{k},\omega}=\mathbf{M}^{-1}_{ij}(\mathbf{k},\omega)\left\langle\delta E_i\delta E_j\right\rangle^0_{\mathbf{k},\omega}, \tag{4.20}$$

where $\left\langle\delta E_i\delta E_j\right\rangle_{\mathbf{k},\omega}$ is the equilibrium electric field correlation tensor and $\left\langle\delta E_i\delta E_j\right\rangle^0_{\mathbf{k},\omega}$ is the source correlation tensor for modes with wavenumber $\mathbf{k}$ and frequency ω. The tensor $\mathbf{M}$ has been defined in Equation 3.38. When the right hand side of Equation 4.20 is set to $\mathbf{0}$, we return to the wave equation which we have solved in Chapter 3.2. The numerical implementation of the solution for the full inhomogenous wave equation for arbitrary gyrotropic velocity distribution functions is left as an item of future work. To solve this equation an expression describing the electric source fluctuations is required. According to [132] the electric source fluctuation term may be calculated for arbitrary velocity distribution functions using the equation:

$$\left\langle E_iE_j\right\rangle^0_{\mathbf{k},\omega}=\sum_s\frac{m_s\omega_{ps}^2}{2\pi^2\omega^2}\int_{-\infty}^{\infty}\int_0^{\infty}2\pi v_\perp dv_\perp dv_\parallel\sum_n V_n^iV_n^{j*}\delta(\omega-k_\parallel v_\parallel-n\Omega_{cs})f_s(v_\parallel,v_\perp), \tag{4.21}$$

where the compact notation

$$V_n=\left(\frac{n\Omega_{cs}}{k_\perp}J_n(k_\perp v_\perp/\Omega_{cs}),-iv_\perp J_n'(k_\perp v_\perp/\Omega_{cs}),v_\parallel J_n(k_\perp v_\perp/\Omega_{cs})\right),$$

is useful to describe the tensor elements. Here J_n describes a Bessel function of the first kind and J_n' describes its derivative with respect to $v_\perp$.

We can also gain understanding from a simpler argument based on scaling laws. This approach can aid us in understanding the temporal evolution of the electric and magnetic fields in PIC simulations and show how these relate to reality. Every particle in a plasma drives a small perturbation in the current density, δj_i. The magnitude of this perturbation is proportional to the total charge of the particle and its velocity, $\delta j_i\propto w_iq_sv_i$, where q_s is the species charge, w_i is the macro-particle weight and v_i is the velocity of macro-particle i. The number density of particles of species s is $n_s=\sum_i w_i$, which means that $w_i\propto n_s/N$. In PIC codes, macro-particles typically have a particle weight which represents many trillions of electrons or ions. The power in the current perturbations drives oscillations in the electric and magnetic fields. The total power in the ensemble of current perturbations is proportional to $\sum_{i,j}\delta j_i\delta j_j$, which when considering the variance of the macro-particle velocity distribution, scales as $1/N$. It is therefore instructive that the power in the perturbations in the electric and magnetic fields should also scale as $1/N$.

The simulations which we have performed are not initialized in statistical equilibrium. The electric and magnetic fields are initialized with constant fixed values, while the particle distributions contain noise due to finite sampling. Macroparticles in the code will then seed fluctuations in the fields. A steady state exists where the growth of fluctuations in the electric and magnetic fields is cancelled out by the damping caused by wave absorption. The time taken for this equilibrium to be reached is proportional to the decay time, which is plotted in Figure 4.14. The characteristic decay time of fluctuations at the anomalous Doppler resonance, marked by the yellow line on the left panel, is relatively short. However the decay time of fluctuations at the Cerenkov resonant region of the bulk branch, at slightly lower k however, is much longer. This means that it is difficult to measure collective growth in this region without also measuring growth driven by fluctuations. We can quantify the magnitude of this effect by performing convergence tests. In Figure 4.15 we have performed a series of simulations where the number of particles per cell is varied.

The simulations shown in Figure 4.15 are performed with only one spatial dimension. We chose to make this reduction so that we could reach a much higher number of particles per cell given limited computational resources. These simulations were performed with the same bulk parameters as the 2D3V simulations which are reported here. Each simulation was performed in a periodic box containing 1000 cells. The magnetic field was oriented at angle of $\theta = 45^o$ from the simulation domain. This allowed us to capture both the ADI and Cerenkov resonance independently. We note that the physics which we capture here may differ from the 2D simulation as waves which propagate at other angles are not resolved.

Several important physical observations may be made from examining Figure 4.15. Firstly, the initial energy at both the Cerenkov and anomalous Doppler resonant regions of k-space appears to scale as $1/N$, where N is the number of particles per cell. This is expected as fluctuations in the electric and magnetic fields are proportional to fluctuations in the underlying particle distribution functions which scale as $1/\sqrt{N}$. Secondly, we see that at around $t \approx 200\tau_{ce}$ the energy at the Cerenkov resonant region appears to flatten off. This can be explained by growth which is driven by fluctuations tending towards an equilibrium with the damping caused by the dielectric properties of the plasma. The time taken for this equilibrium to be reached does not depend on the number of particles per cell. It is also apparent that the dashed line depicts growth which is linear up until around $t \approx 400\tau_{ce}$. Growth rates for the ADI have good convergence, which is evident by the consistent gradients between the dashed lines for each simulation.

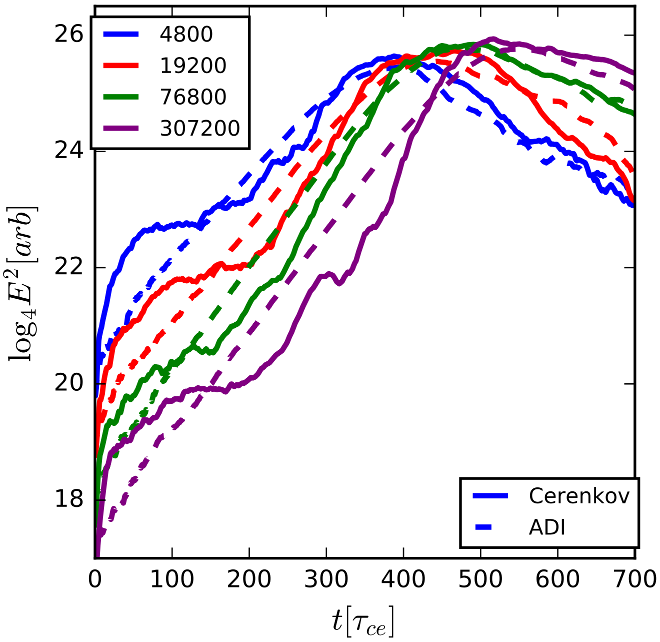

Figure 4.15: Filtered electric field energy is plotted for 1D simulations at angle $\theta = 45^o$ from the magnetic field. The mean energy of Cerenkov resonant wavenumbers between $k = 0.04\omega_{pe}/v_{th}$ and $k = 0.08\omega_{pe}/v_{th}$ is plotted with solid lines and the mean energy of anomalous Doppler resonant wavenumbers between $k = 0.12\omega_{pe}/v_{th}$ and $k = 0.16\omega_{pe}/v_{th}$ is plotted with dashed lines. Each colour represents a different number of particles per cell ranging from 4800ppc to 307200ppc. The base-4 logarithm is chosen because we increase particles per cell by a factor of 4 between each simulation.

After the fluctuation dissipation phase at $t = 200\tau_{ce}$ the Cerenkov and resonant region has an energy which roughly depends on the number of particles per cell. Power here is quasi-stationary as the fluctuations begin to approach saturation. Conversely, growth at the anomalous Doppler resonant region continues to occur. This means that the ratio of power between the anomalous Doppler and Cerenkov resonant regions does not converge. The quasilinear phase begins when waves at the Cerenkov region act to flatten the positive slope in the distribution while waves at the anomalous Doppler region cause it to grow. As the power at the start of the quasilinear phase is not fixed, the gradient of the positive slope does not converge. This means that we may start to see nonlinear and unpredictable behaviour in the simulation. The purple lines, which are measured from simulations with $N = 307200$ particles per cell, show the emergence of what appears to be nonlinear feedback effects in the slope of the parallel velocity distribution, where growth rates do not increase monotonically with time. Increasing the number of particles further may eventually result in convergence up until anomalous Doppler saturation time but it is not clear when this would occur. In the next section we discuss the effects which modification of the underlying electron distribution function have on the growth rates.

4.4.4 Quasilinear Growth Rates

We have shown that it is possible for a positive slope to evolve in the parallel component of the electron velocity distribution function. It is well known that a population inversion in the parallel direction may lead to instability due to inverse Landau damping. In this section we aim to measure growth rates which are produced in simulation and compare these to linear predictions made using the dispersion solver which we have outlined in Section 3.2. This will serve as both a benchmark for our dispersion solver as well as to help us identify the effects which cannot be captured by collective instability or spontaneous emission alone.

In Figure 4.16 we examine growth rates as a function of $k_{\parallel}$ and $k_{\perp}$. Panels a) and b) show growth rates which are computed numerically by directly solving the wave equation using the dispersion solver outlined in Section 3.2. These are computed using the electron velocity distribution function averaged between times $83 - 166\tau_{ce}$ and $250 - 333\tau_{ce}$. These linear growth rates are compared to growth rates which have been measured from simulation during the same time periods in panels c) and d). To compute the growth from simulation, a simple least squares fit is performed directly on the time series of the logarithm of the absolute value of the 2D spatial Fourier transform of the simulated electrostatic field. The gradient

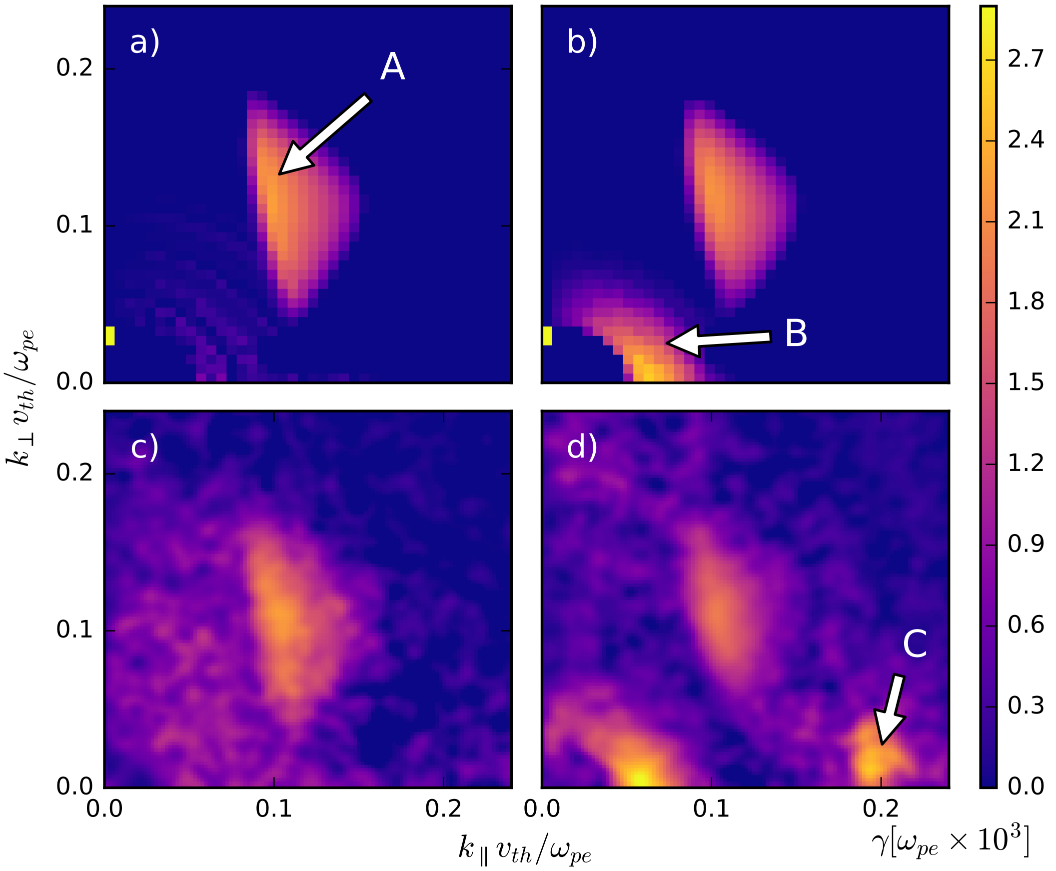

Figure 4.16: Panels a), b): linear growth rates are solved using Equation 3.38 for simulated electron velocity distributions averaged between times $t - 42\tau_{ce}$ and $t + 42\tau_{ce}$. Panels c), d): growth rates are measured from numerical simulation during the corresponding time period. Panels a) and c) show growth rates which are computed at time $t = 125\tau_{ce}$ and panels b) and d) are computed at time $t = 291\tau_{ce}$.

of this fit gives the individual growth rate for each value of $k_{\|}$ and $k_{\perp}$. Annotation C in Figure 4.16 shows a feature which is present in panel d) but not panel b). This discrepancy indicates that growth is driven by physics which is not captured by a purely linear treatment.

In general we see that the distribution in **k**-space of simulated growth strongly agrees with the regions of instability predicted by the dispersion solver. The magnitude of these growth rates also appears to closely correlate. For both of these cases, the left panel shows a period in time where the parallel electron distribution function has undergone little significant modification due to instability. This is the linear growth phase of the simulation. Clearly visible at annotation A is the location in $(k_{\|}, k_{\perp})$ space associated with the wave-particle Anomalous Doppler instability. Growth occurs here at $k_{\|}$ and $k_{\perp} \approx 0.11 v_{th}/\omega_{pe}$ with a maximum value of approximately $\gamma_{ad} = 0.0021\omega_{pe}$. The two right panels at later times are representative of the quasilinear phase of the simulation. In addition to the wave-particle Anomalous Doppler instability, these panels also depict the existence of a region in **k**-space excited by collective Cerenkov emission. This region is highlighted by annotation B and occurs for a range of values around $k_{\|} \approx 0.06 v_{th}/\omega_{pe}$. This well known instability is strongest at $\omega \approx \omega_{pe}$ and $k_{\perp} = 0$. Growth rates here peak at around $\gamma_c \approx 0.0027\omega_{pe}$ and are larger than those of the ADI. At higher values of $k_{\|}$ and low $k_{\perp}$ a third additional region of growth exists for late times. This region is shown by annotation C. The details of this effect and its relation to nonlinear 3-wave coupling are described in detail within section 4.4.5.

To get a more precise comparison between simulated and numerical growth rates we show these overlaid in 1D for the specific angle of $\theta = 45^o$ in figures 4.17 and 4.18 at later times. These figures are constructed from the same data as in Figure 4.16. We again see that very good agreement exists between linear growth rates computed via the dispersion solver and those measured in simulation at this angle. The standard deviation of the linear regressive fit is shown in grey. This estimate of error appears to be accurate at the anomalous Doppler resonance, with a lower error existing in the figure computed at later time.

The agreement at the Cerenkov resonance is reasonable but not exact. This may be due to one of three effects. Firstly, the growth rate in this region depends on the derivative of the distribution function. This quantity is much more sensitive to noise than the distribution function. Secondly, growth here is much more sensitive to changes in the distribution function. In Figure 4.15 it was shown that growth at the Cerenkov resonant region is not completely linear. A line fit that is performed on data which is not entirely linear will produce a much larger error. This is evident in

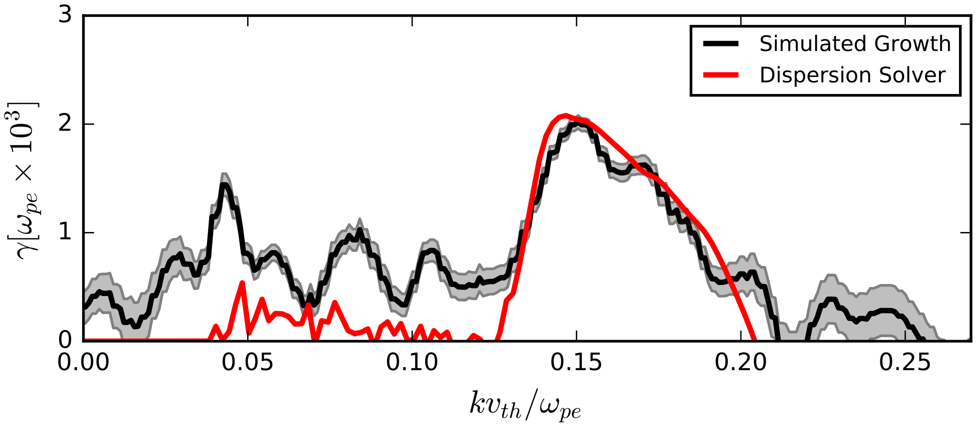

Figure 4.17: Growth rates are computed at angle $\theta = 45^o$ from the magnetic field direction for times between $t_1 = 83\tau_{ce}$ and $t_2 = 166\tau_{ce}$. Growth rates which have been measured directly from the simulated parallel electric field are shown in black, where the standard deviation of the linear regression fit is highlighted in grey. Corresponding linear growth rates which have been calculated using the dispersion solver and velocity distributions taken from simulation at these times are shown in red.

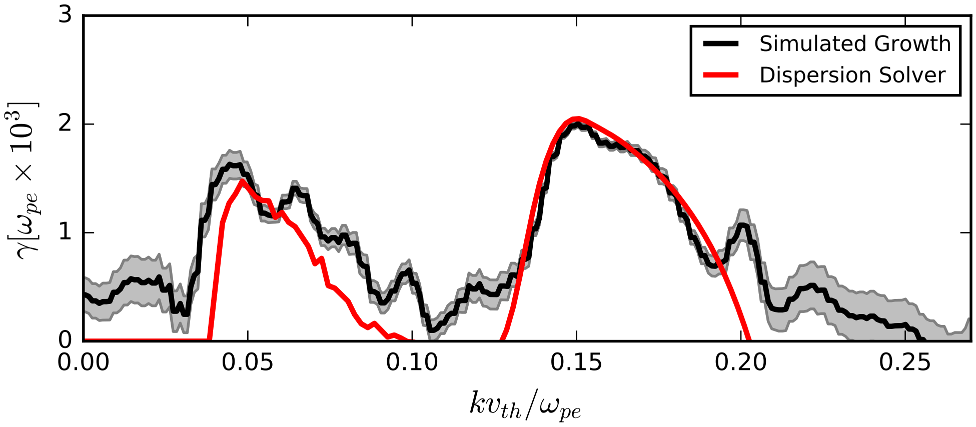

Figure 4.18: Growth rates are shown for angle $\theta = 45^o$ from the magnetic field direction for times between $t_3 = 250\tau_{ce}$ and $t_4 = 333\tau_{ce}$. Line colouring is the same as in Figure 4.17

the higher standard deviation which is also computed for this fit. Thirdly, we have not subtracted spontaneous emission in this computed fit. We discussed in Section 4.4.3 that due to the low rate of absorption for waves in this region we expect that even at times as late as these, fluctuations may not have yet saturated. This largely explains why we consistently underestimate growth at the Cerenkov resonance. The previous two effects largely explain the reduced quality of the fit. We have not yet discussed any non-linear physics. In the following section we attempt to evaluate the significance of coherent 3-wave interactions in this simulation.

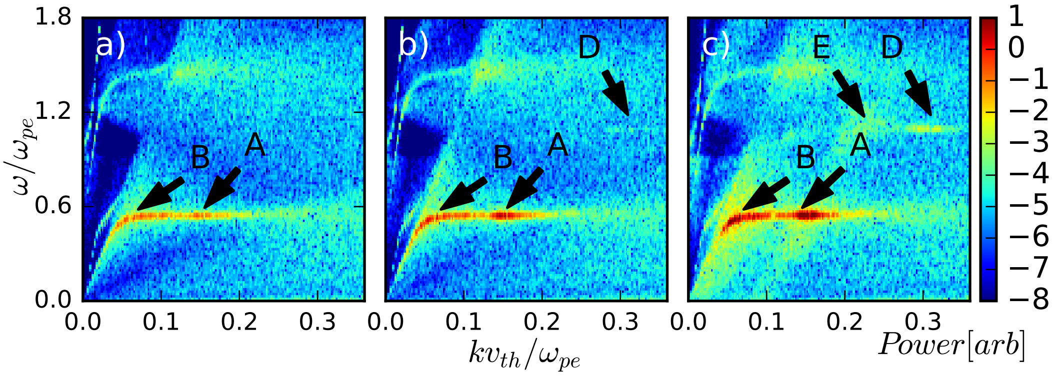

Figure 4.19: Spatiotemporal Fourier transforms of the electrostatic field at angle $\theta = 45^o$ are computed between times $83 - 166\tau_{ce}$, $250 - 333\tau_{ce}$ and $416 - 499\tau_{ce}$ in panels a), b) and c) respectively. Enhancements A-D are discussed in the main text.

4.4.5 Nonlinear Physics

At later times in the simulation we see the excitation of waves in several regions of $(\omega, \mathbf{k})$ space that would not be predicted by purely linear treatments of collective instability or spontaneous emission. In Figure 4.19 we show spatiotemporal Fourier transforms computed for successive time windows, at an angle $\theta = 45^o$ from the magnetic field direction. Several key enhancements are annotated with letters A, B, D and E. The labelling of annotations here is consistent with labelling used in previous figures in this chapter. The first two of these annotations are the anomalous Doppler and Cerenkov resonant regions which we have previously discussed. The power in waves at the the anomalous Doppler resonance (A) can be seen to rise incrementally between panels a), b) and c). Power at the Cerenkov resonance (B) primarily grows between panels b) and c). Two additional regions of excitation are also highlighted by annotations D and E. These excitations appear only once sufficient power exists within the simulation. To explain these excitations we must consider coherent wave-wave scattering.

The theory of wave-wave scattering is one of the cornerstones of weakly nonlinear plasma theory. Our understanding of this topic is primarily based on the textbooks “Nonlinear Plasma Theory” by Sagdeev and Galeev[135] and “Plasma Physics” by Cairns[136]. We begin by considering two travelling waves which are resonant with a third wave such that the conditions $\omega_1 + \omega_2 = \omega_3$ and $\mathbf{k}_1 + \mathbf{k}_2 = \mathbf{k}_3$ are satisfied. This resonance causes nonlinear coupling when the first and second waves beat together such that the sum of two frequencies and wavenumbers matches the frequency and wavenumber of a third wave. When these conditions are satisfied, energy is free to transfer between the different modes. The differential equations:

$$\frac{d\phi_1}{dt} = \frac{i}{4\omega_1}\phi_2\phi_3, \tag{4.22}$$

$$\frac{d\phi_2}{dt} = \frac{i}{4\omega_2}\phi_1\phi_3^*, \tag{4.23}$$

$$\frac{d\phi_3}{dt} = \frac{i}{4\omega_3}\phi_1\phi_2^*, \tag{4.24}$$

describe energy transfer between different modes to first order, where ϕ_j describes the complex amplitude of mode j with frequency ω_j and wavenumber $\mathbf{k}_j$. These equations show that in order for long term energy transfer to occur, there must be phase locking between the complex amplitudes ϕ_1, ϕ_2 and ϕ_3. The long term evolution and saturation of nonlinear three-wave interactions has been studied in detail by Kaup et al.[137]. We do not study the long term evolution in such detail, instead considering only cases where two source modes drive growth at their beat mode. For energy transfer to be significant in this scenario, the amplitude of the two driving waves must be large.

In panels b) and c) of Figure 4.19 it appears that waves at annotation D satisfy the relationships $2\omega_A = \omega_D$ and $2\mathbf{k}_A = \mathbf{k}_D$. The enhancement at region D only appears when the mode amplitudes at region A are large. This would suggest that the mode at $(\omega_A, \mathbf{k}_A)$ drives excitation at $(\omega_D, \mathbf{k}_D)$ through nonlinear wave-wave coupling. Similarly, an enhancement exists where modes at annotation E in panel c) satisfy the relationships $\omega_A + \omega_B = \omega_E$ and $\mathbf{k}_A + \mathbf{k}_B = \mathbf{k}_E$. These modes form a three-wave triad. In addition to the wave amplitude being large, the phases of interacting waves must lock for significant energy transfer to occur. We can examine the phase locking of these waves using higher order spectral techniques.

The bispectrum is a higher order spectrum which measures the degree of phase coupling between two waves and their matching beat wave. Bispectral techniques have been used on numerous occasions to study the nonlinear coupling and energy transfer between modes which form three-wave triads[138–142]. The bispectrum is typically applied to time series data and is defined by the expression:

$$B(\omega_1, \omega_2) = \left\langle \hat{F}(\omega_1)\hat{F}(\omega_2)\hat{F}^*(\omega_1 + \omega_2) \right\rangle. \tag{4.25}$$

Here the angular brackets show that the argument has been averaged in time and $\hat{F}(\omega)$ denotes the temporal Fourier transform of some quantity. The time averaged bispectrum provides information about the energy transfer between modes on longer timescales as short term fluctuations tend to cancel out. A detailed review of the connection between the phase direction of the bispectrum and the direction of power flow between modes was presented by Kim et al.[138]. If the coupling coefficients of the wave equation are known a priori then it is possible to determine the direction of energy flow using the bispectrum. In our figures, we only plot the absolute value of the bispectrum. This serves as an indication for the magnitude of energy transfer, but does not determine the direction of phase mixing or amplitude amplification which could otherwise be found.

We can also perform bispectral anlysis using Fourier transforms which are performed in space and time. This approach to spatiotemporal bispectral analysis has been used to study ion saturation-current in the Large Mirror Device-Upgrade[139]. Requiring that both $\mathbf{k}$ and ω now match, the equation for the bispectrum becomes:

$$B(\omega_1, \omega_2, \mathbf{k}_1, \mathbf{k}_2) = \left\langle \hat{F}(\omega_1, \mathbf{k}_1)\hat{F}(\omega_2, \mathbf{k}_2)\hat{F}^*(\omega_1 + \omega_2, \mathbf{k}_1 + \mathbf{k}_2) \right\rangle, \tag{4.26}$$

where $\hat{F}(\omega, \mathbf{k})$ now denotes the spatiotemporal Fourier transform of some quantity which is oscillating in both space and time. In practise the time averaging is performed by taking a series of temporal Fourier transforms, each with a time duration which is some fraction of the total period of interest. There is a trade-off between the frequency resolution which can be attained and the number of Fourier transforms which may be averaged across. High frequency resolution requires Fourier transforms with larger durations, which means less independent Fourier transforms may be sampled. Conversely, more samples requires shorter Fourier transforms which means lower frequency resolution. For small numbers of samples, where a large variation in mode amplitudes exists, it can be difficult to extract useful information about phase coherence from the bispectrum. In this case the signal present in the bispectrum has a greater dependence on the amplitude of the underlying modes than on the phase correlation which is present. It is more effective to instead determine phase coherence using a normalized quantity which is the bicoherence.

The bicoherence provides a quantitative measure of phase coherence between modes[140]. When modes emerge which are phase locked with additional modes satisfying the triad conditions and the bicoherence of these triads is close to unity, it is probable that the modes are interacting via nonlinear wave-wave coupling. When these modes are not coherent, and their bicoherence is low, it may be the case that they are excited by an independent means. Here we use the following definition for the bicoherence of modes $(\omega_1, \mathbf{k}_1)$ and $(\omega_2, \mathbf{k}_2)$:

$$b^2(\omega_1, \omega_2, \mathbf{k}_1, \mathbf{k}_2) = \frac{\left|B(\omega_1, \omega_2, \mathbf{k}_1, \mathbf{k}_2)\right|^2}{\left\langle \left|\hat{F}(\omega_1 + \omega_2, \mathbf{k}_1 + \mathbf{k}_2)\hat{F}(\omega_1, \mathbf{k}_1)\hat{F}(\omega_2, \mathbf{k}_2)\right|^2 \right\rangle}, \tag{4.27}$$

which follows the convention of normalizing the squared bispectrum.

One of the largest challenges posed during the bispectral analysis of simulation data is dealing with the high dimensionality of output. Equations 4.26 and 4.27 produce output which has six dimensions. As well as being computationally intractable to compute, this quantity is difficult to visualize. To avoid this we must make several reductions. Firstly, we can select only the frequencies where the strongest modes occur. We make this selection for both $\hat{F}(\omega_m(\mathbf{k}_1), \mathbf{k}_1)$ and $\hat{F}(\omega_m(\mathbf{k}_2), \mathbf{k}_2)$, where $\omega_m(\mathbf{k})$ selects the frequency with maximum amplitude at wavenumber $\mathbf{k}$. The prescription for $\hat{F}^*(\omega_m(\mathbf{k}_1) + \omega_m(\mathbf{k}_2), \mathbf{k}_1 + \mathbf{k}_2)$ is then also defined. The approach which we have devised allows for the reduction of two dimensions in the output of the spatiotemporal bispectrum. This approach has been applied to visualize phase locking during the nonlinear excitation of higher ion cyclotron harmonics during simulations of KSTAR edge localised mode crashes[143].

Selecting a single value from both of the frequency domains reduces the dimensionality of output from six to four. We can further reduce the dimensionality by applying constraints to the values of $\mathbf{k}$ which we examine. In Figure 4.20 we show several regions of importance which we restrict our analysis to. The simplest restriction which we can make is to only consider waves which are travelling in a single direction. This further reduces the dimensionality of output from four down to two, which can be plotted without loss of information. We apply this restriction to investigate the phase locking of waves travelling at 45^o from the magnetic field direction in figures 4.21 and 4.22.

Figure 4.21 shows the bispectrum of only oblique waves with wavevectors k_1 and k_2 directed at 45^o from the magnetic field direction. The bispectrum increases more rapidly than the power in the simulation. This means that the rate of power growth at the beat modes may exceed the linear growth of the pump modes. Annotations D and E correspond to the maximum absolute value of the bispectrum for only waves travelling in this direction. These locations directly correspond to the triads we suggested may be interacting when inspecting Figure 4.19. Figure 4.22 shows the bicoherence plotted for the same times and values of k_1 and k_2. The regions shaded in red show where phase locking has occured. It is necessary for both

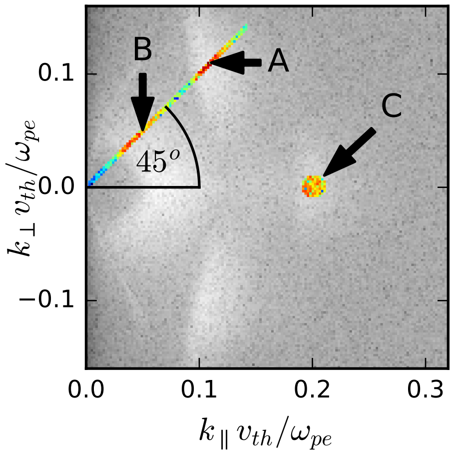

Figure 4.20: Schematic of the regions in **k**-space which we probe for resonant three-wave triads. In figures 4.19, 4.21 and 4.22 we show quantities which have been computed for angle $\theta = 45^o$ in isolation. The anomalous Doppler and Cerenkov wave-particle resonances at A and B are highlighted here and modes travelling in this direction are colourized. In figures 4.23, 4.24 and 4.25 we investigate the cause of the enhancement at region C. These modes at region C are also coloured. We do not explore in great detail the bispectral properties of the majority of modes which are shaded in grey.

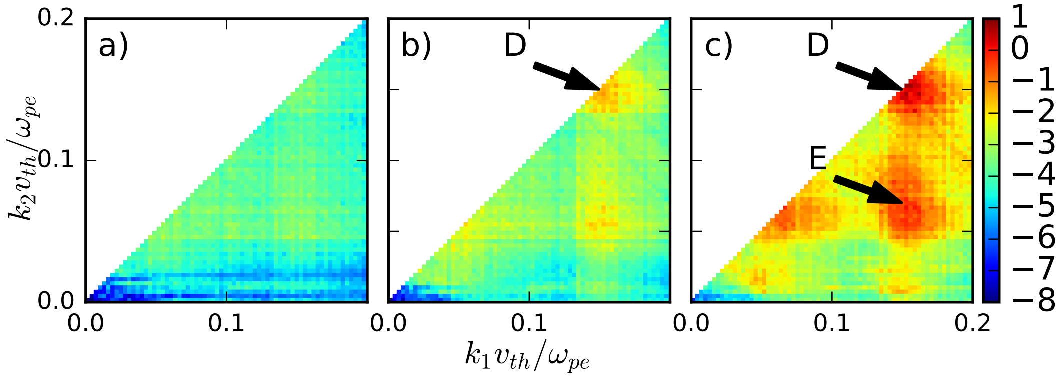

Figure 4.21: Magnitude of the spatiotemporal bispectrum of the electrostatic field is computed for only modes travelling in the $\theta = 45^o$ direction with wavenumbers k_1 and k_2. Panels a), b) and c) correspond to the same panels which are shown in Figure 4.19 at times $83 - 166\tau_{ce}$, $250 - 333\tau_{ce}$ and $416 - 499\tau_{ce}$. For each panel 100 temporal Fourier transforms are performed with duration $16.6\tau_{ce}$ and equidistant spacing in time.

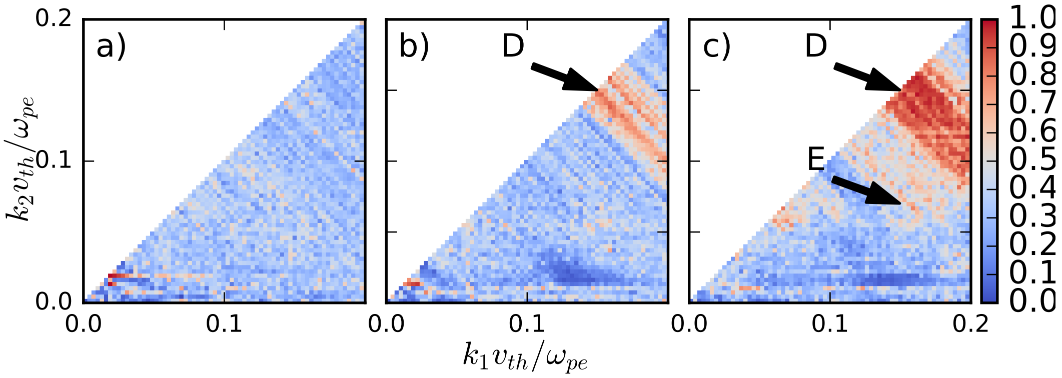

Figure 4.22: Spatiotemporal bicoherence is computed for the same parameters and data which is shown in Figure 4.21. Regions in red show strong mode coherence while regions in blue show modes which are not phase locked. Diagonal red features indicate that a spread of pump modes are phase locked with a single beat mode with the sum of $k_1 + k_2$ a constant.

the absolute value of the bispectrum between modes with wavevector k_1 and k_2 to be large as well as these modes to be phase locked for significant energy transfer to occur. Both these conditions are satisfied for the enhancements annotated by D and E. This is strong evidence that the enhancement at $(\omega_D, \mathbf{k}_D)$ is powered by modes at $(\omega_A, \mathbf{k}_A)$ interacting nonlinearly and the enhancement at $(\omega_E, \mathbf{k}_B)$ is powered by a three-wave triad with pump modes at $(\omega_A, \mathbf{k}_A)$ and $(\omega_B, \mathbf{k}_B)$.

In Figure 4.23 we show spatiotemporal Fourier transforms which are taken in the $\theta = 0^o$ direction. This choice was made to highlight the enhancement at region C. Unlike the previous enhancements which we have explored, no triads can be found using only pump modes travelling in the $\theta = 0^o$ direction to support this enhancement. The pairs of coherent waves with both frequencies and wavenumbers which add up that we have discussed so far have all produced beat waves at regions in (ω, k) space which are damped. It is also possible for the beat frequency and beat wavevector to coincide with a solution to the dispersion relation. If this condition is met, it is possible for the beat power to build up to much higher levels.

Given an adequate model for the dispersion relation $\omega(\mathbf{k})$, we can predict the possible values of $(\omega, \mathbf{k})$ which support the frequency matching condition for three-wave triads involving fundamental modes. We proceed by considering a cold plasma model and assuming that $\mathbf{k}$ is large. Although a kinetic treatment is required to compute the exact frequencies, a cold plasma model is easy to work with and should provide a good first approximation. The resonance frequency of the lower

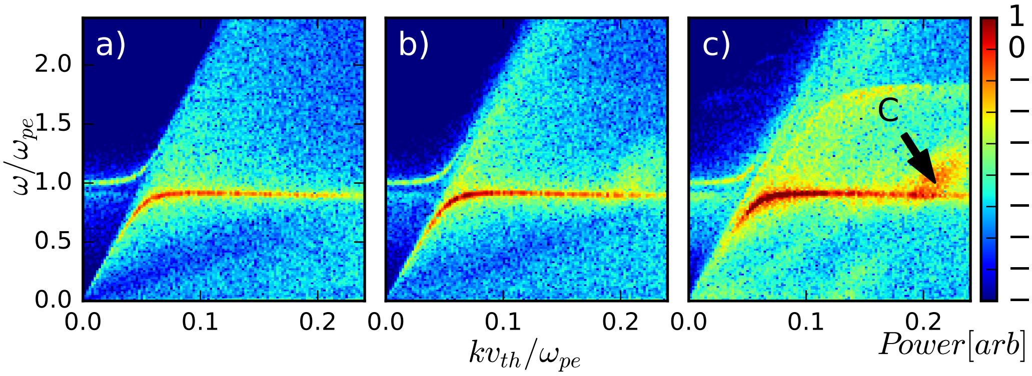

Figure 4.23: Spatiotemporal Fourier transforms of the electrostatic field at angle $\theta = 0^o$ are computed between times $83 - 166\tau_{ce}$, $250 - 333\tau_{ce}$ and $416 - 499\tau_{ce}$ in panels a), b) and c) respectively. Enhancement C is discussed in the main text.

bulk mode travelling in direction θ from the magnetic field is then defined by:

$$\omega_L(\theta)^2 = \frac{1}{2}\omega_h^2 \left(1 - \sqrt{1 - \frac{4\Omega_{ce}^2\omega_{pe}^2 \cos^2\theta}{\omega_h^4}}\right), \tag{4.28}$$

where the upper hybrid frequency is $\omega_h^2 = \omega_{pe}^2 + \Omega_{ce}^2$. The enhancement denoted by letter C occurs at angle $\theta = 0^o$. For this direction and excluding thermal terms the dominant mode occurs at $\omega = \omega_{pe}$. The constraint $\omega_L(\theta_1) + \omega_L(\theta_2) = \omega_{pe}$ is then required for the matching condition to be satisfied. This allows us to calculate the second angle θ_2 as a function of the first:

$$\theta_2(\theta_1) = \cos^{-1}\left[\frac{\omega_h^2}{2\omega_{ce}\omega_{pe}}\sqrt{1 - \left(1 - \frac{2(\omega_{pe} - \omega_L(\theta_1))^2}{\omega_h^2}\right)^2}\right]. \tag{4.29}$$

If we select a specific coordinate in **k**-space for the beat mode, we can then calculate a curve where we may expect the frequency matching condition to be satisfied. The parallel and perpendicular constraints for coordinate $(0.2, 0.0)$ are as follows:

$$\begin{pmatrix} k_1 \cos\theta_1 + k_2 \cos\theta_2(\theta_1) \\ k_1 \sin\theta_1 - k_2 \sin\theta_2(\theta_1) \end{pmatrix} = \begin{pmatrix} 0.2 \\ 0.0 \end{pmatrix}. \tag{4.30}$$

This gives us a method to estimate the positions in **k**-space where we expect phase locking to occur. The black semicircle overlaid in figures 4.24 and 4.25 traces the solution of these equations.

In figures 4.24 and 4.25 we have fixed $\mathbf{k}_3 = \mathbf{k}_1 + \mathbf{k}_2$ to be constant at the values highlighted by the colourized circle around region C in Figure 4.20 which has

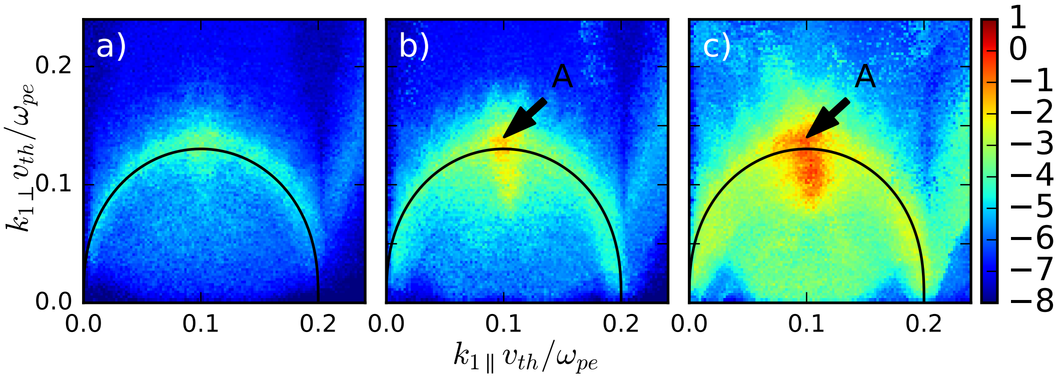

Figure 4.24: Spatiotemporal bispectrum is plotted as a function of $(k_{1\parallel}, k_{1\perp})$. The sum of wavevectors $\mathbf{k}_1+\mathbf{k}_2$ is held fixed at $\mathbf{k}_3 = (0.2\omega_{pe}/v_{th}, 0.0)$. In consistancy with figures 4.21 and 4.22 100 temporal Fourier transforms are performed with duration $16.6\tau_{ce}$ and equidistant spacing.

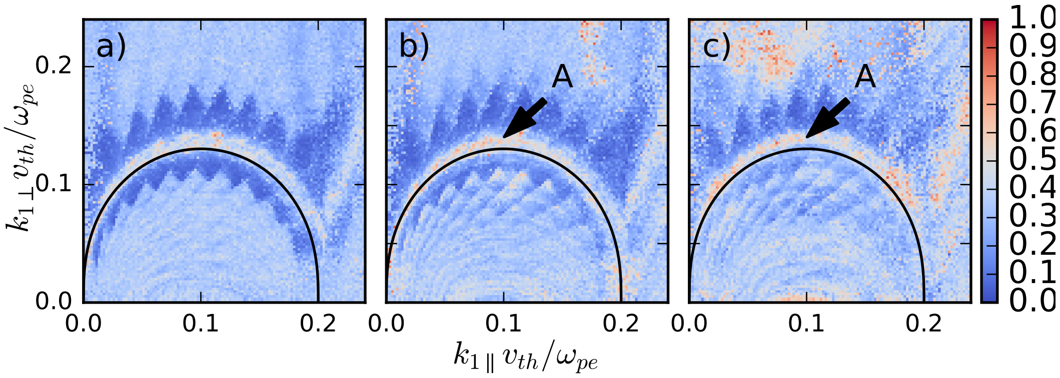

Figure 4.25: Spatiotemporal bicoherence corresponding to bispectrum computed in Figure 4.24. Regions in red show strong mode coherence while regions in blue show modes which are not phase locked. The black line traces the solution to Equation 4.30 which we have calculated.

the centre at $\mathbf{k} = (0.2, 0.0)$ and a radius of $R = 0.007$. The variable $\mathbf{k}_1$ is then varied across both $k_{\|}$ and $k_{\perp}$. The value of $\mathbf{k}_2$ is then constrained by the matching condition. This means that we can visualize the regions in $(k_{\|}, k_{\perp})$ where phase locking occurs as a function of just $\mathbf{k}_1$. The same methods and parameters which were used to compute the bispectrum and bicoherence in figures 4.21 and 4.22 are used to produce figures 4.24 and 4.25. When multiple points land in the same pixel that is being displayed, we average the bispectrum and bicoherence for these pixels.

The bispectrum which is shown in Figure 4.24 shows that the regions which have the highest potential for energy transfer occur along the black line which we would expect the frequency matching condition to occur along. A significant region with high potential for energy transfer also occurs around the anomalous Doppler resonant region marked A in panels b) and c). This region extends significantly beyond the confines of the black line, where bicoherence is large. We can use this to explain the significant excitation of modes with $\omega > \omega_{pe}$ which are visible on panel c) of Figure 4.22.

Figure 4.24 shows the bicoherence which has been computed for the same parameters as Figure 4.23. Regions which are dark blue are actively forced out of phase coherence by a small mismatch condition between their dominant frequencies. As these regions are actively driven out of phase they have a bicoherence which is lower than what would be expected from purely stochastic phases. The majority of modes shaded in light blue have phases which are well described as being stochastic. The pattern around the black curve arises because of the discretization of frequency. The shading of the “cells” in this pattern, with boundaries converging to the points $(0.0, 0.0)$ and $(0.2, 0.0)$, is governed by the dominant frequency mismatch for wavesnumbers k_1 and k_2. We can alter the granularity of this mismatch pattern by modifying the number of frequency bins in the Fourier transform. For regions in $\mathbf{k}$-space where the frequency mismatch approaches zero the bicoherence is high. The semicircle of high bicoherence computed from simulation shows excellent agreement with the black curve which we have predicted by considering only the cold plasma dispersion relation.

Chapter 5

Summary

In this thesis we began by describing some of the methodology which is required to analyse simulations of waves in particle-in-cell codes. We demonstrated the techniques necessary to accurately resolve linear physics and instability. We demonstrated that linear theory is a powerful tool to describe the early stage evolution of simulations. We also showcased high resolution agreement between simple dispersion models and simulations performed using *EPOCH*.

In the third chapter of this thesis we outlined the construction of two variants of a code capable of solving linear dispersion relations for plasmas characterized by arbitrary gyrotropic velocity distributions. A non-relativistic and fully relativistic variant of the code were shown to be a viable approach to accurately calculate linear physics for electrostatic and electromagnetic waves travelling in homogeneous mediums. Linear solvers of this kind are, surprisingly, a very recent advancement in the tools available for studying velocity space instability. The non-relativistic variant of the code is also, to the best of our knowledge, the first of its kind to be released publicly. We showed that these codes effectively calculated a range of velocity space instabilities including two-stream instability, kinetic electron firehose instability, ion cyclotron emission and in the case of the relativistic solver, electron cyclotron maser emission. The ability to perform such calculations rapidly saves both high performance computing resources and researcher time when investigating instability driven by non-thermal velocity distributions. These codes are useful because they allow informed predictions to be made, without detailed foreknowledge of the correct analytic prescriptions, regarding the linear evolution of unstable waves produced in fully kinetic particle-in-cell simulations of highly non-thermal particle distributions in magnetized plasmas. These calculations may be performed in a very reasonable and human interactable time period ranging between a few minutes to a few tens of minutes on a single desktop computer.

In the fourth chapter we showcased 2D3V simulations of the anomalous Doppler instability in fusion relevant plasma. We began by investigating the linear descriptions which have previously been applied to describe the anomalous Doppler instability. Armed with a general means to directly compute linear growth rates for magnetized plasmas characterized by arbitrary gyrotropic velocity distributions, we were able to highlight the approaches which were most effective for computing growth of the ADI. We demonstrated that the wave-wave variant of the ADI was not suited to describing plasmas which were not well modelled by cold beams. We showed that in most cases, with adequate corrections, the previously employed linear calculations could correctly compute growth of the ADI. The 2D3V simulations that we performed demonstrated that it was possible for the ADI to self consistently drive a positive slope in the parallel electron velocity distribution. We showed that the presence of this positive slope excited waves in a separate region of frequency and wavevector space to that excited by the ADI. We showed that the simulated linear and quasilinear stages of instability demonstrated strong agreement with the linear solver which we have constructed. We also showed that the addition of a second simulated spatial dimension was necessary to capture nonlinear three-wave coupling which can be driven by the ADI. The location of this three-wave triad, which has not previously been explored, is consistent with what would be predicted by the wave matching condition and a cold plasma model. This was demonstrated using detailed bispectral analysis and novel visualization techniques which are necessary in high dimensions.

5.1 Future Work

Future work related to the topics which we have covered may move forward in several directions. We note that the linear solver which we have constructed may be modified by simple means to account for several more complex physical effects. Following the work demonstrated in [131–134], it is possible to add a source fluctuation term to the wave Equation 3.38. Solving the inhomogeneous wave equation for arbitrary gyrotropic plasmas would allow for a full equilibrium spectrum of excitations to be predicted, potentially showing agreement with the background fluctuation spectrum produced in PIC simulation. It may also be possible to add in terms which model non-linear effects such three-wave triads to the solver, providing that a fixed wave amplitude is also prescribed. The growth rate solver which we have constructed may also be applied to study a wide range of physics problems involving velocity-space instability.

The fully kinetic self consistent simulations of the ADI which we performed do not directly address experimental data. Correlations have been shown between microwave bursts and supposed anomalous Doppler unstable runaway electrons[104]. Microwave bursts observed in tokamak devices tend to be in a range of frequencies which exceed those observed during the ADI[23]. The frequencies which are observed are instead closer to the second cyclotron harmonic. We briefly considered the electron cyclotron maser instability as a potential candidate for driving this emission. However, it does not appear possible for the necessary perpendicular population inversion required to stimulate the electron cyclotron maser instability to occur. Instead, it may be possible to model the effects which the diffusion in phase space caused by the ADI has on spontaneous emission and absorption at the second cyclotron harmonic. This study would involve calculating the rate of absorption and spontaneous emission at the second cyclotron harmonic for velocity distributions which are expected during different phases of the ADI.

Bibliography

[1] K. G. McClements, J. O. Allen, S. C. Chapman, R. O. Dendy, S. W. A. Irvine, O. Marshall, D. Robb, M. Turnyanskiy, and R. G. L. Vann, "Particle acceleration during merging-compression plasma start-up in the mega amp spherical tokamak," *Plasma Physics and Controlled Fusion*, vol. 60, no. 2, p. 025013, 2018.

[2] E. G. Evstatiev, R. A. Nebel, L. Chacn, J. Park, and G. Lapenta, "Space charge neutralization in inertial electrostatic confinement plasmas," *Physics of Plasmas*, vol. 14, no. 4, p. 042701, 2007.

[3] J. D. Lawson, "Some criteria for a power producing thermonuclear reactor," *Proceedings of the Physical Society. Section B*, vol. 70, no. 1, p. 6, 1957.

[4] R. S. Craxton, K. S. Anderson, T. R. Boehly, V. N. Goncharov, D. R. Harding, J. P. Knauer, R. L. McCrory, P. W. McKenty, D. D. Meyerhofer, J. F. Myatt, A. J. Schmitt, J. D. Sethian, R. W. Short, S. Skupsky, W. Theobald, W. L. Kruer, K. Tanaka, R. Betti, T. J. B. Collins, J. A. Delettrez, S. X. Hu, J. A. Marozas, A. V. Maximov, D. T. Michel, P. B. Radha, S. P. Regan, T. C. Sangster, W. Seka, A. A. Solodov, J. M. Soures, C. Stoeckl, and J. D. Zuegel, "Direct-drive inertial confinement fusion: A review," *Physics of Plasmas*, vol. 22, no. 11, p. 110501, 2015.

[5] T. C. Simonen, "Three game changing discoveries: A simpler fusion concept?," vol. 35, 09 2015.

[6] R. Post, "Summary of ucrl pyrotron (mirror machine) program," 10 1959.

[7] A. Beklemishev, A. Anikeev, V. Astrelin, P. Bagryansky, A. , V. , D. Gavrilenko, A. Ivanov, I. Ivanov, M. , K. Igor, S. Polosatkin, V. Postupaev, S. Sinitsky, A. Shoshin, I. , and Y. , "Novosibirsk project of gas-dynamic multiple-mirror trap," vol. 63, pp. 46–51, 05 2013.

[8] A. A. Ivanov and V. V. Prikhodko, “Gas-dynamic trap: an overview of the concept and experimental results,” *Plasma Physics and Controlled Fusion*, vol. 55, no. 6, p. 063001, 2013.

[9] M. Nagel, C. Dhard, H. Bau, H.-S. Bosch, U. Meyer, S. Raatz, K. Risse, and T. Rummel, “Cryogenic commissioning, cool down and first magnet operation of wendelstein 7-x,” *IOP Conference Series: Materials Science and Engineering*, vol. 171, no. 1, p. 012050, 2017.

[10] C. Beidler, G. Grieger, F. Herrnegger, E. Harmeyer, J. Kisslinger, W. Lotz, H. Maassberg, P. Merkel, J. Nhrenberg, F. Rau, J. Sapper, F. Sardei, R. Scardovelli, A. Schlter, and H. Wobig, “Physics and engineering design for wendelstein VII-X,” vol. 17, pp. 148–168, 01 1990.

[11] E. A. Lazarus, M. S. Chu, J. R. Ferron, F. J. Helton, J. T. Hogan, A. G. Kellman, L. L. Lao, J. B. Lister, T. H. Osborne, R. Snider, E. J. Strait, T. S. Taylor, and A. D. Turnbull, “Higher beta at higher elongation in the diiid tokamak,” *Physics of Fluids B: Plasma Physics*, vol. 3, no. 8, pp. 2220–2229, 1991.

[12] J. Hu, G. Zuo, J. Li, N. Luo, L. Zakharov, L. Zhang, W. Zhang, and P. Xu, “Investigation of lithium as plasma facing materials on ht-7,” *Fusion Engineering and Design*, vol. 85, no. 6, pp. 930 – 934, 2010. Proceedings of the 1st International Workshop on Lithium Applications for the Boundary Control in Fusion Devices.

[13] B. J. Green, I. I. Team, and P. Teams, “Iter: burning plasma physics experiment,” *Plasma Physics and Controlled Fusion*, vol. 45, no. 5, p. 687, 2003.

[14] Y. Shimomura, R. Aymar, V. Chuyanov, M. Huguet, H. Matsumoto, T. Mizoguchi, Y. Murakami, A. Polevoi, M. Shimada, I. J. C. Team, and I. H. Teams, “ITER-FEAT operation,” *Nuclear Fusion*, vol. 41, no. 3, p. 309, 2001.

[15] I. Chapman, W. Cooper, J. Graves, M. Gryaznevich, R. Hastie, T. Hender, D. Howell, M.-D. Hua, G. Huysmans, D. Keeling, Y. Liu, H. Meyer, C. Michael, S. Pinches, S. Saarelma, S. Sabbagh, and the MAST Team, “Macroscopic stability of high mast plasmas,” *Nuclear Fusion*, vol. 51, no. 7, p. 073040, 2011.

[16] A. Costley, J. Hugill, and P. Buxton, “On the power and size of tokamak fusion pilot plants and reactors,” *Nuclear Fusion*, vol. 55, no. 3, p. 033001, 2015.

[17] Y.-K. M. Peng, P. J. Fogarty, T. W. Burgess, D. J. Strickler, B. E. Nelson, J. Tsai, C. A. Neumeyer, R. Bell, C. Kessel, J. Menard, D. Gates, B. LeBlanc, D. Mikkelsen, E. Fredrickson, L. Grisham, J. Schmidt, P. Rutherford, S. Sabbagh, A. Field, A. Sykes, I. Cook, O. Mitarai, and Y. Takase, "A component test facility based on the spherical tokamak," *Plasma Physics and Controlled Fusion*, vol. 47, no. 12B, p. B263, 2005.

[18] F. Wagner, G. Becker, K. Behringer, D. Campbell, A. Eberhagen, W. Engelhardt, G. Fumann, O. Gehre, J. Gernhardt, G. von Gierke, G. Haas, and M. Huang, "Regime of improved confinement and high beta in neutral-beam-heated divertor discharges of the ASDEX tokamak," vol. 49, pp. 1408–1412, 11 1982.

[19] A. Team, "The H-mode of ASDEX," *Nuclear Fusion*, vol. 29, no. 11, p. 1959, 1989.

[20] T. Eich, A. Leonard, R. Pitts, W. Fundamenski, R. Goldston, T. Gray, A. Herrmann, A. Kirk, A. Kallenbach, O. Kardaun, A. Kukushkin, B. LaBombard, R. Maingi, M. Makowski, A. Scarabosio, B. Sieglin, J. Terry, A. Thornton, A. U. Team, and J. E. Contributors, "Scaling of the tokamak near the scrape-off layer H-mode power width and implications for ITER," *Nuclear Fusion*, vol. 53, no. 9, p. 093031, 2013.

[21] H. Zohm, "Edge localized modes (ELMs)," *Plasma Physics and Controlled Fusion*, vol. 38, no. 2, p. 105, 1996.

[22] D. Hill, "A review of elms in divertor tokamaks," *Journal of Nuclear Materials*, vol. 241-243, pp. 182 – 198, 1997.

[23] S. J. Freethy, K. G. McClements, S. C. Chapman, R. O. Dendy, W. N. Lai, S. J. P. Pamela, V. F. Shevchenko, and R. G. L. Vann, "Electron Kinetics Inferred from Observations of Microwave Bursts During Edge Localized Modes in the Mega-Amp Spherical Tokamak," *Physical Review Letters*, vol. 114, p. 125004, Mar. 2015.

[24] K. G. McClements and M. R. Turnyanskiy, "Energetic particles in laboratory, space and astrophysical plasmas," *Plasma Physics and Controlled Fusion*, vol. 59, no. 1, p. 014012, 2017.

[25] W. Suttrop, A. Kirk, V. Bobkov, M. Cavedon, M. Dunne, R. McDermott, H. Meyer, R. Nazikian, C. Paz-Soldan, D. Ryan, E. Viezzer, M. Willensdorfer,

T. A. Upgrade, and M. Teams, “Experimental conditions to suppress edge localised modes by magnetic perturbations in the ASDEX upgrade tokamak,” *Nuclear Fusion*, vol. 58, no. 9, p. 096031, 2018.

[26] O. Gruber, K. Lackner, G. Pautasso, U. Seidel, and B. Streibl, “Vertical displacement events and halo currents,” *Plasma Physics and Controlled Fusion*, vol. 35, no. SB, p. B191, 1993.

[27] S. Putvinski, P. Barabaschi, N. Fujisawa, N. Putvinskaya, M. N. Rosenbluth, and J. Wesley, “Halo current, runaway electrons and disruption mitigation in ITER,” *Plasma Physics and Controlled Fusion*, vol. 39, no. 12B, p. B157, 1997.

[28] J. Roth, E. Tsitrone, A. Loarte, T. Loarer, G. Counsell, R. Neu, V. Philipps, S. Brezinsek, M. Lehnen, P. Coad, C. Grisolia, K. Schmid, K. Krieger, A. Kallenbach, B. Lipschultz, R. Doerner, R. Causey, V. Alimov, W. Shu, O. Ogorodnikova, A. Kirschner, G. Federici, and A. Kukushkin, “Recent analysis of key plasma wall interactions issues for ITER,” *Journal of Nuclear Materials*, vol. 390-391, pp. 1 – 9, 2009. Proceedings of the 18th International Conference on Plasma-Surface Interactions in Controlled Fusion Device.

[29] F. C. Schuller, “Disruptions in tokamaks,” *Plasma Physics and Controlled Fusion*, vol. 37, no. 11A, p. A135, 1995.

[30] R. Fitzpatrick, “A simple ideal magnetohydrodynamical model of vertical disruption events in tokamaks,” *Physics of Plasmas*, vol. 16, no. 1, p. 012506, 2009.

[31] P. C. ITER Physics Expert Group on Disruptions, MHD, and I. P. B. Editors, “Chapter3: Mhd stability, operational limits and disruptions,” *Nuclear Fusion*, vol. 39, no. 12, p. 2251, 1999.

[32] A. Alekseev, A. Belov, E. A Azizov, V. Amosov, I. N Makashin, S. Mirnov, I. B Semenov, S. Tugarinov, and A. P Tchernobai, “Studies of fast penetration of impurities into the core plasma during the disruption at t-11m,” 09 2018.

[33] E. M. Hollmann, P. B. Aleynikov, T. Flp, D. A. Humphreys, V. A. Izzo, M. Lehnen, V. E. Lukash, G. Papp, G. Pautasso, F. Saint-Laurent, and J. A. Snipes, “Status of research toward the iter disruption mitigation system,” *Physics of Plasmas*, vol. 22, no. 2, p. 021802, 2015.

[34] Y. Li, J. Sun, Y. Zhang, C. Sang, N. Wu, and D. Wang, “Simulation of runaway electron generation and diffusion during major disruptions in the hl-2a tokamak,” *Fusion Engineering and Design*, vol. 89, no. 7, pp. 1019 – 1023, 2014. Proceedings of the 11th International Symposium on Fusion Nuclear Technology-11 (ISFNT-11) Barcelona, Spain, 15-20 September, 2013.

[35] H. Dreicer, “Electron and ion runaway in a fully ionized gas. I,” *Phys. Rev.*, vol. 115, pp. 238–249, Jul 1959.

[36] H. Dreicer, “Electron and ion runaway in a fully ionized gas. II,” *Phys. Rev.*, vol. 117, pp. 329–342, Jan 1960.

[37] M. Rosenbluth and S. Putvinski, “Theory for avalanche of runaway electrons in tokamaks,” *Nuclear Fusion*, vol. 37, no. 10, p. 1355, 1997.

[38] A. H. Boozer, “Theory of runaway electrons in ITER: Equations, important parameters, and implications for mitigation,” *Physics of Plasmas*, vol. 22, no. 3, p. 032504, 2015.

[39] G. Pautasso, Y. Zhang, B. Reiter, L. Giannone, O. Gruber, A. Herrmann, O. Kardaun, K. Khayrutdinov, V. Lukash, M. Maraschek, A. Mlynek, Y. Nakamura, W. Schneider, G. Sias, M. Sugihara, and the ASDEX Upgrade Team, “Contribution of ASDEX upgrade to disruption studies for ITER,” *Nuclear Fusion*, vol. 51, no. 10, p. 103009, 2011.

[40] V. Sizyuk and A. Hassanein, “Self-consistent analysis of the effect of runaway electrons on plasma facing components in ITER,” *Nuclear Fusion*, vol. 49, no. 9, p. 095003, 2009.

[41] H. R. Wilson, J. W. Connor, A. R. Field, S. J. Fielding, R. L. Miller, L. L. Lao, J. R. Ferron, and A. D. Turnbull, “Ideal magnetohydrodynamic stability of the tokamak high-confinement-mode edge region,” *Physics of Plasmas*, vol. 6, no. 5, pp. 1925–1934, 1999.

[42] P. K. Browning, A. Stanier, G. Ashworth, K. G. McClements, and V. S. Lukin, “Self-organization during spherical torus formation by flux rope merging in the mega ampere spherical tokamak,” *Plasma Physics and Controlled Fusion*, vol. 56, no. 6, p. 064009, 2014.

[43] A. Glasser, C. R Sovinec, R. A Nebel, T. Gianakon, S. J Plimpton, M. S Chu, D. Schnack, and t. NIMROD Team, “The NIMROD code: A new approach to numerical plasma physics,” vol. 41, p. A747, 01 1999.

[44] V. Lukin, A. H. Glasser, W. Lowrie, and E. Meier, “HiFi – Adaptive, Implicit, High Order Finite Element Code for General Multi-Fluid Applications.,” in *AAS/Solar Physics Division Meeting #40*, vol. 40 of *AAS/Solar Physics Division Meeting*, p. 835, May 2009.

[45] H. R. Wilson, P. B. Snyder, G. T. A. Huysmans, and R. L. Miller, “Numerical studies of edge localized instabilities in tokamaks,” *Physics of Plasmas*, vol. 9, no. 4, pp. 1277–1286, 2002.

[46] J. Reusch, J. Anderson, and Y. Tsidulko, “Full particle orbit tracing with the rio code in the presence of broad-spectrum mhd activity in a reversed-field pinch,” *Nuclear Fusion*, vol. 54, no. 10, p. 104007, 2014.

[47] I. Gamba, J. Haack, C. Hauck, and J. Hu, “A fast spectral method for the boltzmann collision operator with general collision kernels,” *SIAM Journal on Scientific Computing*, vol. 39, no. 4, pp. B658–B674, 2017.

[48] P. L. Bhatnagar, E. P. Gross, and M. Krook, “A model for collision processes in gases. I. small amplitude processes in charged and neutral one-component systems,” *Phys. Rev.*, vol. 94, pp. 511–525, May 1954.

[49] L. Pareschi, G. Russo, and G. Toscani, “Fast spectral methods for the Fokker-Planck-Landau collision operator,” *Journal of Computational Physics*, vol. 165, no. 1, pp. 216 – 236, 2000.

[50] E. A. Belli and J. Candy, “An eulerian method for the solution of the multi-species drift-kinetic equation,” *Plasma Physics and Controlled Fusion*, vol. 51, no. 7, p. 075018, 2009.

[51] A. J. Brizard and T. S. Hahm, “Foundations of nonlinear gyrokinetic theory,” *Rev. Mod. Phys.*, vol. 79, pp. 421–468, Apr 2007.

[52] I. L. Klimontovich, “On the Method of “Second Quantization” in Phase Space,” *Soviet Journal of Experimental and Theoretical Physics*, vol. 6, p. 753, 1958.

[53] T. D. Arber, K. Bennett, C. S. Brady, A. Lawrence-Douglas, M. G. Ramsay, N. J. Sircombe, P. Gillies, R. G. Evans, H. Schmitz, A. R. Bell, and C. P. Ridgers, “Contemporary particle-in-cell approach to laser-plasma modelling,” *Plasma Physics and Controlled Fusion*, vol. 57, no. 11, p. 113001, 2015.

[54] K. Yee, “Numerical solution of initial boundary value problems involving maxwell’s equations in isotropic media,” *IEEE Transactions on Antennas and Propagation*, vol. 14, pp. 302–307, May 1966.

[55] R. Courant, K. Friedrichs, and H. Lewy, “Über die partiellen differenzengleichungen der mathematischen physik,” *Mathematische Annalen*, vol. 100, pp. 32–74, Dec 1928.

[56] J. Boris, “Acceleration calculation from a scalar potential.,” 1 1970.

[57] T. Esirkepov, “Exact charge conservation scheme for particle-in-cell simulation with an arbitrary form-factor,” *Computer Physics Communications*, vol. 135, no. 2, pp. 144 – 153, 2001.

[58] R. B. Blackman and J. W. Tukey, *The measurement of power spectra.* Dover Publications Inc., 1958.

[59] J. R. Pierce, “Possible fluctuations in electron streams due to ions,” *Journal of Applied Physics*, vol. 19, p. 231, 1948.

[60] A. V. Haeff, “Space-charge wave amplification effects,” *Phys. Rev.*, vol. 74, p. 1532, 1948.

[61] V. A. Bailey, “Spontaneous waves in discharge tubes and in the solar atmosphere,” *Nature*, vol. 16, p. 599, 1948.

[62] J. R. Pierce, “Increasing space-charge waves,” *Journal of Applied Physics*, vol. 20, no. 11, pp. 1060–1066, 1949.

[63] G. Comer, P. Peter, and N. Andersson, “Cosmological two-stream instability,” *Physics Letters B*, vol. 715, no. 4, pp. 289 – 292, 2012.

[64] M. E. Dieckmann, B. Eliasson, P. K. Shukla, N. J. Sircombe, and R. O. Dendy, “Two-stream instability in collisionless shocks and foreshock,” *Plasma Physics and Controlled Fusion*, vol. 48, no. 12B, p. B303, 2006.

[65] P. Yadav, D. N. Gupta, and K. Avinash, “Relativistic electron-beam assisted growth of oscillating two-stream instability of a plasma wave,” *Physics of Plasmas*, vol. 24, no. 6, p. 062107, 2017.

[66] L. D. Landau, “On the vibrations of the electronic plasma,” *J. Phys.(USSR)*, vol. 10, pp. 25–34, 1946.

[67] R. O. Dendy, *Plasma dynamics.* Oxford England New York: Clarendon Press Oxford University Press, 1990.

[68] J. E. Drummond, "Basic microwave properties of hot magnetoplasmas," *Phys. Rev.*, vol. 110, pp. 293–306, Apr 1958.

[69] T. H. Stix, *Waves in Plasmas.* American Institute of Physics, 1992.

[70] K. Atkinson, *An introduction to numerical analysis.* New York: Wiley, 1989.

[71] J. A. Nelder and R. Mead, "A simplex method for function minimization," *The Computer Journal*, vol. 7, no. 4, pp. 308–313, 1965.

[72] B. D. Fried and S. D. Conte, *The Plasma Dispersion Function.* 1961.

[73] H. Xie and Y. Xiao, "PDRK: A general kinetic dispersion relation solver for magnetized plasma," *Plasma Science and Technology*, vol. 18, pp. 97–107, feb 2016.

[74] P. Astfalk and F. Jenko, "Leopard: A grid-based dispersion relation solver for arbitrary gyrotropic distributions," *Journal of Geophysical Research: Space Physics*, vol. 122, no. 1, pp. 89–101, 2016.

[75] P. Hellinger, P. M. Trávníek, V. K. Decyk, and D. Schriver, "Oblique electron fire hose instability: Particle-in-cell simulations," *Journal of Geophysical Research: Space Physics*, vol. 119, no. 1, pp. 59–68, 2013.

[76] J. V. Hollweg and H. J. Vlk, "New plasma instabilities in the solar wind," *Journal of Geophysical Research (1896-1977)*, vol. 75, no. 28, pp. 5297–5309, 1970.

[77] J. W. S. Cook, R. O. Dendy, and S. C. Chapman, "Particle-in-cell simulations of the magnetoacoustic cyclotron instability of fusion-born alpha-particles in tokamak plasmas," *Plasma Physics and Controlled Fusion*, vol. 55, no. 6, p. 065003, 2013.

[78] L. Carbajal, R. O. Dendy, S. C. Chapman, and J. W. S. Cook, "Linear and nonlinear physics of the magnetoacoustic cyclotron instability of fusion-born ions in relation to ion cyclotron emission," *Physics of Plasmas*, vol. 21, no. 1, p. 012106, 2014.

[79] J. W. S. Cook, R. O. Dendy, and S. C. Chapman, "Stimulated emission of fast alfvén waves within magnetically confined fusion plasmas," *Phys. Rev. Lett.*, vol. 118, p. 185001, May 2017.

[80] R. Dendy and K. McClements, "Ion cyclotron wave emission at the quasi-perpendicular bow shock," *Journal of Geophysical Research*, vol. 98, 9 1993.

[81] R. O. Dendy, C. N. Lashmore-Davies, K. G. McClements, and G. A. Cottrell, "The excitation of obliquely propagating fast alfvn waves at fusion ion cyclotron harmonics," *Physics of Plasmas*, vol. 1, no. 6, pp. 1918–1928, 1994.

[82] E. Jones, T. Oliphant, P. Peterson, *et al.*, "SciPy: Open source scientific tools for Python," 2001–.

[83] S. W. A. Irvine, "Kinetic dispersion solver." `https://github.com/SamuelIrvine/Kinetic-Dispersion-Solver`, 2016.

[84] W. Research, "Mathematica 10.," 2015.

[85] E. G. Harris, "Plasma instabilities associated with anisotropic velocity distributions," *Journal of Nuclear Energy*, vol. 2, pp. 138–145, Jan. 1961.

[86] D. B. Melrose, "Coherent gyromagentic emission as a radiation mechanism," *Australian Journal of Physics*, vol. 26, p. 229, Apr. 1973.

[87] D. B. Melrose, "An interpretation of Jupiter's decametric radiation and the terrestrial kilometric radiation as direct amplified gyroemission," *apj*, vol. 207, pp. 651–662, July 1976.

[88] C. S. Wu and L. C. Lee, "A theory of the terrestrial kilometric radiation," *apj*, vol. 230, pp. 621–626, June 1979.

[89] R. G. Hewitt, D. B. Melrose, and K. G. Ronnmark, "The loss-cone driven electron-cyclotron maser," *Australian Journal of Physics*, vol. 35, pp. 447–471, 1982.

[90] R. Bingham and R. A. Cairns, "Generation of auroral kilometric radiation by electron horseshoe distributions," *Physics of Plasmas*, vol. 7, no. 7, pp. 3089–3092, 2000.

[91] R. Bingham, B. J. Kellett, R. A. Cairns, J. Tonge, and J. T. Mendona, "Cyclotron maser radiation from astrophysical shocks," *The Astrophysical Journal*, vol. 595, no. 1, p. 279, 2003.

[92] D. Verscharen, K. Klein, B. D. G. Chandran, M. Stevens, C. S. Salem, and S. D. Bale, "ALPS: the arbitrary linear plasma solver," *Journal of Plasma Physics*, vol. 84, 03 2018.

[93] V. L. Ginzburg, "Certain theoretical aspects of radiation due to superluminal motion in a medium," *Soviet Physics Uspekhi*, vol. 2, no. 6, p. 874, 1960.

[94] B. B. Kadomtsev and O. P. Pogutse, "Electric Conductivity of a Plasma in a Strong Magnetic Field," *Soviet Journal of Experimental and Theoretical Physics*, vol. 26, p. 1146, June 1968.

[95] V. D. Shapiro and V. I. Shevchenko, "Quasilinear Theory of Relaxation of an Electron Beam in a Magnetoactive-plasma," *Soviet Journal of Experimental and Theoretical Physics*, vol. 27, p. 635, Oct. 1968.

[96] H. Knoepfel and D. A. Spong, "Runaway electrons in toroidal discharges," *Nuclear Fusion*, vol. 19, pp. 785–829, June 1979.

[97] S. Sajjad, X. Gao, B. Ling, S. H. Bhatti, and T. Ang, "Runaway electron dynamics during impurity gas puffing on HT-7 tokamak," *Physics of Plasmas*, vol. 17, p. 042504, Apr. 2010.

[98] M. V. Nezlin, "Negative-energy waves and the anomalous doppler effect," *Soviet Physics Uspekhi*, vol. 19, no. 11, p. 946, 1976.

[99] K. Molvig, M. S. Tekula, and A. Bers, "Theory of the runaway electron tail," *Physical Review Letters*, vol. 38, pp. 1404–1407, June 1977.

[100] V. V. Parail and O. P. Pogutse, "Instability of the runaway-electron beam in a Tokamak," *Fizika Plazmy*, vol. 2, pp. 228–236, Mar. 1976.

[101] C. S. Liu, V. S. Chan, D. K. Bhadra, and R. W. Harvey, "Theory of Runaway-Current Sustainment by Lower-Hybrid Waves," *Physical Review Letters*, vol. 48, pp. 1479–1482, May 1982.

[102] F. Santini, E. Barbato, F. De Marco, S. Podda, and A. Tuccillo, "Anomalous doppler resonance of relativistic electrons with lower hybrid waves launched in the frascati tokamak," *Phys. Rev. Lett.*, vol. 52, pp. 1300–1303, Apr 1984.

[103] M. J. Mayberry, K.-I. Chen, S. C. Luckhardt, and M. Porkolab, "Particle confinement improvement during 2.45 GHz lower-hybrid current-drive experiments," *Physics of Fluids*, vol. 30, pp. 2288–2291, July 1987.

[104] E. Li, L. Hu, B. Ling, Y. Liu, A. Ti, R. Zhou, H. Lu, and X. Gao, "Identification of anomalous doppler resonance effect during current ramp down in HT-7 tokamak," *Nuclear Instruments and Methods in Physics Research Section A:*

Accelerators, Spectrometers, Detectors and Associated Equipment, vol. 621, no. 1, pp. 566 – 569, 2010.

[105] C. Krafft and A. Volokitin, "Interaction of suprathermal solar wind electron fluxes with sheared whistler waves: fan instability," *Annales Geophysicae*, vol. 21, no. 7, pp. 1393–1403, 2003.

[106] R. Bingham, R. A. Cairs, I. Vorgul, and V. D. Shapiro, "Lower-hybrid waves generated by anomalous doppler resonance in auroral plasmas," *Journal of Plasma Physics*, vol. 76, no. 3-4, p. 539546, 2010.

[107] R. O. Dendy, "On the anomalous doppler/inner lindblad resonance," *Plasma Physics and Controlled Fusion*, vol. 33, no. 9, p. 1069, 1991.

[108] R. O. Dendy and C. N. LashmoreDavies, "Wave-wave resonance instabilities and electron velocity distribution tail structure," *Plasma Physics and Controlled Fusion*, vol. 26, no. 11, p. 1347, 1984.

[109] S. Ichimaru, *Basic principles of plasma physics: a statistical approach.* Reading, Mass: W.A. Benjamin, 1973.

[110] R. Horn, *Matrix analysis.* Cambridge Cambridgeshire New York: Cambridge University Press, 1985.

[111] L. I. Rudakov, "Collective Slowing Down of an Intense Beam of Relativistic Electrons in a Dense Plasma Target," *Soviet Journal of Experimental and Theoretical Physics*, vol. 32, p. 1134, 1971.

[112] R. L. Ferch and R. N. Sudan, "Linear two-stream instability of warm relativistic electron beams," *Plasma Physics*, vol. 17, no. 11, p. 905, 1975.

[113] K. V. Lotov and I. V. Timofeev, "Transition regime of the one-dimensional two-stream instability," *ArXiv e-prints*, Aug. 2014.

[114] R. O. Dendy, C. N. Lashmore-Davies, and A. Montes, "The single-particle and collective descriptions of the anomalous Doppler resonance and the role of ion dynamics," *Physics of Fluids*, vol. 29, pp. 4040–4046, Dec. 1986.

[115] S. Krantz, *Handbook of Complex Variables.* Boston, MA: Birkhauser Boston Imprint Birkhauser, 1999.

[116] Y. A. Omelchenko, V. D. Shapiro, V. I. Shevchenko, M. Ashour-Abdalla, and D. Schriver, "Modified lower hybrid fan instability excited by precipitating

auroral electrons," *Journal of Geophysical Research: Space Physics*, vol. 99, no. A4, pp. 5965–5975, 1994.

[117] G. Zacharegkas, H. Isliker, and L. Vlahos, "Limits of applicability of the quasilinear approximation to the electrostatic wave-plasma interaction," *Physics of Plasmas*, vol. 23, no. 11, p. 112119, 2016.

[118] W. N. Lai, S. C. Chapman, and R. O. Dendy, "Self-consistent nonlinear kinetic simulations of the anomalous doppler instability of suprathermal electrons in plasmas," *Physics of Plasmas*, vol. 20, no. 10, p. 102122, 2013.

[119] W. N. Lai, S. C. Chapman, and R. O. Dendy, "Velocity space evolution of a minority energetic electron population undergoing the anomalous Doppler instability," *Physics of Plasmas*, vol. 22, p. 112119, Nov. 2015.

[120] S. Saito, S. P. Gary, H. Li, and Y. Narita, "Whistler turbulence: Particle-in-cell simulations," *Physics of Plasmas*, vol. 15, no. 10, p. 102305, 2008.

[121] C. F. Kennel and F. Engelmann, "Velocity space diffusion from weak plasma turbulence in a magnetic field," *The Physics of Fluids*, vol. 9, no. 12, pp. 2377–2388, 1966.

[122] R. M. Kulsrud and A. Ferrari, "The relativistic quasilinear theory of particle acceleration by hydromagnetic turbulence," *Astrophysics and Space Science*, vol. 12, pp. 302–318, Aug 1971.

[123] R. O. Dendy, "Classical single-particle dynamics of the anomalous Doppler resonance," *Physics of Fluids*, vol. 30, pp. 2438–2441, Aug. 1987.

[124] K. Papadopoulos, N. Winsor, and B. Hui, "Formation of positive slope on electron runaway distribution in Tokamaks," *Nuclear Fusion*, vol. 17, pp. 1087–1091, Oct. 1977.

[125] G. Kirchhoff, "Ueber das Verhältniss zwischen dem Emissionsvermögen und dem Absorptionsvermögen der Körper für Wärme und Licht," *Annalen der Physik*, vol. 185, pp. 275–301, 1860.

[126] H. Nyquist, "Thermal Agitation of Electric Charge in Conductors," *Physical Review*, vol. 32, pp. 110–113, July 1928.

[127] R. Kubo, "The fluctuation-dissipation theorem," *Reports on Progress in Physics*, vol. 29, no. 1, p. 255, 1966.

[128] A. Sitenko, *Electromagnetic Fluctuations In Plasma.* Burlington: Elsevier Science, 1967.

[129] T. Birmingham, J. Dawson, and C. Oberman, "Radiation processes in plasmas," *The Physics of Fluids*, vol. 8, no. 2, pp. 297–307, 1965.

[130] R. W. Harvey, M. R. OBrien, V. V. Rozhdestvensky, T. C. Luce, M. G. McCoy, and G. D. Kerbel, "Electron cyclotron emission from nonthermal tokamak plasmas," *Physics of Fluids B: Plasma Physics*, vol. 5, no. 2, pp. 446–456, 1993.

[131] R. Gaelzer, P. H. Yoon, S. Kim, and L. F. Ziebell, "On the dimensionally correct kinetic theory of turbulence for parallel propagation," *Physics of Plasmas*, vol. 22, no. 3, p. 032310, 2015.

[132] S. Kim, P. H. Yoon, and G. S. Choe, "Spontaneous emission of electromagnetic and electrostatic fluctuations in magnetized plasmas: Quasi-parallel modes," *Physics of Plasmas*, vol. 23, no. 2, p. 022111, 2016.

[133] P. H. Yoon and R. A. López, "Spontaneous emission of electromagnetic fluctuations in magnetized plasmas," *Physics of Plasmas*, vol. 24, no. 2, p. 022117, 2017.

[134] R. A. López and P. H. Yoon, "Simulation of electromagnetic fluctuations in thermal magnetized plasma," *Plasma Physics and Controlled Fusion*, vol. 59, no. 11, p. 115003, 2017.

[135] A. A. G. R. Z Sagdeev, *Nonlinear plasma theory (Frontiers in physics).* W. A. Benjamin, 1969.

[136] R. A. Cairns, *Plasma physics.* Glasgow Philadelphia: Blackie Distributed in the USA and Canada by Heyden, 1985.

[137] D. J. Kaup, A. Reiman, and A. Bers, "Space-time evolution of nonlinear three-wave interactions. I. Interaction in a homogeneous medium," *Reviews of Modern Physics*, vol. 51, pp. 275–310, Apr. 1979.

[138] Y. C. Kim, J. M. Beall, E. J. Powers, and R. W. Miksad, "Bispectrum and nonlinear wave coupling," *Physics of Fluids*, vol. 23, pp. 258–263, Feb. 1980.

[139] T. Yamada, S.-I. Itoh, S. Inagaki, Y. Nagashima, S. Shinohara, N. Kasuya, K. Terasaka, K. Kamataki, H. Arakawa, M. Yagi, A. Fujisawa, and K. Itoh,

"Two-dimensional bispectral analysis of drift wave turbulence in a cylindrical plasma," vol. 17, pp. 052313–052313, 05 2010.

[140] Y. C. Kim and E. J. Powers, "Digital bispectral analysis of self-excited fluctuation spectra," vol. 21, 08 1978.

[141] T. D. de Wit, *Numerical Schemes for the Analysis of Turbulence — A Tutorial*, pp. 315–342. Berlin, Heidelberg: Springer Berlin Heidelberg, 2003.

[142] S. Itoh, K. Itoh, Y. Nagashima, and Y. Kosuga, "On the application of cross bispectrum and cross bicoherence," *Plasma and Fusion Research*, vol. 12, 1 2017.

[143] B. Chapman, R. Dendy, S. Chapman, K. McClements, G. Yun, S. Thatipamula, and M. Kim, "Nonlinear wave interactions generate high-harmonic cyclotron emission from fusion-born protons during a KSTAR ELM crash," *Nuclear Fusion*, vol. 58, no. 9, p. 096027, 2018.

Appendix A

Relativistic Dispersion Solver

A.1 Quadratic Splines

The grid points z_0, z_1, z_2, z_3, z_4, z_5, z_6, z_7 and z_8 form a 3×3 arrangement and are interpolated with quadratic splines $C(x, y)$ such that:

$$C(x,y) = c_0 + c_1x + c_2x^2 + c_3y + c_4xy + c_5x^2y + c_6y^2 + c_7xy^2 + c_8x^2y^2, \tag{A.1}$$

where,

$$c_0 = z_0 \tag{A.2}$$

$$c_1 = -3z_0 + 4z_1 - z_2 \tag{A.3}$$

$$c_2 = 2(z_0 - 2z_1 + z_2) \tag{A.4}$$

$$c_3 = -3z_0 + 4z_3 - z_6 \tag{A.5}$$

$$c_4 = 9z_0 - 12z_1 + 3z_2 - 12z_3 + 16z_4 - 4z_5 + 3z_6 - 4z_7 + z_8 \tag{A.6}$$

$$c_5 = -2(3z_0 - 6z_1 + 3z_2 - 4z_3 + 8z_4 - 4z_5 + z_6 - 2z_7 + z_8) \tag{A.7}$$

$$c_6 = 2(z_0 - 2z_3 + z_6) \tag{A.8}$$

$$c_7 = -2(3z_0 - 4z_1 + z_2 - 6z_3 + 8z_4 - 2z_5 + 3z_6 - 4z_7 + z_8) \tag{A.9}$$

$$c_8 = 4(z_0 - 2z_1 + z_2 - 2z_3 + 4z_4 - 2z_5 + z_6 - 2z_7 + z_8) \tag{A.10}$$

A.2 Integrating Primatives

The integrals which we must compute are then of the form:

$$p_0 = c_0 \int_0^1 dy \left[\int_0^y dx \frac{1}{1 + b_0 + m_x^1 x + m_y^1 y}\right] + \left[\int_y^1 dx \frac{1}{1 + b_0 + m_x^2 x + m_y^2 y}\right], \tag{A.11}$$

$$p_1 = c_1 \int_0^1 dy \left[\int_0^y dx \frac{x}{1 + b_0 + m_x^1 x + m_y^1 y}\right] + \left[\int_y^1 dx \frac{x}{1 + b_0 + m_x^2 x + m_y^2 y}\right], \tag{A.12}$$

$$p_2 = c_2 \int_0^1 dy \left[\int_0^y dx \frac{x^2}{1 + b_0 + m_x^1 x + m_y^1 y}\right] + \left[\int_y^1 dx \frac{x^2}{1 + b_0 + m_x^2 x + m_y^2 y}\right], \tag{A.13}$$

$$p_3 = c_3 \int_0^1 dy \left[\int_0^y dx \frac{y}{1 + b_0 + m_x^1 x + m_y^1 y}\right] + \left[\int_y^1 dx \frac{y}{1 + b_0 + m_x^2 x + m_y^2 y}\right], \tag{A.14}$$

$$p_4 = c_4 \int_0^1 dy \left[\int_0^y dx \frac{xy}{1 + b_0 + m_x^1 x + m_y^1 y}\right] + \left[\int_y^1 dx \frac{xy}{1 + b_0 + m_x^2 x + m_y^2 y}\right], \tag{A.15}$$

$$p_5 = c_5 \int_0^1 dy \left[\int_0^y dx \frac{x^2 y}{1 + b_0 + m_x^1 x + m_y^1 y}\right] + \left[\int_y^1 dx \frac{x^2 y}{1 + b_0 + m_x^2 x + m_y^2 y}\right], \tag{A.16}$$

$$p_6 = c_6 \int_0^1 dy \left[\int_0^y dx \frac{y^2}{1 + b_0 + m_x^1 x + m_y^1 y} \right] + \left[\int_y^1 dx \frac{y^2}{1 + b_0 + m_x^2 x + m_y^2 y} \right], \tag{A.17}$$

$$p_7 = c_7 \int_0^1 dy \left[\int_0^y dx \frac{xy^2}{1 + b_0 + m_x^1 x + m_y^1 y} \right] + \left[\int_y^1 dx \frac{xy^2}{1 + b_0 + m_x^2 x + m_y^2 y} \right], \tag{A.18}$$

$$p_8 = c_8 \int_0^1 dy \left[\int_0^y dx \frac{x^2 y^2}{1 + b_0 + m_x^1 x + m_y^1 y} \right] + \left[\int_y^1 dx \frac{x^2 y^2}{1 + b_0 + m_x^2 x + m_y^2 y} \right]. \tag{A.19}$$

A.3 Example Jupyter Notebook

We have included here a sample Jupyter notebook which uses the dispersion solver that we outlined in Chapter 3. Further examples are included within the code.

```
"""""In this notebook we use the kinetic dispersion solver to compute
the solution to the two-stream instability for electrons. """
import numpy as np
import matplotlib.pyplot as plt
from multiprocessing import Pool
from KineticDispersion import Solver, Species
import warnings
warnings.filterwarnings('ignore')
%matplotlib inline
#%matplotlib notebook
```

```
"""""Define physical constants"""
e0 = 8.85E-12
mu0 = 1.26E-6
e = 1.6E-19
kb = 1.38E-23
me = 9.11E-31
ev = 11500
cl = 3E8
```

```
""labelsize=9
fontsize=12

def miniFigure():
    """Sets up a small single figure. """
    fig, ax = plt.subplots(1, 1, figsize=(2.86, 2.42))
    plt.subplots_adjust(left=0.17, right=0.83, top=0.97, bottom=0.19)
    ax.tick_params('x', labelsize=labelsize)
    ax.tick_params('y', labelsize=labelsize)
    lbaxes = fig.add_axes([0.17, 0.19, 0.66, 0.78], frameon=False)
    lbaxes.set_xticks([])
    lbaxes.set_yticks([])
    lbaxes.yaxis.tick_right()
    lbaxes.tick_params('y', labelsize=labelsize)
    lbaxes.yaxis.set_label_position("left")
    return fig, ax, lbaxes
```

```
"""""Define constants for the two-stream instability"""
Te = ev*1 #Electron temperature of 1ev.
B = 0.0000001 #Must define a negilible background magnetic field.
density = 2.5E19 #Number density per metre cubed.
v0 = cl/1000.0 #Drift velocity
vth = cl/1000000.0 #Thermal velocity
wpe = (density*e**2/(e0*me))**0.5 #Plasma frequency
wce = e*B/me #Electron cyclotron frequency
```

```
"""""Set constants for plotting"""
wunit = wpe #The unit which we normalize frequency to.
kunit = wunit/v0 #The unit we normalize wavenumber to.
viewbounds = (0.0001, 2, -0.025, 2.0) #The range of values we plot.
```

```
"""""Two drifting maxwellians. Distributions are truncated at 5vth"""
vpara1min = -5*vth - v0
vpara1max = 5*vth - v0
vpara2min = -5*vth + v0
vpara2max = 5*vth + v0
vperpmin = 0.0 #vperp starts at 0
vperpmax = 5*vth
nperp = 1000
npara = 1000
vpara1 = np.linspace(vpara1min, vpara1max, npara, dtype='float64')
vpara2 = np.linspace(vpara2min, vpara2max, npara, dtype='float64')
vperp = np.linspace(vperpmin, vperpmax, nperp, dtype='float64')
Fvpara1 = np.exp((-0.5*(vpara1 + v0)**2/(vth**2)))
Fvpara2 = np.exp((-0.5*(vpara2 - v0)**2/(vth**2)))
Fvperp = np.exp((-0.5*vperp**2/(vth**2)))
Fv1 = np.outer(Fvpara1, Fvperp)
Fv2 = np.outer(Fvpara2, Fvperp)
```

```
"""""Create a species object for each beam. """
s1 = Species(-1*e, me, 0.5*density, vpara1, vperp, Fv1,
                np.arange(0, 1))
s2 = Species(-1*e, me, 0.5*density, vpara2, vperp, Fv2,
                np.arange(0, 1))

"""Create a dispersion solver using a list of species. """
solver = Solver(B, [s1, s2])
```

```
"""""Angle should not be exactly zero. """
theta = 0.000001*np.pi/180
"""ww defines the frequencies which we plot in the background"""
ww = np.linspace(viewbounds[2], viewbounds[3], 100)*wpe + 0.0001j*wpe
kk = np.linspace(viewbounds[0], viewbounds[1], 40)*kunit
"""We use a 2D array of guesses, defined by a real and imaginary
components wwr, wwi. """
wwr = np.linspace(-0.2, 2.0, 100)*wpe
wwi = np.linspace(0.000001j, 1.8j, 20)*wpe
ww2 = np.outer(wwr, np.ones(len(wwi))) \
+ np.outer(np.ones(len(wwr)), wwi)
"""k has a parallel and perpendicular component. """
kkpara = kk*np.cos(theta)
kkperp = kk*np.sin(theta)
"""Set up the values of k we will solve for as a list. """
klist = np.array((kkpara, kkperp)).T
```

```python
"""""The problem is embarassingly parallel so we construct a process
pool. Here we have used a desktop supporting 8 processes. """

def func(k):
    """Evaluate the insolution at k using ww. """
    marginalized = solver.marginalize(ww, k)
    return marginalized

def func2(k):
    """Find roots using the 2D initial guess array ww2. """
    roots = solver.roots(ww2, k)
    return roots

pool = Pool(8)

try:
    """We construct an array of insolution to plot. """
    insolution = np.array(pool.map_async(func, klist).get(99999))
    roots = pool.map_async(func2, klist).get(99999)
    pool.close()
except:
    pool.terminate() #Terminate cleanly.
    print ’Pool exception’
finally:
    pool.join()
```

```python
"""""Post process the output into plotable format. """
root_w = []
root_k = []
for rootset, k in zip(roots, klist):
    for root in rootset:
        root_w.append(root[0])
        root_k.append((k[0]**2 + k[1]**2)**0.5*np.sign(k[0]))

root_w = np.array(root_w)
root_k = np.array(root_k)

"""We differentiate between small and large growth rates. """
growthmask = np.where(root_w.imag/wunit>1E-3)
stationarymask = np.where(root_w.imag/wunit<=1E-3)
```

```
"""""Finally we generate the figure. """
fig, ax, lbaxes = miniFigure()
lbaxes.yaxis.set_label_position("right")

im = ax.imshow((np.sign(insolution.real)/np.abs(insolution)**0.5).T,
                aspect='auto', interpolation='nearest', extent=viewbounds,
                vmin=-2.5E1, vmax=2.5E1, origin='lower', cmap='bwr')
ax.plot(root_k[stationarymask]/kunit, root_w[stationarymask].real/wunit,
        ls='None', marker='.', color='black', markersize=4)
ax.plot(root_k[growthmask]/kunit, root_w[growthmask].real/wunit,
        ls='None', marker='.', color='#FFC700', markersize=4)
ax.plot(root_k[growthmask]/kunit, root_w[growthmask].imag*1E0/wunit,
        color='red', ls='None', marker='.', markersize=4)
ax.set_ylim(viewbounds[2], viewbounds[3])
ax.set_xlim(0, 2)

ax.set_xlabel('$kv_{0}/\omega_{pe}$', fontsize=fontsize)
ax.set_ylabel('$\omega[\omega_{pe}]$', fontsize=fontsize)
lbaxes.set_ylabel('$\gamma[\omega_{pe}]$', fontsize=fontsize)
ax.tick_params('x', labelsize=labelsize)
ax.tick_params('y', labelsize=labelsize)
```